Final Report

The Charles Pankow Foundation
Research Grant Agreement #05-19
Steel Coupling Beams in Low-Seismic and Wind Applications

University of Cincinnati, Cincinnati, OH
Sushil Kunwar
Bahram M. Shahrooz, PE, FACI, FASCE, FSEI

CHARLES PANKOW FOUNDATION
Building Innovation through Research

MAGNUSSON KLEMENCIC ASSOCIATES
Structural + Civil Engineers

This page left blank intentionally.

Table of Contents

List of Tables

List of Figures

This page left blank intentionally.

Executive Summary

Research Overview

Coupled structural (shear) walls (CSW) are a common structural system. This system is comprised of two or more structural walls that are linked, typically, at each floor by coupling beams. Based on the expected level of inelastic deformations, composite structural (shear) walls can be classified as Composite Ordinary Shear Wall (COSW) or Composite Special Shear Wall (CSSW). One common composite system involves linking reinforced concrete wall piers by steel (or steel-concrete composite) coupling beams that are embedded in the wall piers. Design and detailing of steel coupling beam-wall connection in COSW was the focus of the research reported herein.

In the 2010 and earlier versions of AISC 341 *Seismic Provisions*, the coupling beam-wall connection was designed to develop the coupling beam's expected capacity. This provision in the 2016 version was replaced by the requirement that the connection in COSW be designed only to develop the demand from the coupling beam as calculated by linear-elastic analysis with no ductile detailing requirements. As a result, the design and detailing of the embedment region has been relaxed. This change leads to shorter embedment lengths and smaller reinforcement in the embedment region.

Analytical studies conducted at the University of Cincinnati indicated the shorter embedment length could accelerate the loss of coupling beam-wall connection integrity, leading to a reduction in the level of coupling action between the wall piers. The loss of coupling action will affect the demands in the wall piers, and their capacities could be exceeded. Moreover, inter-story and overall drifts could surpass acceptable limits. Primarily to remedy these observations, AISC 341 *Seismic Provisions* was modified in 2022 by specifying a minimum

embedment length of not being less than the coupling beam's depth and requiring additional longitudinal reinforcement along the embedded region.

A coordinated experimental (consisting of two half-scale and four three-quarter beam-wall subassemblies) and analytical study was conducted to examine the current design provisions for steel coupling beams in COSW outlined in AISC 341-2022. It is important to note that the current (and previous) AISC *Seismic Provisions* for coupling beams in COSW and CSSW are solely based on experimental research focused on coupling beam-wall connection details intended to resist high seismic loads. To the best of the authors' knowledge, no experimental research had been conducted to understand the performance of COSW prior to the study presented in this report. The research data were used to evaluate the current AISC 341 *Seismic Provisions* and to develop new design and detailing provisions for COSW.

Summary and Observations

The following conclusions and observations are made:

1. The additional longitudinal reinforcement required by AISC 341-22 did not appreciably impact the connection performance in terms of the initial stiffness, stiffness degradation, dissipated energy, maximum load that could be resisted, and mode of failure.
2. Except for the specimens with embedment length/coupling beam depth ≤ 1 and the specimen with auxiliary transfer bars attached to the flanges, the other specimens did not fully develop their target nominal shear strength (V_n).
3. For the specimens without face bearing plates, which act as a bearing stiffener, the coupling beam's flange and web experienced local bending and buckling. In one specimen with face bearing plates, which failed prematurely due to excessive damage in the connection region, the flange experienced a small amount of bending within the

connection region – the bending occurred at a location that was away from the face bearing plates.

4. The applicability of current AISC Eq H4-1 for determining the required embedment length is questionable for cases with embedment length/coupling beam depth ≤ 1 because strain distribution is not linear for such cases. One of the implicit assumptions in AISC Eq H4-1 is that strain varies linearly along the embedment length. Although Eq. H4-1 underestimates the connection capacity and is conservative for cases with embedment length/coupling beam depth ≤ 1, the use of strut-and-tie models is more appropriate.

$$V_n = 1.54\sqrt{f_c'}\left(\frac{b_w}{b_f}\right)^{0.66}\beta_1 b_f L_e\left[\frac{0.58-0.22\beta_1}{0.88+\frac{g}{2L_e}}\right] \qquad \text{AISC Eq H4-1}$$

5. The auxiliary transfer bars provide a direct load path for transferring the forces in the coupling beam to the surrounding concrete. This direct load path is not offered by longitudinal reinforcement along the embedment length. The lack of a direct load path is deemed to be the main reason for the similarities of the performance of the specimens with or without the higher longitudinal reinforcement required by AISC 341-22.

6. Based on analysis of the test results, the following equation was developed for calculating the required embedment length:

$$V_n = \frac{0.19 f_c' b_f L_e}{0.56+\frac{g}{2L_e}}$$

7. The measured capacities were found to be on average within 3% of the capacities calculated by the new equation. Additional analytical studies of archetypes from several previous research indicate an excellent correlation between the capacities determined by using a detailed, mechanistic procedure and those from the new equation. Not only does the new equation closely capture the connection capacity but it is also simpler than the current equation (AISC Eq. H4-1).
8. The use of the new equation results in longer embedment lengths than the values computed from the current AISC Eq. H4-1. However, the embedment lengths are much shorter than those needed to develop the member capacity, which was required in the 2010 or earlier versions of AISC 341 *Seismic Provisions*.
9. With 95% confidence, the average value of the experimental stiffness is between 0.678 and 0.692 times the value obtained by using the effective moment of inertia calculated from AISC Eq. C-H4-1. Therefore, the coefficient of 0.6 in this equation needs to be changed to 0.4.

$$I_{eff} = 0.60I\left(1 + \frac{12\lambda EI}{g^2 G A_w}\right)^{-1} \qquad \text{Eq C-H4-1}$$

10. The archetype, which was used to select and detail the test specimens, had been designed by using the current AISC Eq. C-H4-1. By using the modified version of this equation (i.e., using 0.4 instead of 0.6), the first-floor wall piers of the archetype were found to be slightly inadequate (demand/capacity became 1.03 instead of 0.97 in the original design). Furthermore, the wind load inter-story drifts for several stories exceeded the limit of $h/450$, where h is the story height, but all the inter-story drifts remained below $h/400$.

Recommendations

In view of the results presented in this report, the following revisions to AISC 341 seismic provisions are recommended.

1. Replace the current AISC Eq. H4-1 by

$$V_n = \frac{0.19 f_c' b_f L_e}{0.56 + \frac{g}{2L_e}}$$

2. Replace the current AISC Eq. C-H4-1 by

$$I_{eff} = 0.40I\left(1 + \frac{12\lambda EI}{g^2 G A_w}\right)^{-1}$$

3. Require a bearing stiffener ("face bearing plates") at the interface between steel coupling beams and reinforced concrete walls. This requirement may be waived if the adequacy of flanges and web against bending and buckling is ensured. Note that face bearing plates could simplify the formwork around the flanges and web.

Acknowledgements

The research presented in this report was funded by the Charles Pankow Foundation and co-funded by the American Institute of Steel Construction and the Magnusson Klemencic Associates (MKA) Foundation. These foundations are gratefully thanked for their financial support. The authors express their gratitude to Ms. Anne Ellis, former Executive Director of the Charles Pankow Foundation, who continued to support the project as the research team overcame several delays because of lab closure during the Covid pandemic and equipment problems. Mr. Ron Klemencic and Mr. Kevin Aswegan at Magnusson Klemencic Associates are acknowledged for their technical advice and informative discussions throughout the project. Dr. Devin Huber at the American Institute of Steel Construction is thanked for facilitating the fabrication of several test fixtures and taking care of their associated costs. Dr. Christopher Motter at Washington State University is thanked for discussions throughout the project. The members of AISC Task Committee 5 (Composite Design) are acknowledged for their feedbacks during various phases of the project.

Material donations and support from the following companies are gratefully acknowledged: reinforcing bars by Contractors Materials Co. (CMC) in Cincinnati, Ohio; auxiliary transfer bars and their associated hardware by LENTON in Solon, Ohio; Baker Concrete in Monroe, Ohio provided the forms for the phase one test specimens; Terracon in Cincinnati, Ohio performed many of the concrete cylinder tests. Mr. Floyd Tharpe, Mr. Garrett Tharpe, and Mr. Terry Tincher at Family Tradition in Spring Valley, Ohio helped with the fabrication of phase two test specimens; their assistance is gratefully acknowledged. Mr. Terry Tincher's endless support throughout the experimental phase is acknowledged and gratefully

appreciated. Ms. Sarah Jobe of K&M industry in Spring Valley, Ohio is sincerely thanked for her help with the logistics of fabrication and delivery of the second phase test specimens.

The authors express their gratitude to Mr. TJ Brown at the University of Cincinnati Large Scale Test Facility and Mr. Curtis Fox from the Department of Aerospace Engineering at the University of Cincinnati for their technical support. The following former and current students at the University are thanked for their help with various aspects of the experimental phase of the reported research: Mr. Samuel Blesi, Dr. Sandip Chhetri, Dr. Abdullah Haroon, and Ms. Margaret Sullivan-Miller.

The authors dedicate this report to our friend and colleague Dr. Partick J. Fortney at the University of Cincinnati who unexpectedly passed away in 2019. His deep desire to understand behavior and performance of ordinary composite coupled walls was the genesis of the reported research. The proposed changes to AISC *Seismic Provisions* would not have been possible without Pat's passion to teaching, research, and practice of structural engineering.

This page left blank intentionally.

Chapter 1 Introduction and Background

1.1 Introduction

Coupled structural (shear) walls (CSW) are a common structural system. This system has become more widespread after the 9/11 attack because of its inherent redundancy and minimal impact on architectural versatility. The system consists of two or more wall piers connected by coupling (link) beams. The coupling beams allow the transfer of vertical forces between the adjacent wall piers, thus, creating a frame-like action. This action induces an axial force couple which opposes the global overturning moment from lateral forces. The coupling action provides three significant benefits. First, it decreases the moments that the individual wall piers must resist. Second, the coupling beams dissipate energy by undergoing inelastic deformations. Third, the coupled system has significantly larger stiffness than that from the individual wall piers, thereby, reducing the roof deflection and inter-story drifts.

For reinforced concrete (RC) coupling beams, special diagonal reinforcement (Figure 1.1) is necessary to prevent or reduce the likelihood of sliding failure at the beam-wall interface. The use of special diagonal reinforcement complicates the construction process and may increase the project's time and cost. The designer may also need to provide impractically deep beams because of the limited shear capacity of RC coupling beams (Harries et al., 2005). The impacts of these issues can be eliminated or reduced by replacing RC coupling beams with steel coupling beams. The resulting structural system, which uses steel beams for coupling action, is known as a Hybrid/Composite Coupled Wall System.

Based on the expected level of inelastic deformations, composite structural (shear) walls can be classified as Composite Ordinary Shear Wall (COSW) or Composite Special Shear Wall (CSSW). The design and detailing of COSW and CSSW are presented in Sections H4 and H5 of

AISC Seismic Provision 341-16 (AISC 341-16, 2016), respectively. COSW systems are used in regions with low-to-moderate seismic demands and are expected to undergo limited inelastic deformations. On the other hand, CSSW systems are used in regions with high seismic demands and are expected to undergo significant inelastic deformations. The design and detailing of the coupling beam-wall connection in COSW is the focus of this research.

In the 2010 and earlier versions of AISC 341 seismic provisions (AISC 341-10, 2010), the coupling beam-wall connection was designed to develop the coupling beam's expected capacity. This provision in the 2016 version (AISC 341-16, 2016) was removed and replaced by the requirement that the beam-wall connection in COSW be designed only to develop the demand from the coupling beam as calculated by linear-elastic analysis with no ductile detailing requirements. It is important to note that the current provisions for coupling beams in COSW and CSSW are solely based on experimental research focused on coupling beam-wall connection details intended to resist high seismic loads. There is little experimental research to support the revised provisions for COSW.

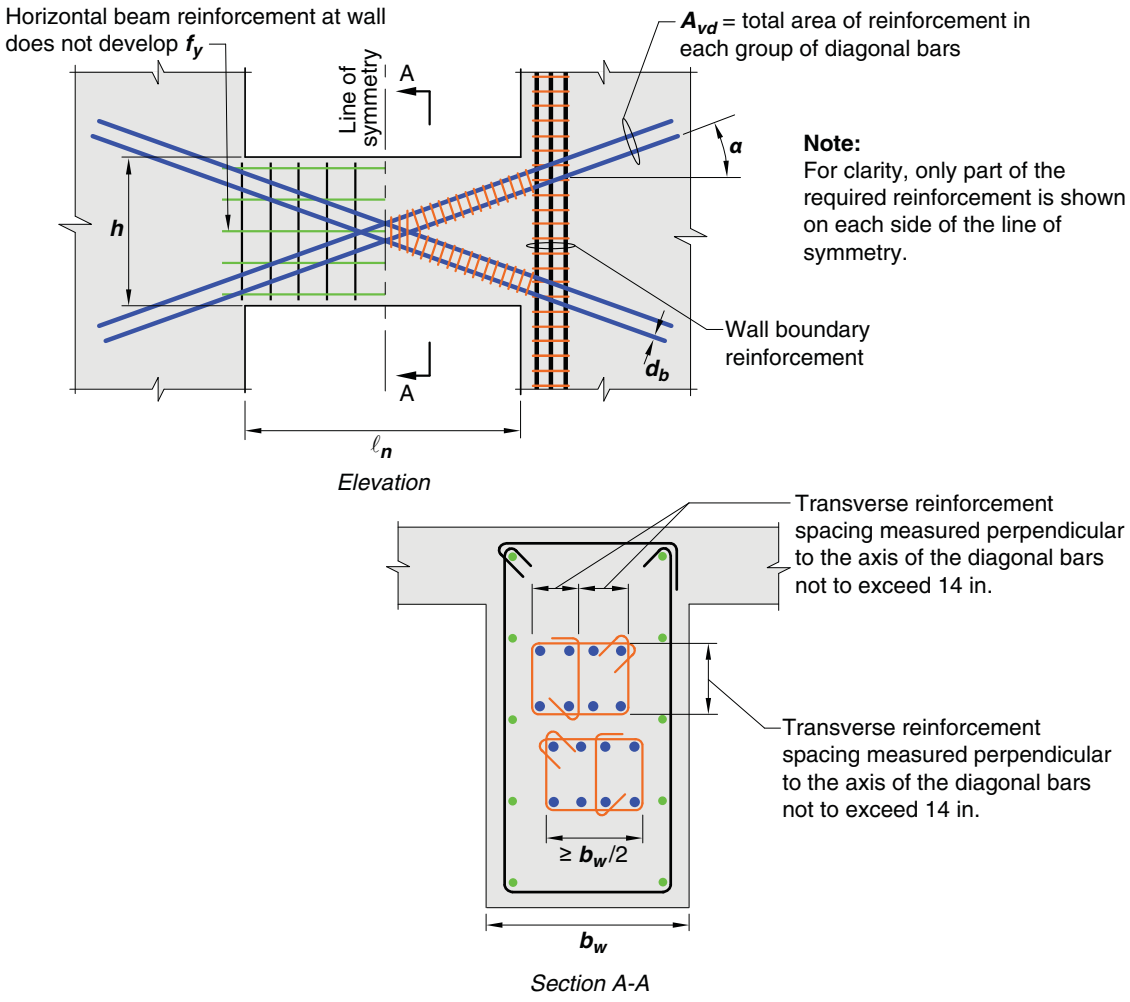

Figure 1.1 Diagonal reinforcement of reinforced concrete coupling beams (source: ACI 318-19).

1.2 Review of Past Research and Design Provisions

1.2.1 Background of coupling beam-wall connection design

The coupling beam's embedment length is calculated using an equation developed by Mattock and Gaafar (1982), which was originally formulated to find the strength of embedded steel brackets/corbels cast in precast concrete columns. The equation is based on satisfying force and moment equilibrium in the embedment region and is shown in Eq 1.1.

$$V_n = 1.54\sqrt{f_c'}\left(\frac{b_w}{b_f}\right)^{0.66}\beta_1 b_f L_e\left[\frac{0.58-0.22\beta_1}{0.88+\frac{g}{2L_e}}\right] \qquad \textbf{Eq 1.1}$$

b_f = coupling beam flange width, in.

b_w = thickness of wall pier, in.

f_c' = specified concrete compressive strength, ksi

g = coupling beam clear span, in.

L_e = embedment length, in.

$$\beta_1 = \begin{cases} 0.85 \text{ if } f_c' \leq 4 \text{ ksi} \\ 0.65 - 0.2\left(\dfrac{f_c' - 8}{4}\right) \text{ for } 4 \leq f_c' < 8 \text{ ksi} \\ 0.65 \text{ if } f_c' \geq 8 \text{ ksi} \end{cases}$$

1.2.2 AISC 341-10 vs. AISC 341-16

The provisions for coupling beams in COSW were significantly changed in 2016. These changes are discussed in this section and contrasted against those in the 2010 version of AISC 341. The impacts of these changes are illustrated through simulation studies of a 25-story prototype structure. The differences between these two provisions are discussed for (a) calculation of design force and (b) detailing of embedment region.

1.2.2.1 Design force

According to AISC 341-10, the coupling beam-wall connections are designed such that the strength is at least equal to the expected strength of the coupling beam as shown in Eq 1.2

$$V_{connection} = V_n = \frac{2R_y M_p}{g} \leq R_y V_p \qquad \textbf{Eq 1.2}$$

M_p = coupling beam plastic moment capacity

R_y = ratio of expected yield strength to specified minimum yield strength

V_p = coupling beam plastic shear capacity

In the 16th edition of AISC 341, the requirement that the connection be designed to develop the coupling beam's expected strength was changed to designing the connection for the demands from linear elastic analysis which is shown in Eq 1.3.

$$\phi V_{connection} \geq V_{elastic} \quad \textbf{Eq 1.3}$$

$\phi = 0.9$

Concrete spalling may occur at the beam-wall connection during cyclic wind or low seismic loading. The loss of concrete cover will reduce the embedment length available for transferring forces. AISC 341-10 took this effect into account, in part, by assuming the embedment length to begin inside the wall from the first wall longitudinal bar in the boundary element. In contrast, AISC 341-16 does not consider the wall spalling and assumes that the calculated embedment length begins from the face of the wall.

1.2.2.2 Embedment region detailing

Past research (Harries et al.,1997) demonstrated the need for longitudinal reinforcement in embedded regions to control gap opening at coupling beam flange-wall boundary interface under cyclic loading, which is shown schematically in Figure 1.2. AISC 341-10 specified vertical wall reinforcement over the embedment length with a nominal axial strength of at least equal to the coupling beam's expected shear strength. On the other hand, AISC 341-16 requires vertical wall reinforcement to resist the coupling beam's linear elastic shear demand. The required reinforcement (A_{st}) is computed from Eq 1.4, in which V_n is the coupling beam's expected strength based on ASIC 341-10 and is linear elastic shear demand of coupling beam according to AISC 341-16 and f_y is reinforcement yield strength.

$$f_y A_{st} \geq V_n \quad \textbf{Eq 1.4}$$

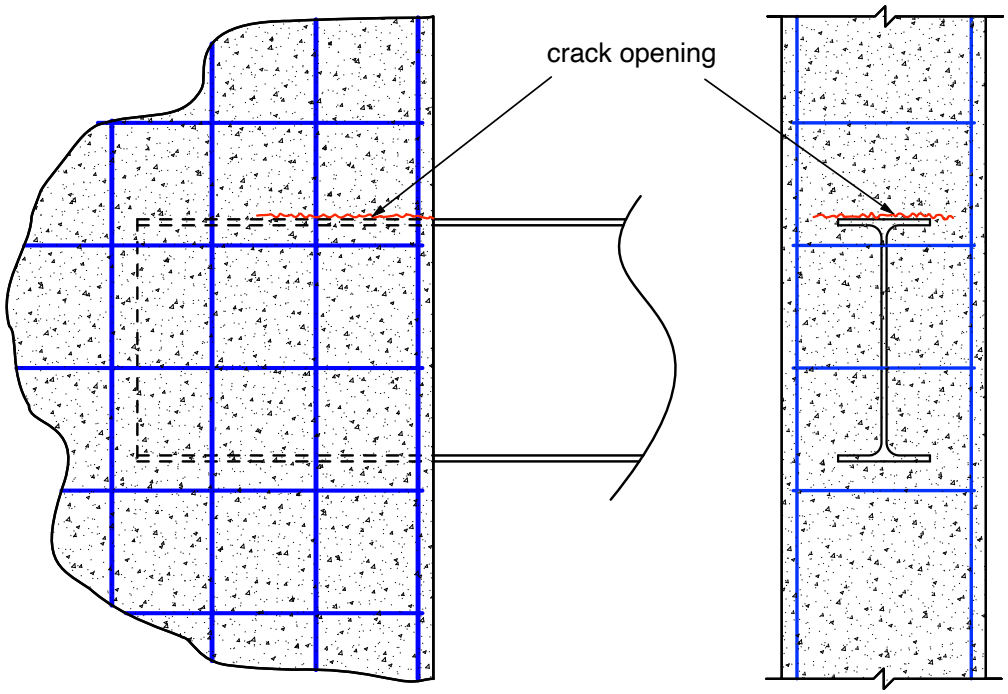

Figure 1.2 Gap opening at coupling beam-wall interface.

Both versions require distributing the longitudinal reinforcement such that two-thirds of the calculated reinforcement is within the first half of the embedment length. The reinforcement must extend at least one tension development length above and below the flanges.

1.2.2.3 Summary

The above discussions indicate that the embedment region design and detailing have been relaxed in the 2016 version of AISC 341. This change will lead to a smaller embedment length and smaller reinforcement in the embedment region. The implications of these relaxations have yet to be determined.

1.2.3 Expected impacts of changes made in AISC 341-16

In an attempt to examine the potential impacts of AISC 341-16 provisions, an analytical study of COSW was conducted by Mirza (2018). A 25-story office building located in Cincinnati (a low seismic region) was selected and designed. Due to the absence of a boundary element in the wall for an ordinary system, the embedment region can be vulnerable if the

calculated embedment length is short, and connection degradation is expected to occur. Gradual degradation of connection was simulated in the ETABS (2016). For this purpose, the embedment length was progressively reduced by 1 in., 2 in., or 4 in. to model cracking at the coupling beam-wall interface. For each value, rotational springs (Figure 1.3) were calibrated such that the calculated demands match the available capacities after inducing damage. The shear and moment capacities before damage (V and M) and their counterparts after damage (V' and M') are shown in Eq 1.5.

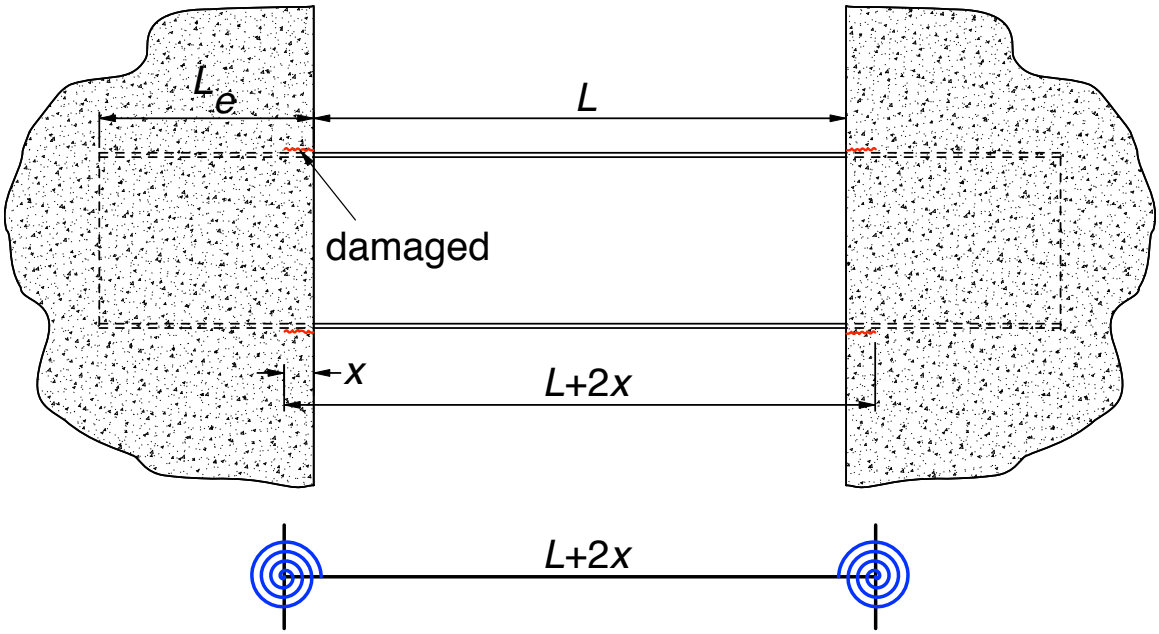

Figure 1.3 Simulation of stiffness by rotational springs.

$$V = \phi 1.54\sqrt{f_c'}\left(\frac{b_w}{b_f}\right)^{0.66}\beta_1 b_f L_e\left[\frac{0.58-0.22\beta_1}{0.88+\frac{L}{2L_e}}\right]$$

$$V' = \phi 1.54\sqrt{f_c'}\left(\frac{b_w}{b_f}\right)^{0.66}\beta_1 b_f (L_e-x)\left[\frac{0.58-0.22\beta_1}{0.88+\frac{L+2x}{2(L_e-x)}}\right] \quad \textbf{Eq 1.5}$$

$$\frac{M'}{M} = \frac{V'}{V}\left(\frac{L+2x}{L}\right)$$

As the level of damage was progressively increased the overall stiffness dropped, leading to larger inter-story drifts. As shown in Figure 1.4, the inter-story drifts in floors above the 8th floor exceeded $h/450$ ($h =$ inter-story height) and floors above the 11th floor exceeded $h/400$ with the introduction of 2 in. of connection degradation. For 4-in. degradation, the inter-story drifts above the 3rd floor exceeded both limits. A similar trend was observed when considering lateral drifts, see Figure 1.5.

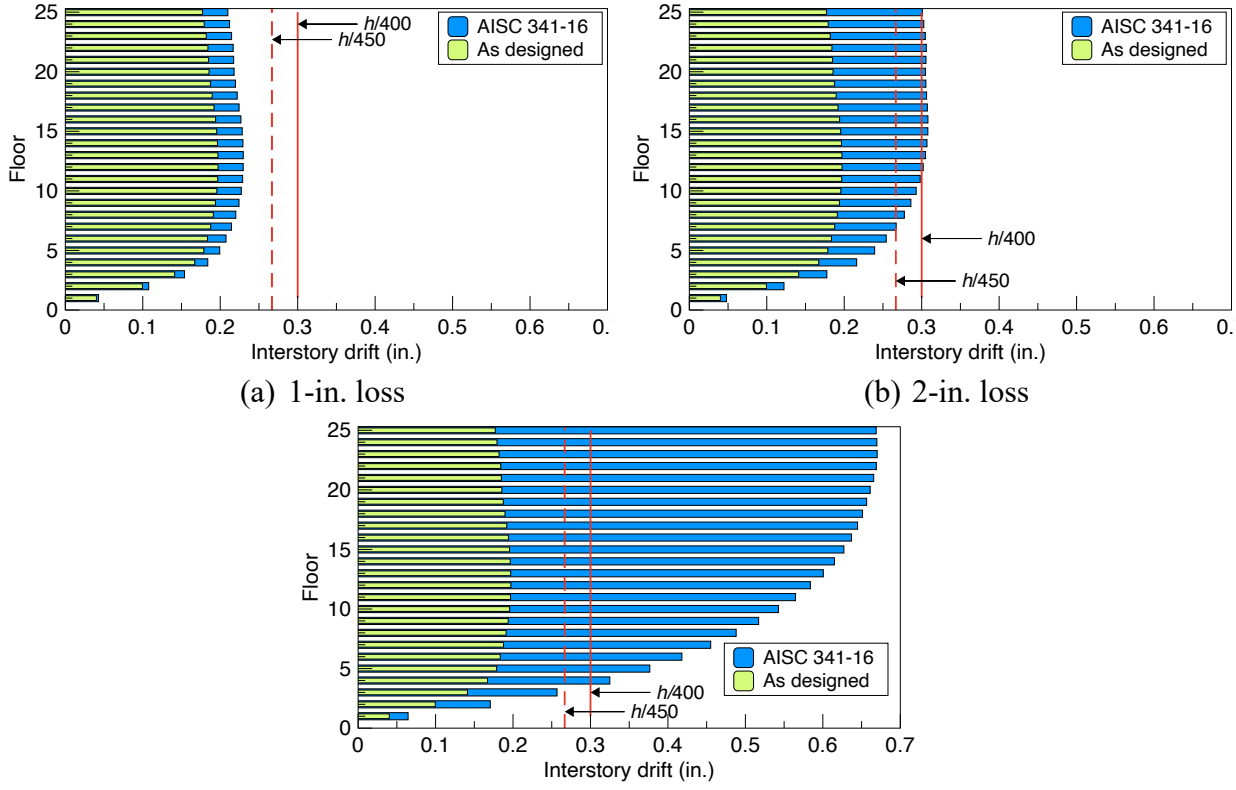

Figure 1.4 Changes in inter-story drifts for different losses of embedment length.

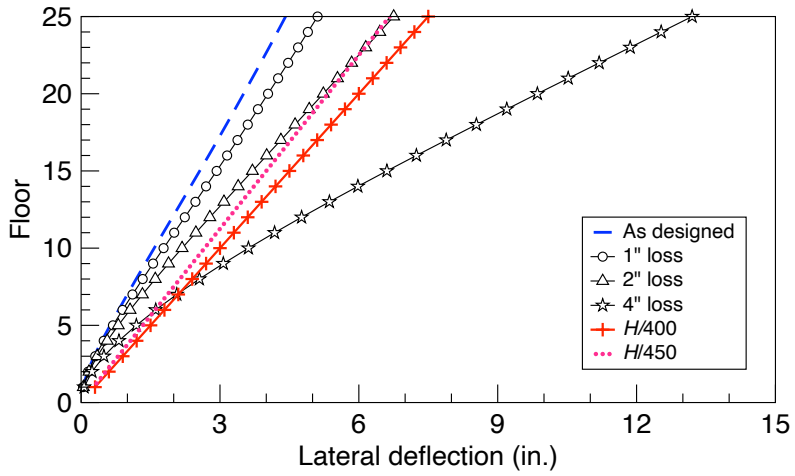

Figure 1.5 Impact of connection degradation on lateral drift.

With the loss of coupling beam-wall connection integrity, the level of coupling action was reduced. As a result, the demands in the wall piers were impacted. In general, the wall pier capacities were exceeded as the level of damage (simulated by reducing the "effective" embedment length) became larger, i.e., wall demand to capacity exceeded 1 as shown in Figure 1.6. For several locations, e.g., at floor 5, the introduction of damage lowered the wall demand to capacity ratio. This trend can be explained with reference to Figure 1.7. After accounting for loss of embedment length, the coupling action was reduced and moment in the coupled direction increased from -1394 k-ft to -5698 k-ft. At the same time, the axial tension induced by coupling action was decreased, increasing the axial load from 1460 kips to 2028 kips. As a result of these shifts, the moment demand was moved farther away from the moment contour, which reduced the demand-to-capacity ratio.

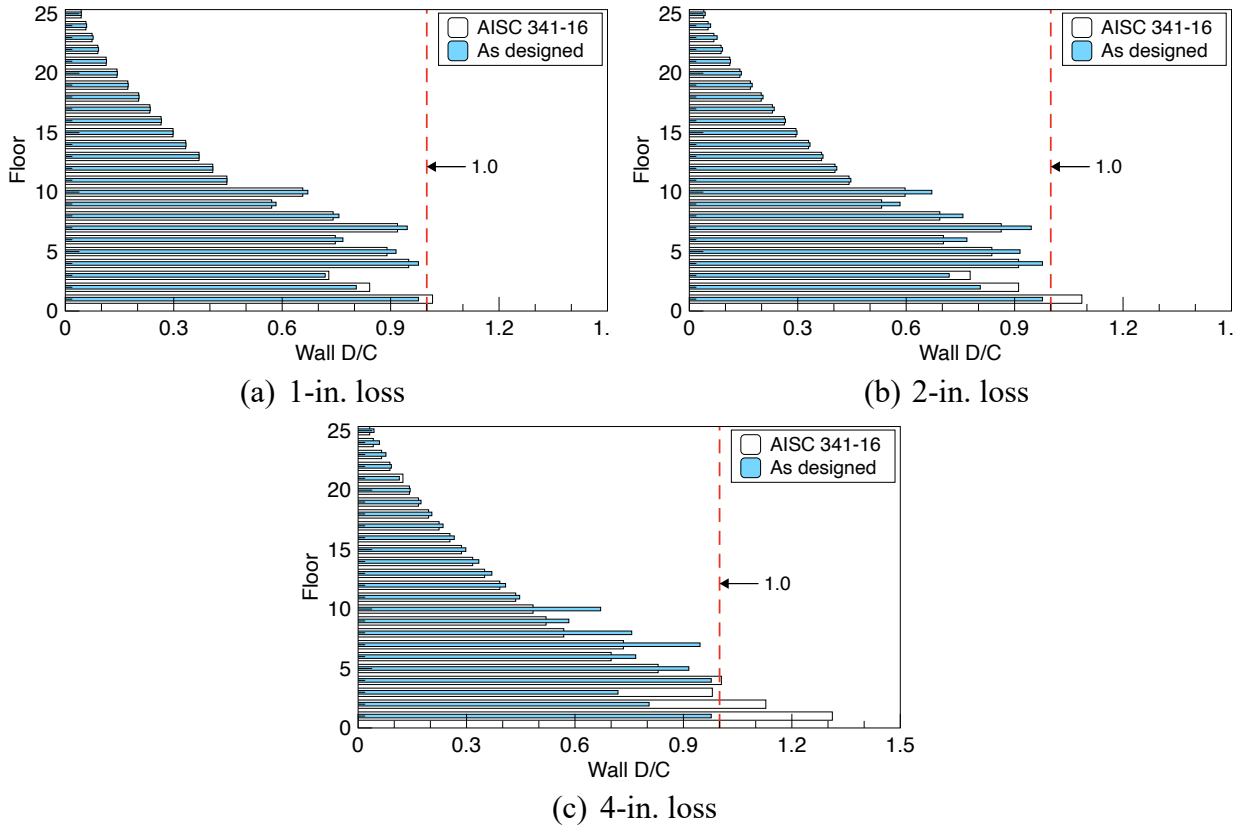

Figure 1.6 Impact of connection degradation on capacity of wall piers.

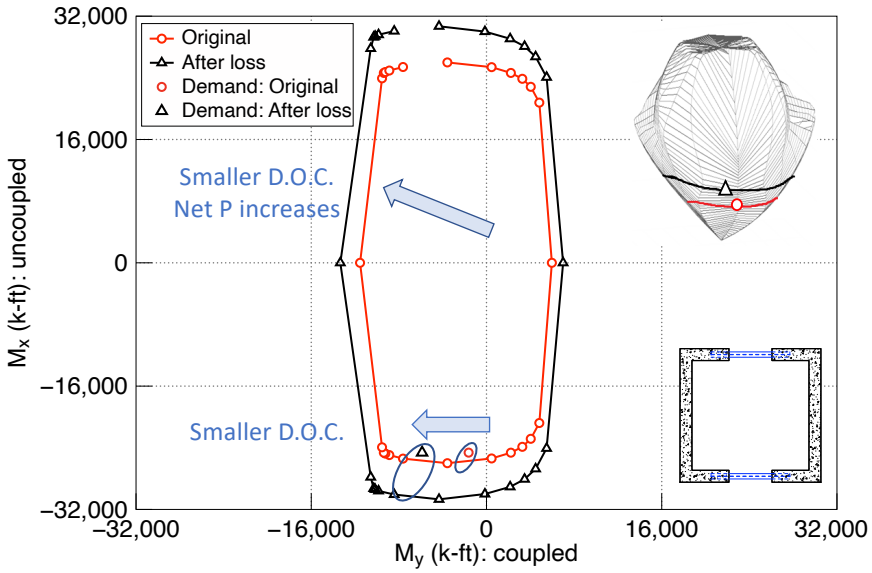

Figure 1.7 Comparison of wall pier axial load and bending moment with and without damage.

1.2.4 AISC 341-22

The elastic demands at the top and bottom stories are typically small. If connections are required to develop such low values of elastic demands (as recommended by AISC 341-16), the calculated embedment length could be unrealistically small. Driven primarily based on the results of the analyses performed by Mirza (2018), which was discussed in Section1.2.3, several changes have been proposed to remedy the potential issues observed in the simulations. The key changes are as follows:

(a) Specify a minimum embedment length equal to coupling beam depth.

(b) Revise the reinforcement needed to control gap opening, as discussed in Section 1.2.2.2. Eq 1.4 is replaced by Eq 1.6.

$$f_y A_{st} \geq C_b$$

where

A_{st} = area of reinforcement

Eq 1.6

$$C_b = \text{greater of} \left(\frac{\frac{g}{2L_e} + 0.33\beta_1}{0.88 - 0.33\beta_1} \right) V_n \text{ and } V_n$$

f_y = reinforcement yield strength

V_n = coupling beam elastic shear demand

1.3 Project overview and objectives

A coordinated experimental and analytical study was conducted to examine design provisions for steel coupling beams in COSW. Large-scale test specimens were selected based on a 25-story prototype structure located in Cincinnati. The test specimens consisted of two half-scale beam-wall subassemblies and four three-quarter scale beam-wall components. The

experimental test data were utilized to scrutinize AISC 341-16 and AISC 341-22 design and detailing provisions for COSW with the ultimate objective of proposing revisions.

Chapter 2 Experimental Program

2.1 Introduction

As discussed in Chapter 1, the test specimens were selected based on a 25-story archetype. An overview of the design of the archetype is provided in this chapter. Additionally, the test specimen details, measured material properties, key features of the testing apparatus, and instrumentations are presented.

2.2 Selection and design of archetype

A twenty-five-story office building was selected and designed. The plan view of the archetype is shown in Figure 2.1. Cincinnati, Ohio, which is in a low seismic region, was selected as the location of the building. Two C-shaped composite ordinary shear walls (COSW) linked by steel coupling beams (two per floor) form the lateral force-resisting system. The gravity load resisting system consists of columns, spandrel beams, and post-tensioned floor slabs. Design of the archetype is discussed in Kunwar (2020).

As seen from Table 2.1, minimum reinforcement (0.25%) controlled the transverse reinforcement for all the floors except for the first three stories. Minimum reinforcement also controlled the longitudinal reinforcement for the walls above story 8. Four groups of coupling beams were selected (see Table 2.2). The maximum coupling beam shear demand (185 kips) was in story 9. Three rolled wide flange shapes were selected based on the maximum calculated shear demand in each group.

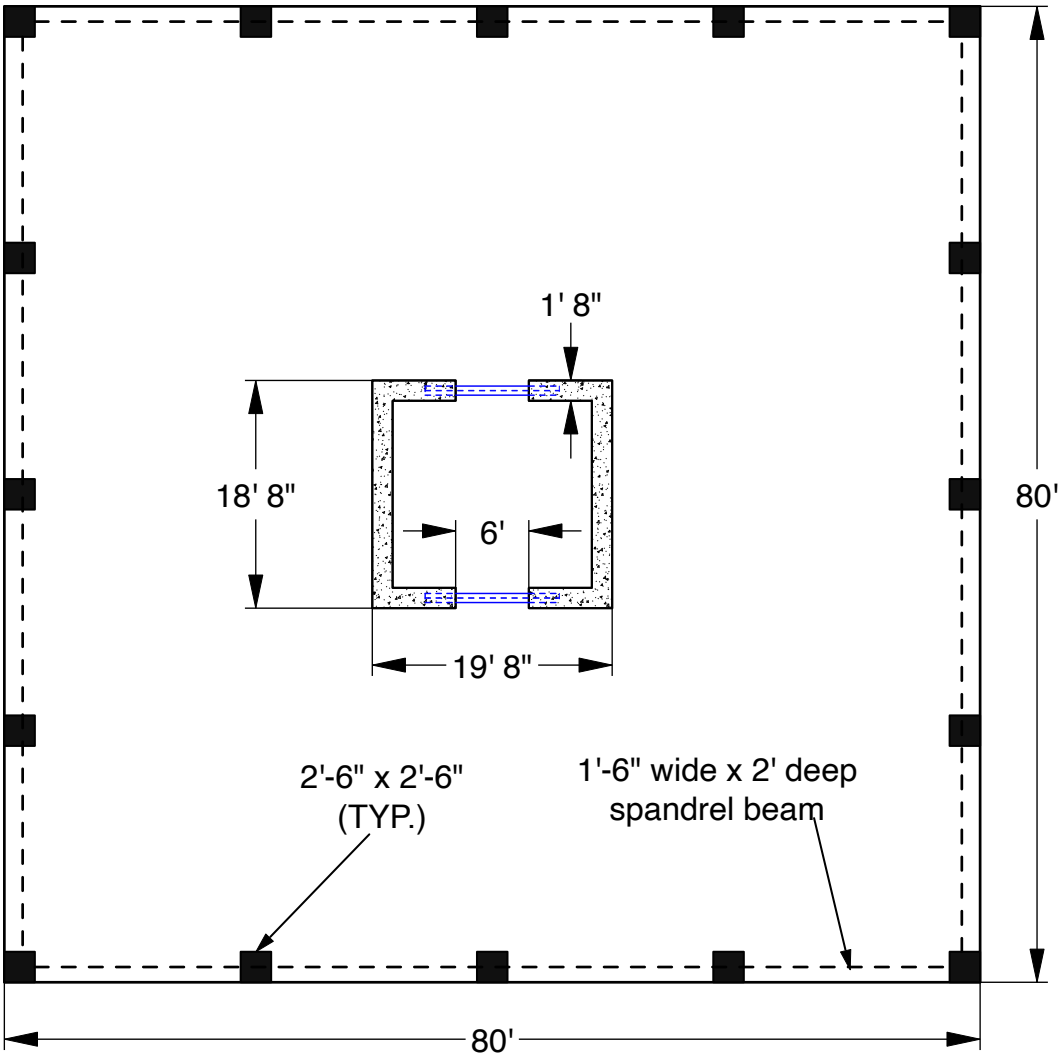

Figure 2.1 Archetype plan view.

Table 2.1 Wall reinforcement ratio.

Story	Reinforcement ratio (%)	
	Longitudinal	Transverse
1-3	0.92	0.41
4-6	0.68	0.25
7-8	0.43	0.25
9-25	0.25	0.25

Table 2.2 Summary of coupling beam demands and capacities.

Group	Story	Beam size	Maximum shear demand in a group (kips)	Beam capacity (kips)
1	1-2	W12 x 53	53	98
2	3-9	W16 x 77	185	187
3	10-16	W14 x 74	142	157
4	17-25	W12 x 53	68	98

To highlight the differences between the 2010, 2016, and 2022 versions of AISC 341 *Seismic Provisions*, the required embedment lengths and reinforcement over the embedment portion (to control gap opening) are compared in Figure 2.2a and Figure 2.2b, respectively. As expected, AISC 341-10 requires the longest embedment lengths than those from AISC 341-16 and AISC 341-22 because the embedment lengths are determined to develop the member capacity according to AISC 341-10. There is no difference between the development lengths from AISC 341-16 and AISC 341-22 except for cases that are controlled by the minimum depth requirement of AISC 341-22. The amount of reinforcement needed to control gap opening based on AISC-22 is noticeably larger than the other two versions. On average, AISC 341-22 provisions require 3.8 times and 2.1 times larger longitudinal reinforcement than AISC 341-16 and AISC 341-10, respectively.

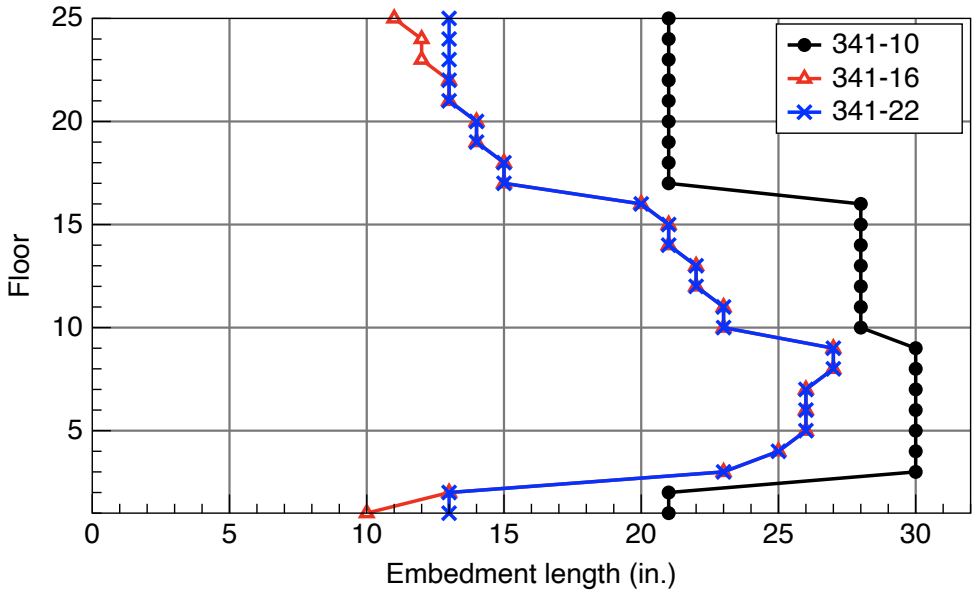

(a) Embedment length.

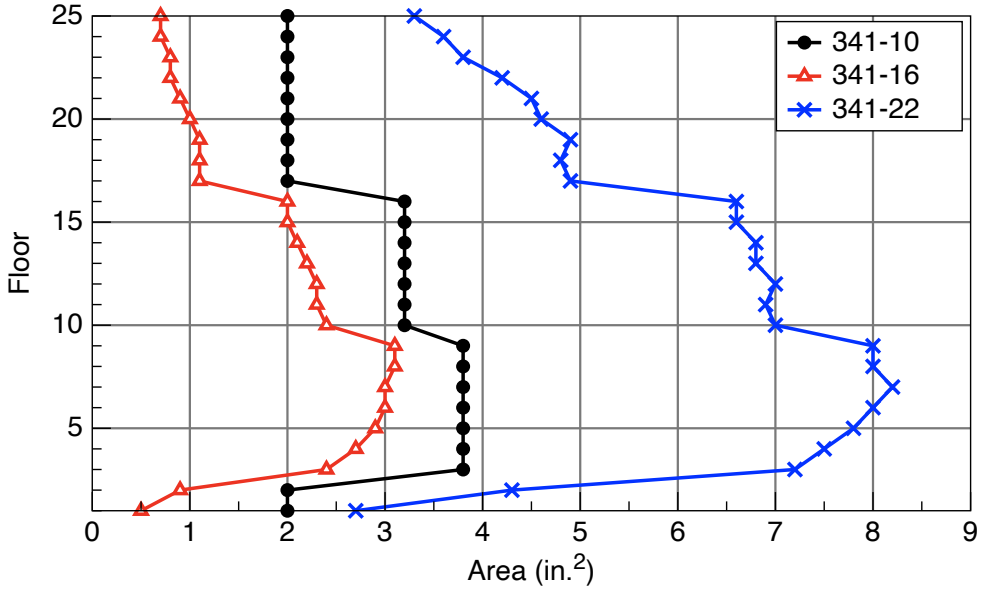

(b) Reinforcement for controlling gap opening.

Figure 2.2 Comparisons of ASIC 341-10, AISC 341-16, and AISC 341-22.

2.3 Test specimens

A total of six specimens were fabricated in two phases, two in phase 1 and four in phase 2. The specimens in both phases consisted of a portion of the wall pier and one-half of a steel coupling beam embedded in the wall pier. The specimens in phase 1 had two coupling beams,

one at each end of the wall pier. One connection was designed according to AISC 341-16 and the other one based on AISC 341-22. Each coupling beam was tested separately; hence, four different tests were conducted in the first phase. Four specimens were fabricated and tested in the second phase. Therefore, the data from eight tests were obtained. There were major differences in terms of loading, scale, and overall configuration of the specimens in phase 1 and phase 2. Therefore, the specimens from the two phases are described separately.

2.3.1 Phase 1 specimens

Two half-scale specimens were tested in the first phase. Specimens 1a and 1b were selected based on the demands in the 24th story to simulate cases with short embedment lengths. Specimens 2a and 2b were based on the demands and wall details in the 9th story of the archetype because the wall at this location is governed by minimum reinforcement but coupling beam has the largest shear force. The design forces from these two floors were used to proportion the specimens. Additional details are provided in Kunwar (2020).

2.3.1.1 Wall pier

The walls in the archetype are C-shaped whereas a rectangular wall was chosen in the test specimens. The rectangular wall represents one flange of the C-shaped walls. As a result, standard similitude concepts cannot be used to determine the wall reinforcement for the half-scale test specimens. Considering that the amount of wall reinforcement is expected to influence the performance of coupling beam-wall connection, it was decided to maintain the same percentage of wall reinforcement in the test specimen and one flange of the archetype C-shaped wall. The wall thickness was taken as 10 in. to represent half-scale equivalent of the archetype wall thickness of 20 in. The other dimensions were selected based on constraints such as the spacing of tie downs of the laboratory's strong floor, dimensions of hydraulic actuators, etc. The wall geometry and reinforcement for specimens 1a and 1b and specimens 2a and 2b are shown in

Figure 2.3 and Figure 2.4, respectively. Photographs in Figure 2.5 show various stages of fabrication of the first phase specimens.

2.3.1.2 Coupling beams

The shear force in a half-scale coupling beam is equivalent to the full-scale value divided by 4. Using the scaled shear force, the coupling beams were designed and detailed according to AISC 341-16 and AISC 341-22. W8x21 (to represent story 9) and W6x16 (to represent story 24) were selected based on having adequate strength and matching as close as possible the ½-scale equivalents[1] of key cross-sectional properties of the full-scale beams as close as possible.

2.3.1.3 Embedment length and detailing

As discussed previously, each specimen has two coupling beams – one designed and detailed according to AISC 341-16 and the other one based on AISC 341-22. The details of coupling beam-wall pier connection as well as additional wall longitudinal reinforcement, if any, are summarized in Table 2.3.

Table 2.3 Phase 1 test matrix and wall-beam connection details.

Specimen ID	Test ID	Story in archetype	Governing code	Coupling beam	Embedment length (in.)	Additional reinforcement
1a	Test 1	24	341-16	W6x16	6	----
1b	Test 2	24	341-22	W6x16	7	4 No. 3
2a	Test 3	9	341-16	W8x21	13	2 No. 3
2b	Test 4	9	341-22	W8x21	13	2 No. 4 and 4 No. 5

[1] Dimensions = ½ of full-scale values, area = ¼ of full-scale area, plastic section modulus = 1/8 of full-scale value, moment of inertia = 1/16 of full-scale value

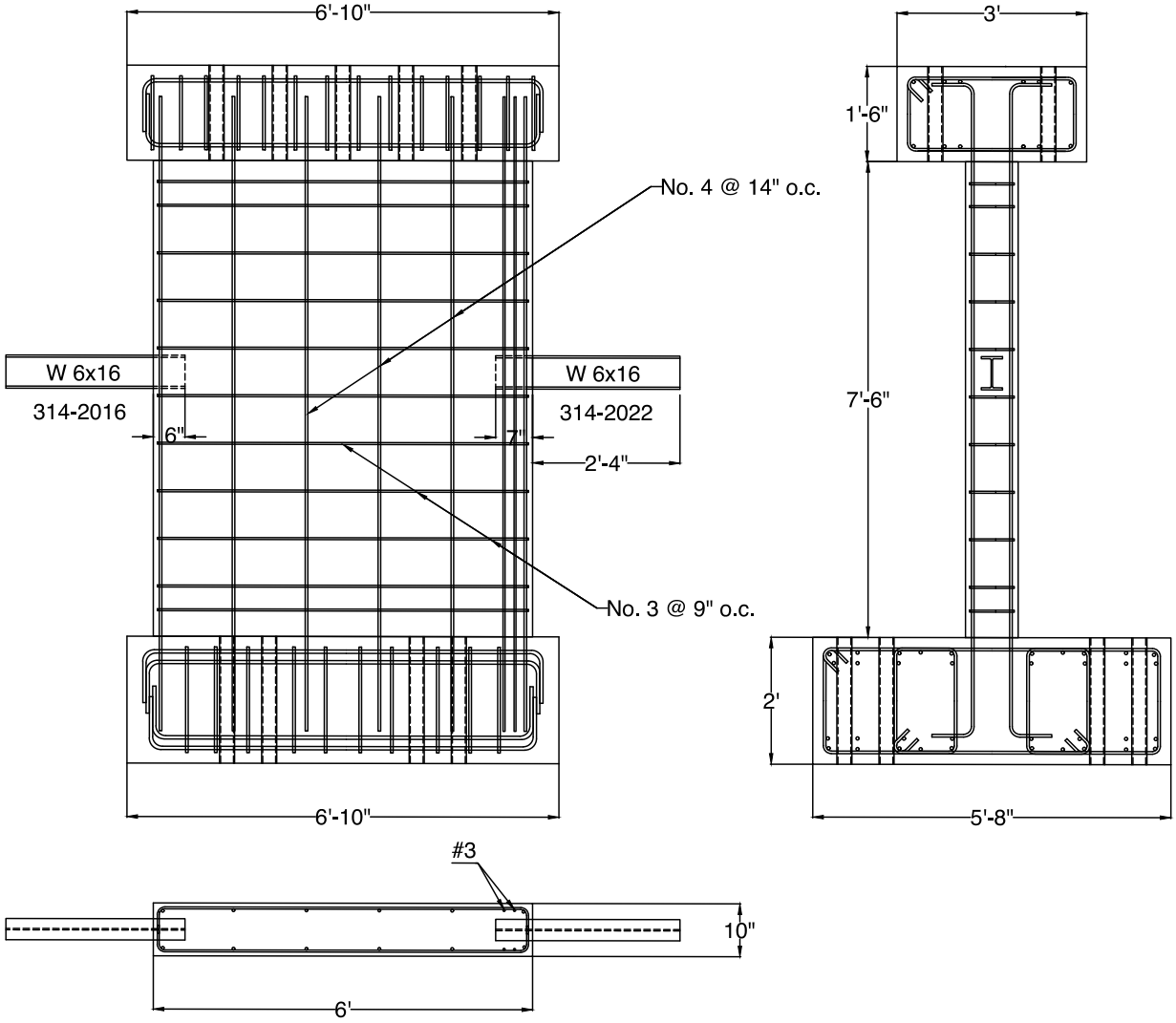

Figure 2.3 Details of specimens 1a and 1b (tests 1 and 2).

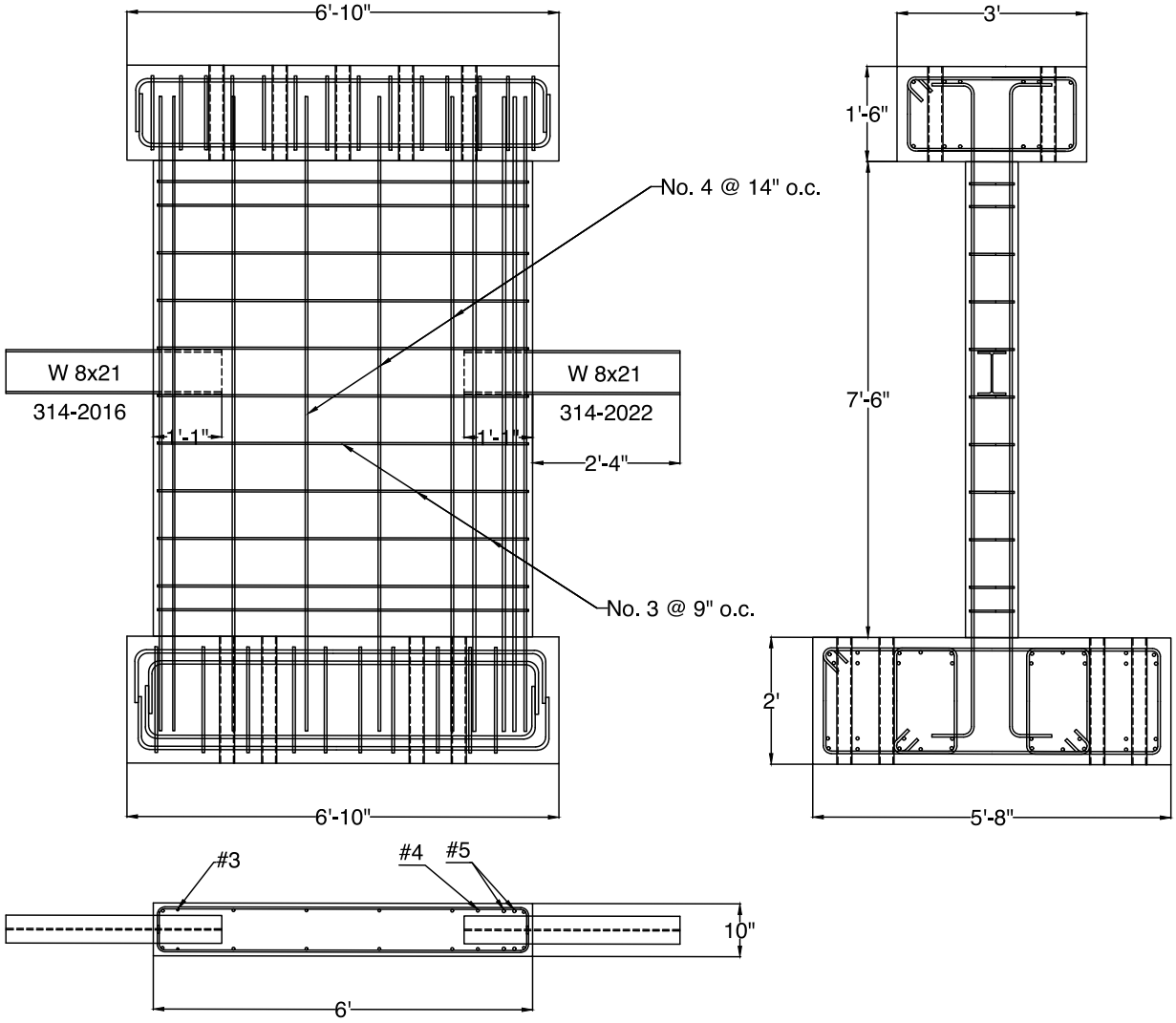

Figure 2.4 Details of specimens 2a and 2b (tests 3 and 4).

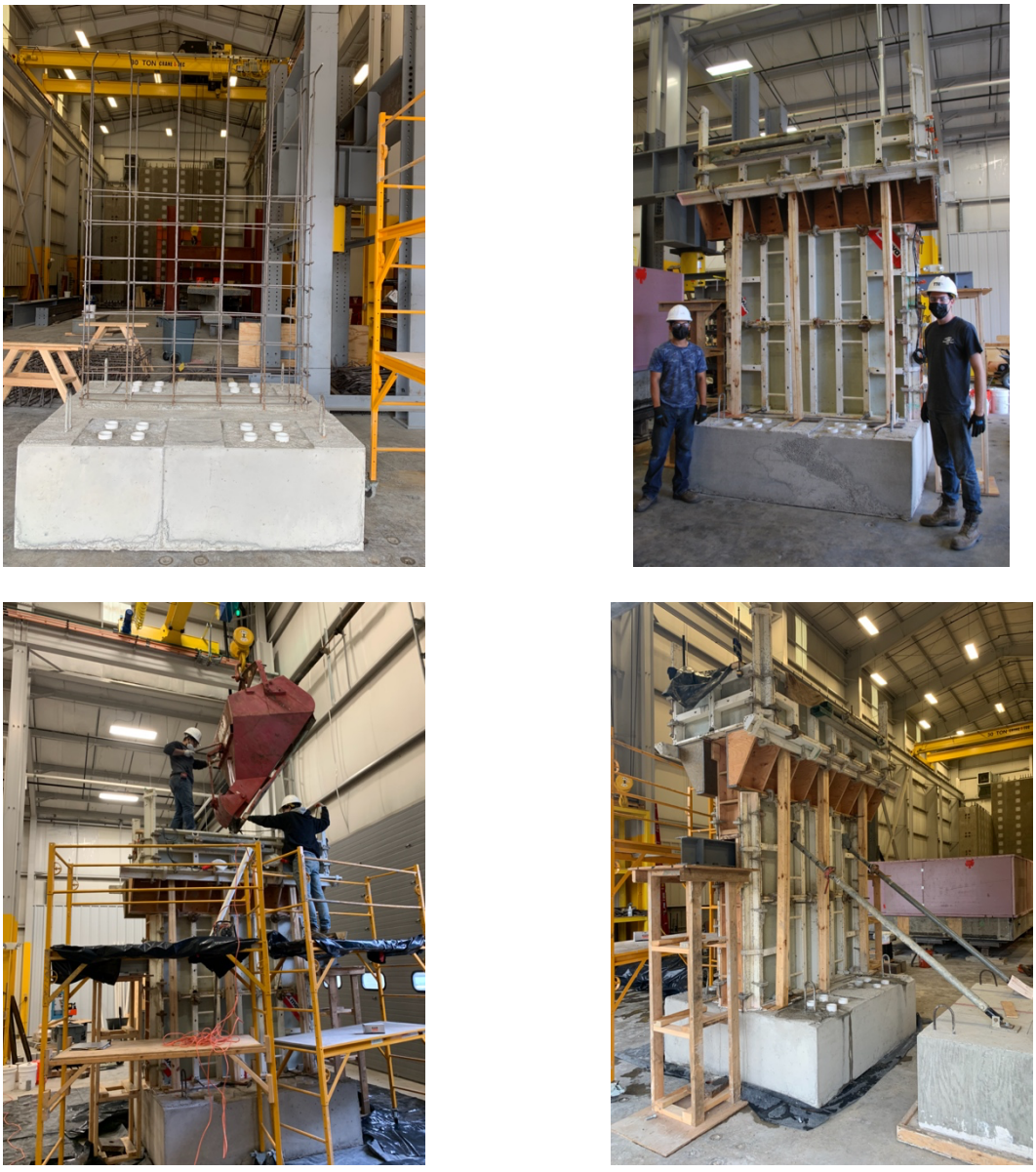

Figure 2.5 Fabrication of first-phase specimens.

2.3.2 Phase 2 specimens

The maximum coupling beam shear demand is in story 9 of the archetype. The test specimens were designed and detailed based on the demands in this story and corresponding wall reinforcement. The specimens in the second phase are approximately ¾ scale, whereas ½-scale specimens were used in the first phase. The test matrix is summarized in Table 2.4. Based on the observations made in the first phase (discussed in Chapter 3), it was decided to add face-

bearing plates in all the second phase specimens. The embedment length was determined using the current AISC 341 (2022) equation (Eq 2.1) and a revised equation (Eq 2.2). Derivation of the revised equation is provided in Appendix A. The calculated embedment length according to ASIC 341 and the revised equation is 19 in. and 24 in., respectively.

$$\text{AISC 341-22} \quad V_n = 1.54\sqrt{f_c'}\left(\frac{b_w}{b_f}\right)^{0.66}\beta_1 b_f L_e\left[\frac{0.58-0.22\beta_1}{0.88+\frac{g}{2L_e}}\right] \qquad \textbf{Eq 2.1}$$

$$\text{Revised} \qquad V_n = \frac{0.227 f_c' b_f L_e}{0.845+\frac{g}{2L_e}} \qquad \textbf{Eq 2.2}$$

Table 2.4 Phase 2 test matrix.

Specimen ID	Test ID	Embedment length	Auxiliary transfer reinforcement	Confinement	Face bearing plate
3	5	AISC 341-22	No	No	Yes
4	6	Revised	No	No	Yes
5	7	AISC 341-22	Yes	No	Yes
6	8	AISC 341-22	No	Yes	Yes

The amount of auxiliary transfer reinforcement was calculated using Eq 2.3, which is the same as Eq. H5-3 in AISC 341-2022. The auxiliary transfer reinforcement was added to mitigate stiffness degradation observed in the first phase (discussed in Chapter 3). Considering that stiffness is primarily a serviceability issue, F_{ysr} was taken as $0.5F_{ysr}$, i.e., 30 ksi for ASTM A615 Gr. 60 reinforcement that was used. A total of 8 No. 5 bars (4 on each flange) were used. The manufacturer had threaded the bars into couplers and torqued them according to their specifications. The coupler of the assembly was welded to the flanges before placing the coupling beam in the form. In actual construction, couplers would have been welded to the flanges before threading and torquing the headed bars.

$$A_{tb} \geq 0.03 f_c' L_e b_f / F_{ysr} \qquad \textbf{Eq 2.3}$$

Confinement in specimen 6 (test ID 8) consisted of two layers of cross ties along the embedment length. Confinement was provided for both flanges. Specimen details and photographs before casting are shown in Figure 2.6 and Figure 2.7, respectively.

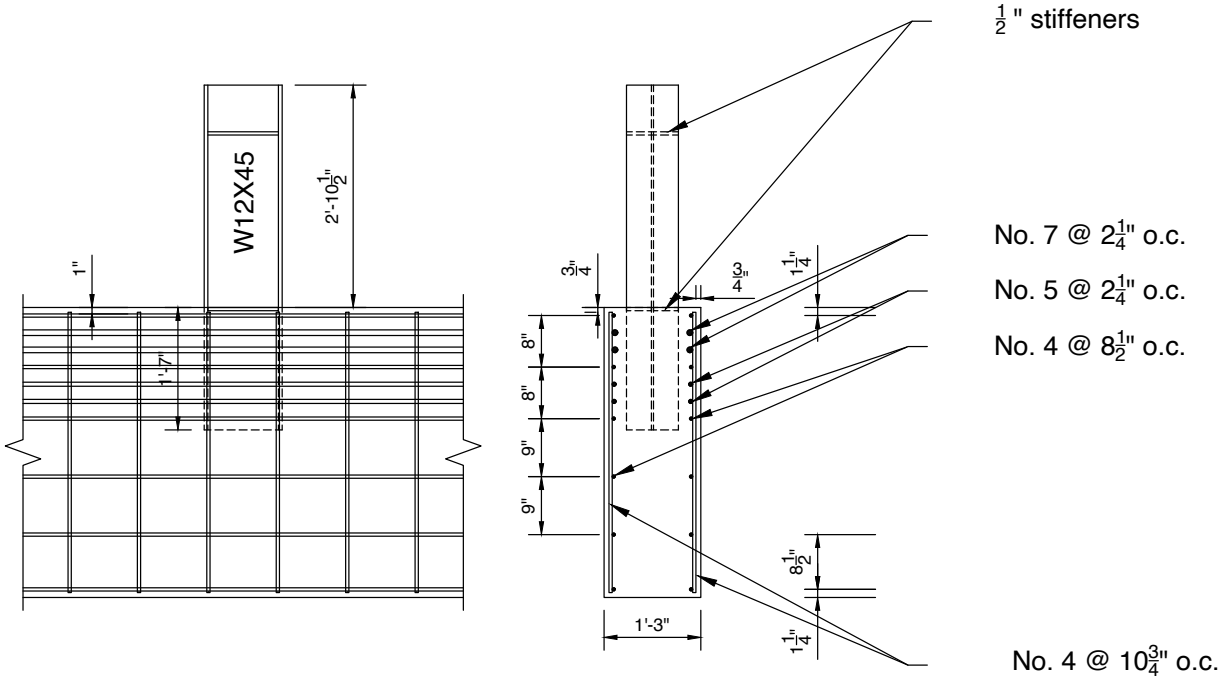

(a) Specimen 3 (test 5)

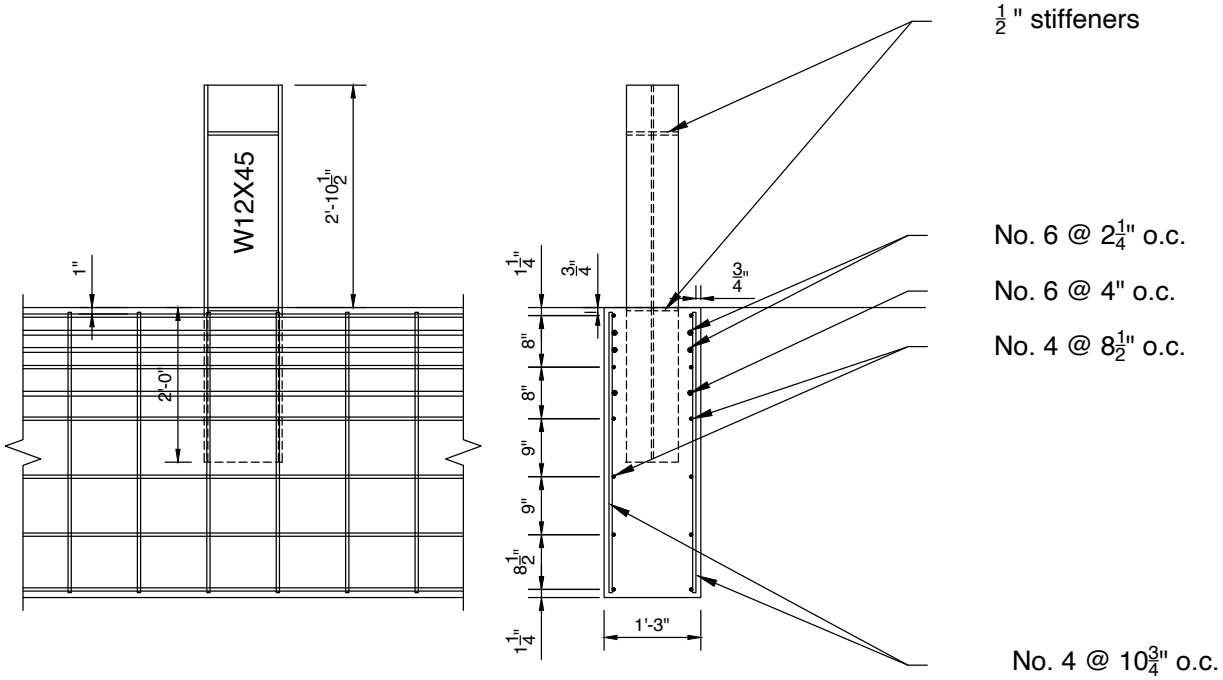

(b) Specimen 4 (test 6)

Figure 2.6 Specimen details.

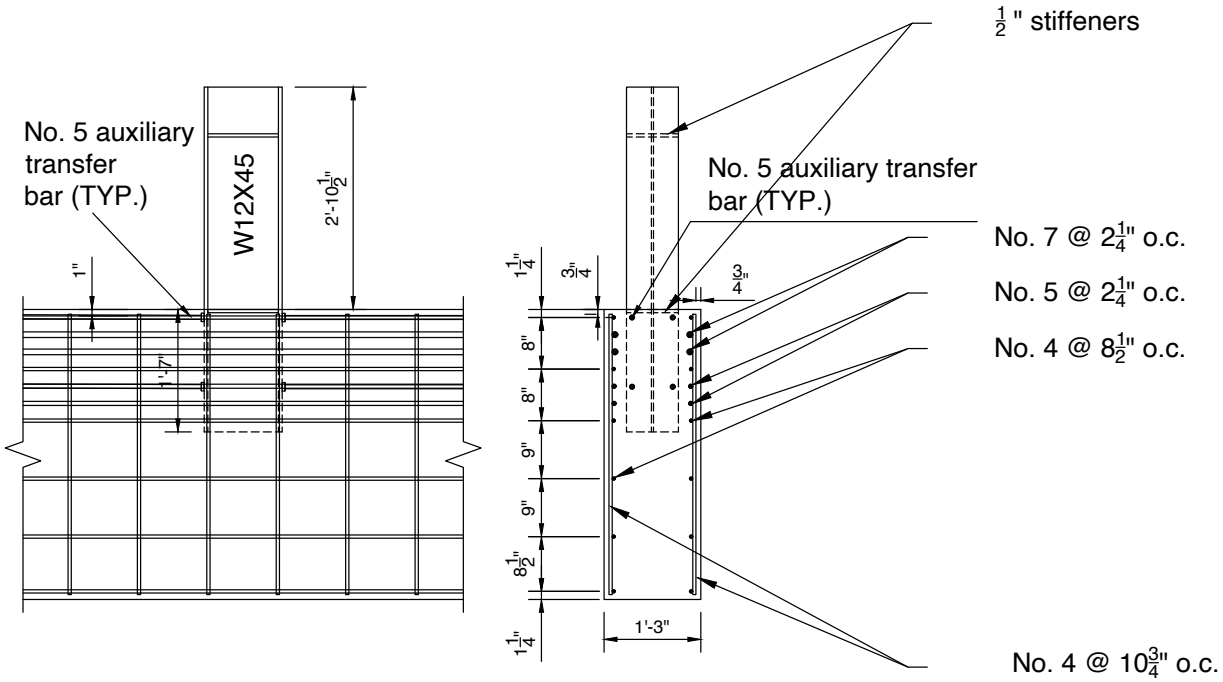

Auxiliary transfer bars will be as close as possible to the web while maintaining ACI spacing requirements for headed bars

(c) Specimen 5 (test 7)

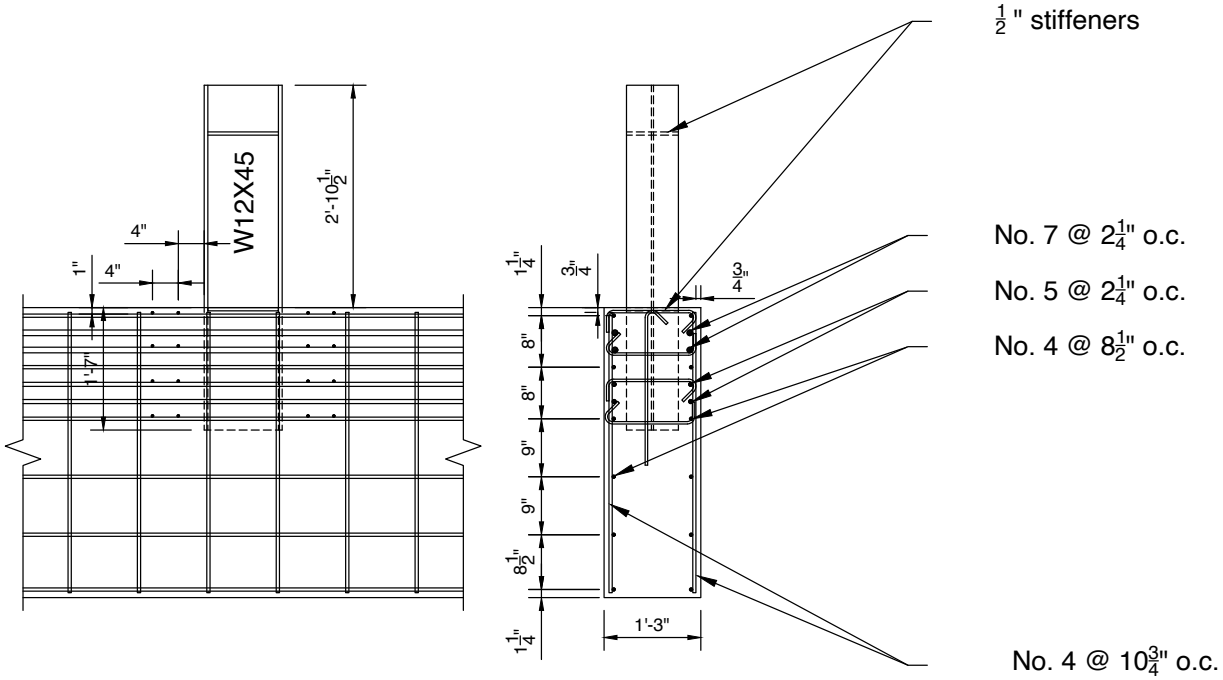

(d) Specimen 6 (test 8)

Figure 2.6 Specimen details (cont.).

(a) Specimen 4 (test 6) [specimen 3 (test 5) was similar but with a shorter embedment length]

(b) Specimen 5 (test 7)

(c) Specimen 6 (test 8)

Figure 2.7. Photographs of specimens before casting

2.4 Material properties

Design concrete compressive strength (f'_c) was 5,000 psi. The reinforcing bars were A615 Gr. 60 and structural steel was A572 Gr. 50. The material properties were determined by testing samples according to the relevant ASTM test methods.

2.4.1 Concrete

The concrete compressive strength was determined using "field cured" 6-in. diameter by 12-in. high cylinders and 4-in. diameter by 8-in. high cylinders tested in accordance with ASTM C39 (2021). Additionally, 4-in. cores were obtained from a number of the test specimens. The cores were tested and processed according to ASTM C42 (2020). Splitting tensile strength was determined using ASTM C496 (2017). The measured compressive and tensile strengths are summarized in Table 2.5.

Table 2.5 Measured concrete compressive and tensile strengths.

Specimen ID	Test ID	Compressive Strength (psi)	Tensile Strength (psi)
1a	1	4133[a]	363
1b	2	4133[a]	363
2a	3	6954[b]	529
2b	4	6954[b]	529
3	5	6983[a]	520
4	6	4700[b]	460
5	7	6730[a]	450
6	8	6150[c]	480

[a] from cylinders (ASTM C39)
[b] from cores (ASTM C42)
[c] average of the strengths from cylinders and cores

2.4.2 Reinforcement

Full-section specimens were tested according to ASTM A370 (2022). The values of yield strength (f_y), ultimate strength (f_u), and rupture strain are summarized in Table 2.6. These values

are the averages from three samples. The measured stress-strain diagrams are provided in Appendix B.

Table 2.6 Measured material properties of reinforcement.

Phase	size	f_y (ksi)		f_u (ksi)		rupture strain	
		Average	COV	Average	COV	Average	COV
1	#3	75.3	0.021	97.0	0.0068	0.123	0.405
	#4	76.7	0.026	105.6	0.0017	0.118	0.460
	#5	71.9	0.031	101.0	0.0073	0.096	0.109
2	#3	75.3	0.021	97.0	0.0068	0.123	0.405
	#4	71.5	na[a]	100	0.017	nr[b]	na
	#5	70.2	0.005	86.3	0.004	> 0.1225[c]	na
	#6	71.4	0.004	88.1	0.003	> 0.1265	na
	#7	75.2	0.005	91	0.004	> 0.1375	na
	[a] due to issues with extensometer, yield strength could be obtained from only one sample. [b] the value was not reported. [c] rupture occurred outside of the gage length						

2.4.3 Structural Steel

Using subsize specimens fabricated and tested according to ASTM E8 (2022), the yield and ultimate strength of the flanges and webs of the steel coupling beams were determined. The results, which are the average values from testing two samples, are tabulated in Table 2.7. The measured stress-strain diagrams are shown in Appendix B.

Table 2.7 Measured material properties of steel coupling beams.

Phase	Specimen I.D.	Test I.D.	Shape	Location	F_y (ksi)	F_u (ksi)
1	1a, 1b	1, 2	W6×16	Flange	52.8	66.9
				Web	60.1	72.5
	2a, 2b	3, 4	W8×21	Flange	58.8	75.9
				Web	63.8	79.1
2	3, 4, 5, 6	5, 6, 7, 8	W12×45	Flange	53.6	68.1
				Web	56.8	70.2

2.5 Test setup

Two vastly different setups were utilized for testing the specimens in phase 1 and phase 2. The test setups are described separately in this section.

2.5.1 Phase 1 test setup

Four servo-valve controlled actuators were used to load the coupling beam and subject the wall pier to gravity load, axial force, shear force, and bending moment, refer to Figure 2.8. Actuator 1 was controlled to follow a predefined load or displacement history. The force measured by this actuator, which is the shear force in the coupling beam, was used as the input to control the force in the other three actuators according to the relationships tabulated in Table 2.8. These relationships were determined to keep the stresses in the test specimen equal to those in the archetype. The procedure for determining these ratios is discussed in Appendix C.

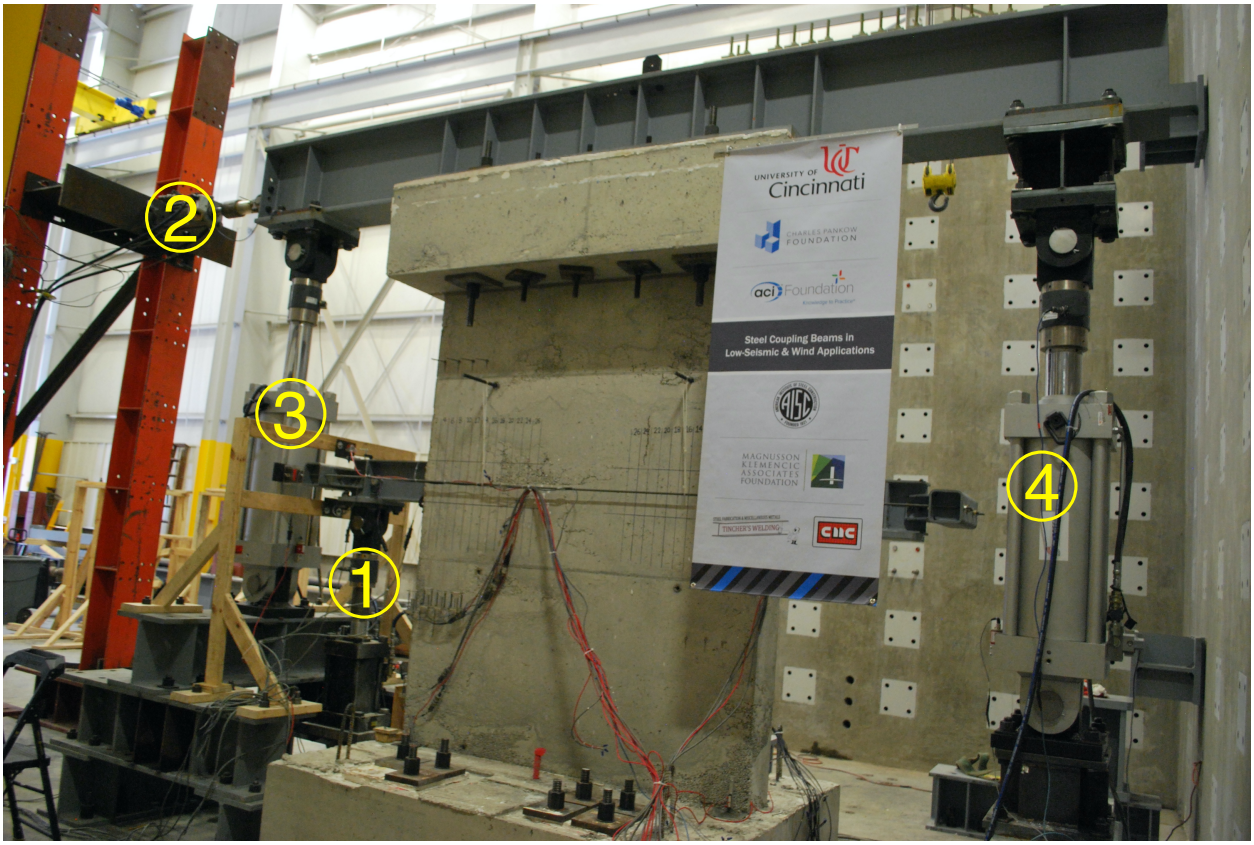

Figure 2.8 Test setup for specimens in phase 1.

Table 2.8 Force relationships between secondary and primary actuators.

Actuator (See Figure 2.8)	Relationships for Specimens 1a and 1b (test 1 and test 2)	Relationships for Specimen 2a and 2b (test 3 and test 4)
2	Force = 0.026 x force in actuator 1	Force = 0.143 x force in actuator 1
3	Force = 0.229 x force in actuator 1	Force = 0.682 x force in actuator 1
4	Force = 0.035 x force in actuator 1	Force = 0.831 x force in actuator 1

The directions of applied forces are provided in Figure 2.9. It should be noted that the wall curvature in specimens 1a and 1b, which represented the 24th floor connection, is opposite to that in the lower floors. Considering the complexity of simultaneous control of four actuators, a bespoke test frame was fabricated and used to debug programming of the controller. The four actuators during debugging process are shown in Figure 2.10. It was anticipated that the coupling beam would be "pulled out" of the wall when the primary actuator (actuator 1) pushes the beam up. This axial deformation would be restrained by the floor diaphragm in the archetype. Therefore, an assembly was mounted to restrain the axial deformation. A pair of assemblies were bolted to the coupling beams at each end of the wall pier and were connected by 5/8-in. A193-B7 threaded rods, see Figure 2.11. A similar concept has been used by other researchers (Motter, 2013).

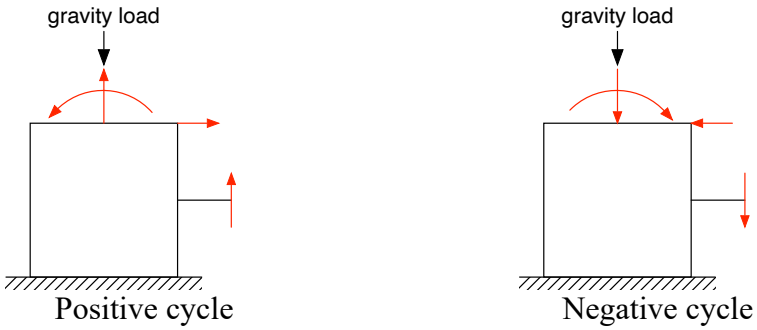

(a) Specimens 1a and 1b – Floor 24 (test 1 and test 2)

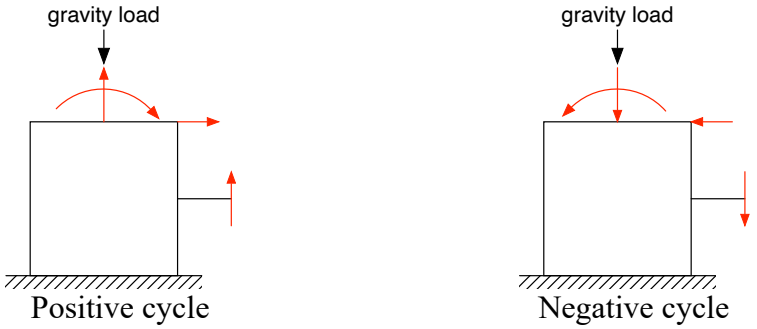

(b) Specimens 2a and 2b – Floor 9 (test 3 and test 4)

Figure 2.9 Direction of applied forces and moment.

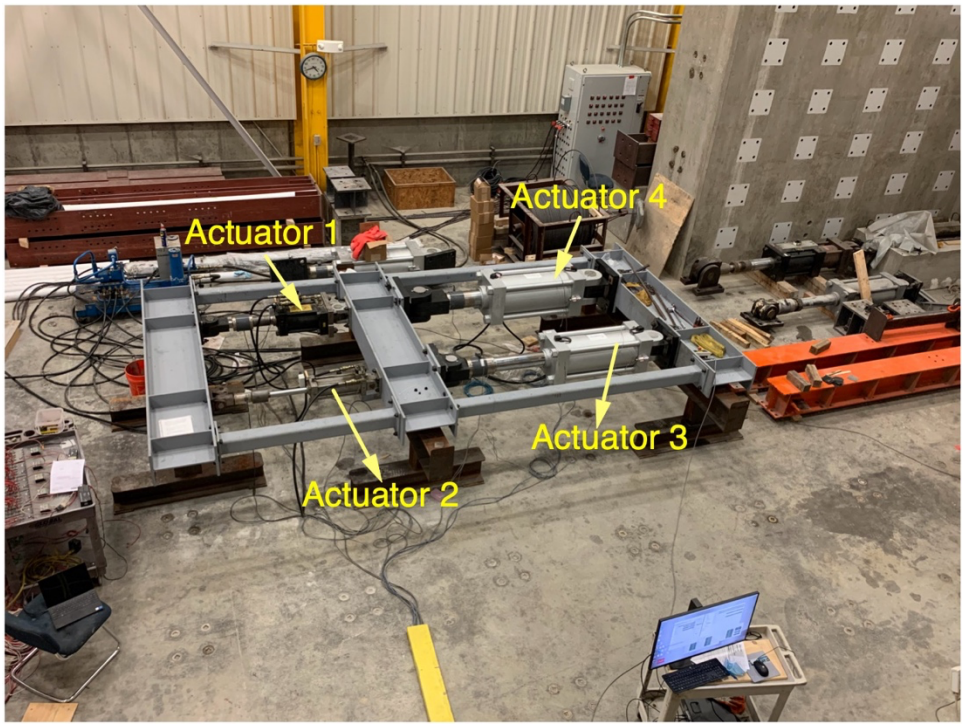

Figure 2.10 Setup for debugging controller.

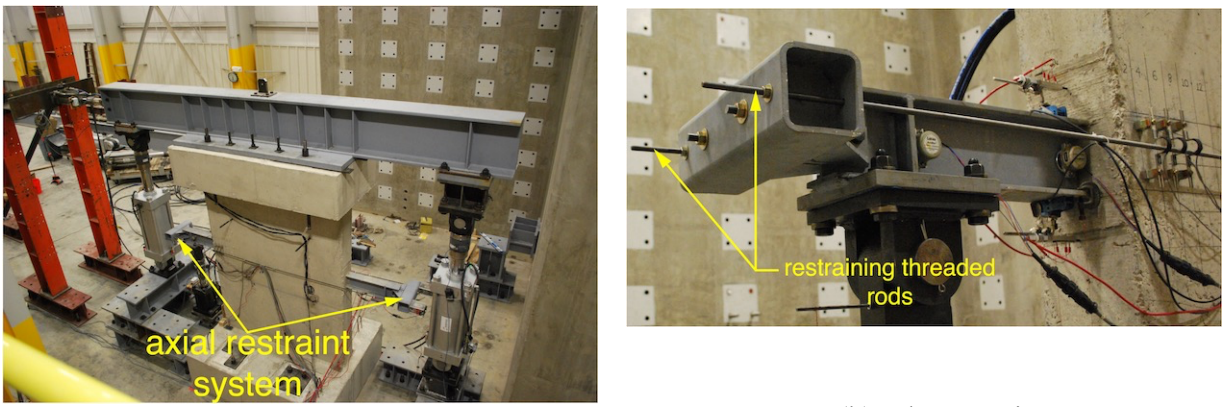

(a) Overall view (b) Closeup view

Figure 2.11 Coupling beam axial deformation restraint apparatus for phase 1 specimens.

2.5.2 Phase 2 test setup

The test specimen was post-tensioned to the laboratory's strong floor using two strong "tie backs". A constant axial load was applied by using eight 1-in. high-strength threaded rods. The level of applied axial load was intended to match the axial stress at the 9th story of the archetype. A single servo-controlled actuator was used to apply load and displacement cycles to the coupling beam. The test setup is shown in Figure 4.1. The positive direction of applied load and displacement is indicated in this figure.

Figure 2.12 Test setup for specimens in phase 2.

Similar to phase 1 specimens, the axial deformation of the coupling beam was restrained. As seen from Figure 2.13, the apparatus consisted of a strong tie back beam that was bolted to the coupling beam. A pair of 1-in. high-strength threaded rods connected the strong tie-back beam to the bottom of the wall. Universal joints in line with the threaded rods were used to minimize deformation of the rods.

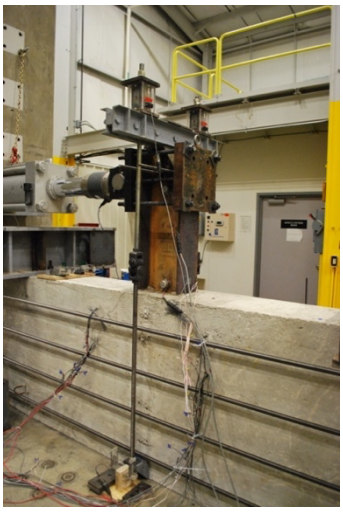

(a) Overview

(b) Universal joint in line with threaded rods

Figure 2.13 Coupling beam axial deformation restraint apparatus for phase 2 specimens.

2.6 Instrumentation

Various internal and external sensors were installed to measure several key responses. Strain gages were attached to the wall longitudinal reinforcement at various locations and auxiliary transfer bars (for phase 2 specimen 5 [test 7]), see Figure 2.14. The gages were located at 2 in. from the flanges. The strain gages for the auxiliary transfers were placed at the development length. Strain gages were also attached to the coupling beam flanges at 1 in. from the face of the wall. Strain gage rosettes, also at 1 in. above the wall, were also installed on the web of the phase 2 specimens.

The following external instruments were utilized to monitor various responses: (a) actuator's load cell and displacement transducer measured the applied force and resulting

displacement, (b) external displacement transducers were used to measure the deflection of the coupling beam at the location of applied shear force, (c) tilt meters recorded the coupling beam rotation, (d) displacement transducers monitored the axial deformation of the coupling beam, (e) sensors were used to measure the horizontal displacement of the flange relative to the wall, (f) load cells recorded the force required to restrain coupling beam axial deformation, (g) potential uplift of the wall was measured by vertical displacement transducers attached to the specimen and targeted against the strong floor, and (h) potential slip of the specimen relative to the strong floor was monitored by displacement transducers. In phase 1 specimens, concrete strain along the embedment length using clip gages, which did not measure reliable data due to spalling and damage around the embedment length, or vertical DC LVDTs. The external instrumentations are illustrated in Figure 2.15 and Figure 2.16 for phase 1 and phase 2 specimens, respectively. The locations of these sensors are provided in Figure 2.17, Figure 2.18, and Figure 2.19.

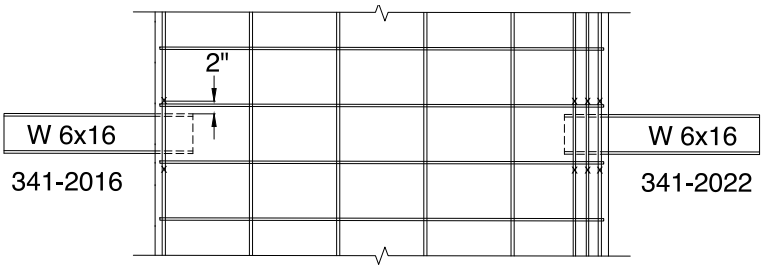

(a) Specimens 1a and 1b (test 1 and test 2)

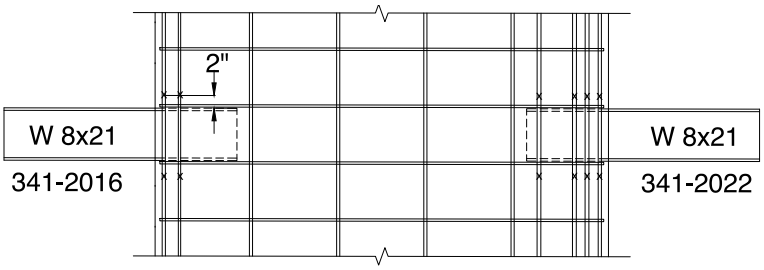

(b) Specimens 2a and 2b (test 3 and test 4)

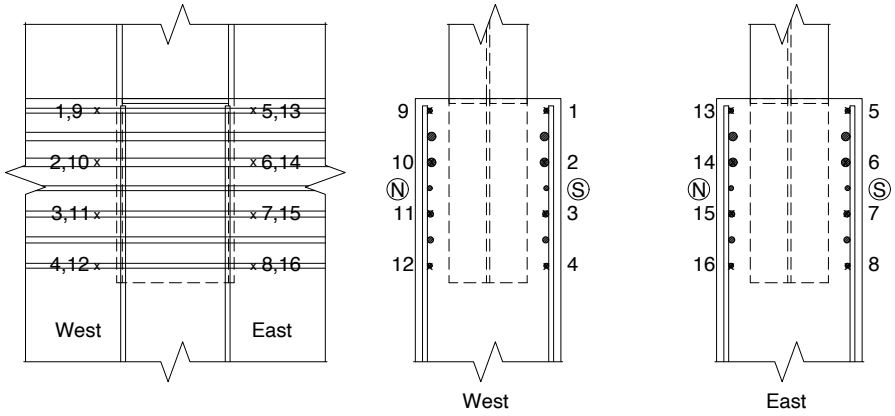

(c) Specimen 3 (test 5)

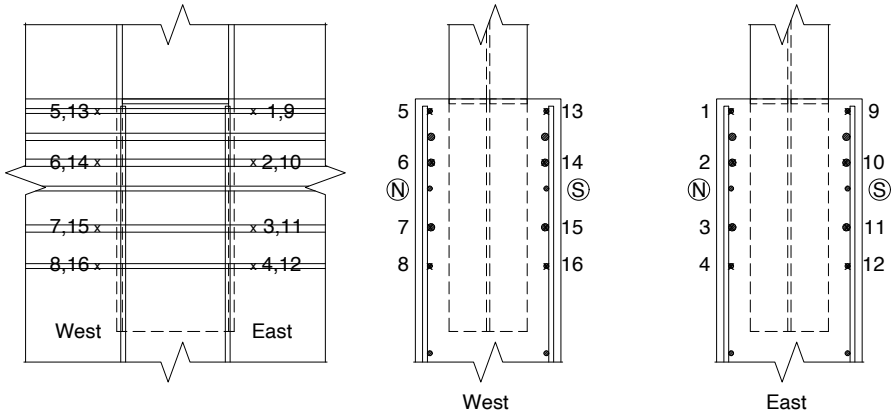

(d) Specimen 4 (test 6)

Figure 2.14 Locations of strain gages shown with x.

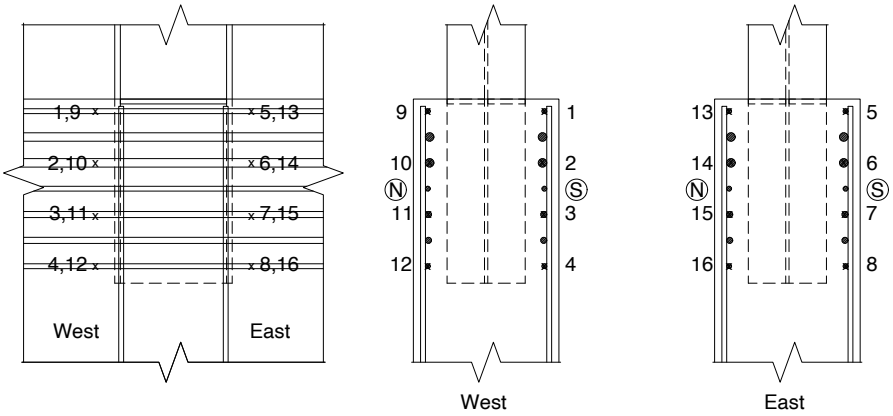

(e) Specimen 5 (test 7)

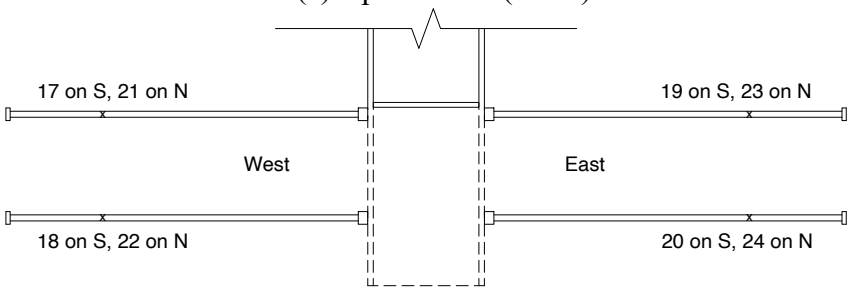

(f) Specimen 5 (test 7) – auxiliary transfer bars0

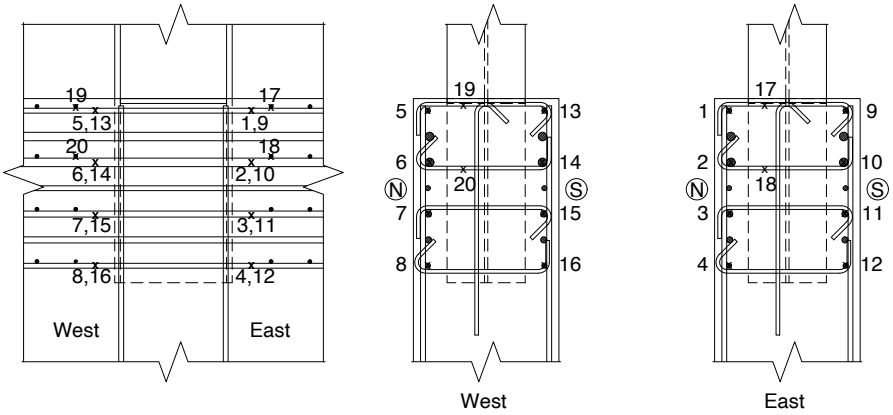

(g) Specimen 6 (test 8)

Figure 2.14 Locations of strain gages shown with x (cont.).

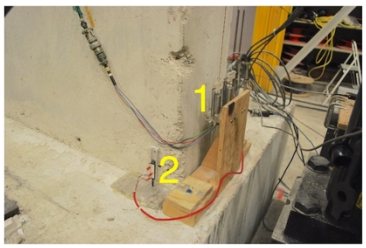

(a) 1: transducer for measuring beam deflection at support, 2: transducer for measuring potential wall uplift

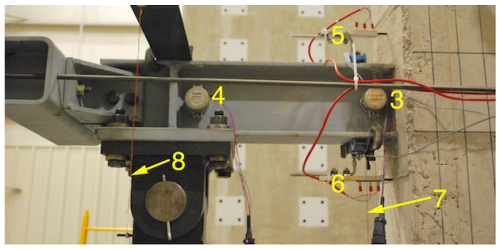

(b) 3 & 4: tilt meters for measuring rotations, 5 & 6: transducers for determining initiation of spalling, 7: copper wire for sensor 1 (see a), 8: copper wire for sensor 9 (see c)

(c) 9: additional measurement of beam deflection at load point

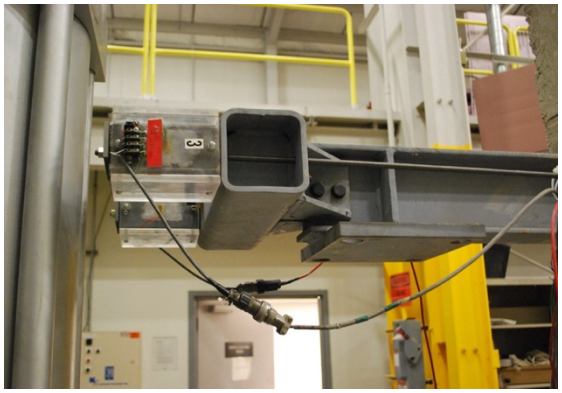

(d) measurement of coupling beam axial force

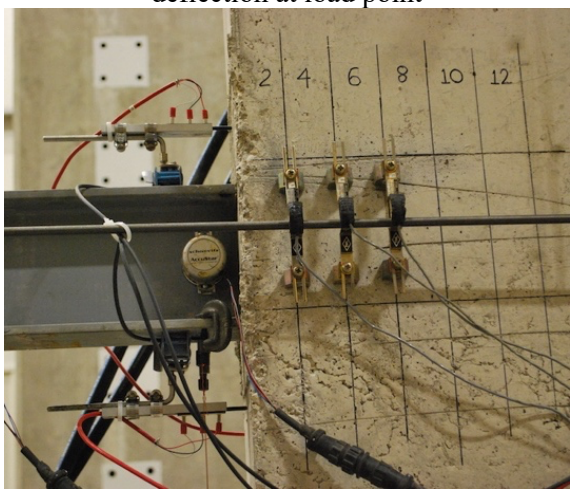

(e) Measurement of concrete surface strain Specimens 1a and 1b (tests 1 and 2): clip gages

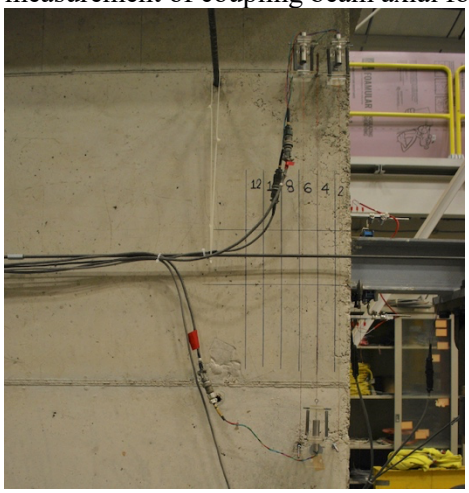

(f) Measurement of concrete surface strain Specimens 2a and 2b (tests 3 and 4): DC LVDTs

Figure 2.15 External instrumentation for phase 1 specimens.

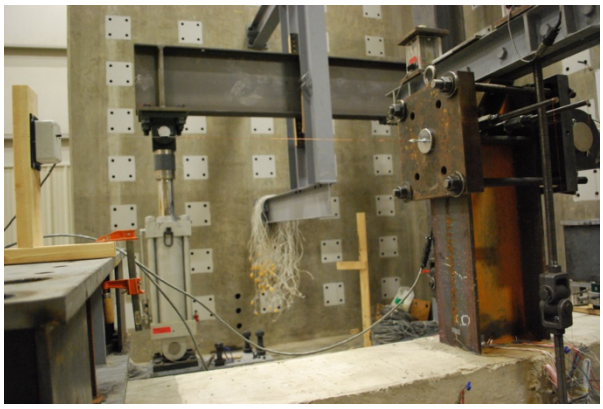

(a) External displacement transducer to measure beam deflection

(b) Tilt meters

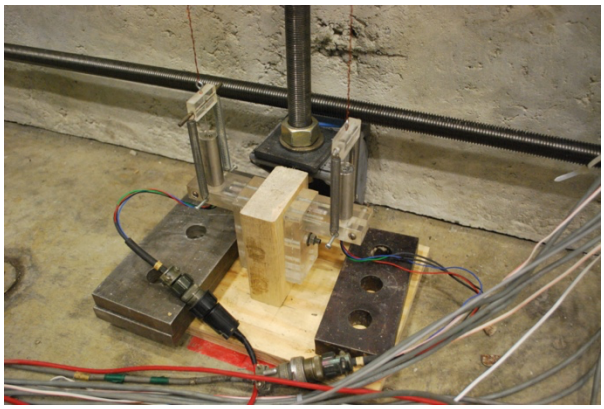

(c) Two out of four displacement transducers used to monitor beam axial deformation

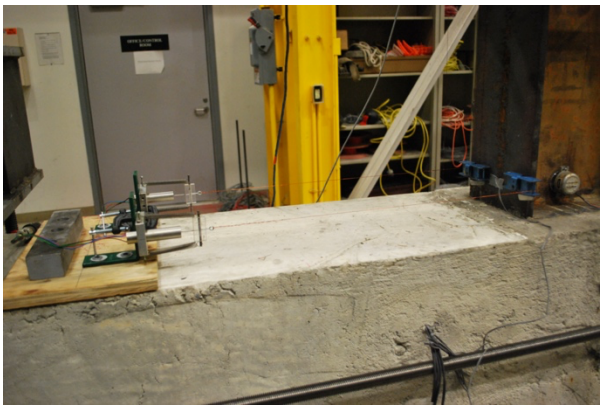

(d) Displacement transducers to measure deflection of the beam near its base

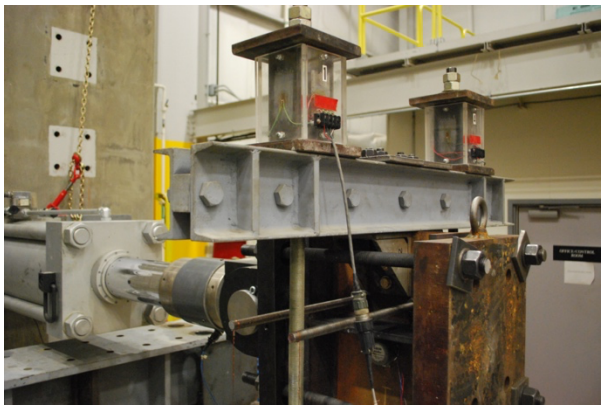

(e) Load cells to measure force in axial restraining apparatus

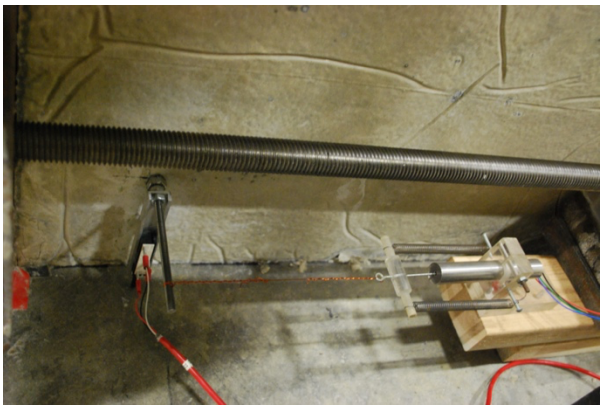

(f) Displacement transducers to monitor potential wall uplift and slip

Figure 2.16 External instrumentation for phase 2 specimens.

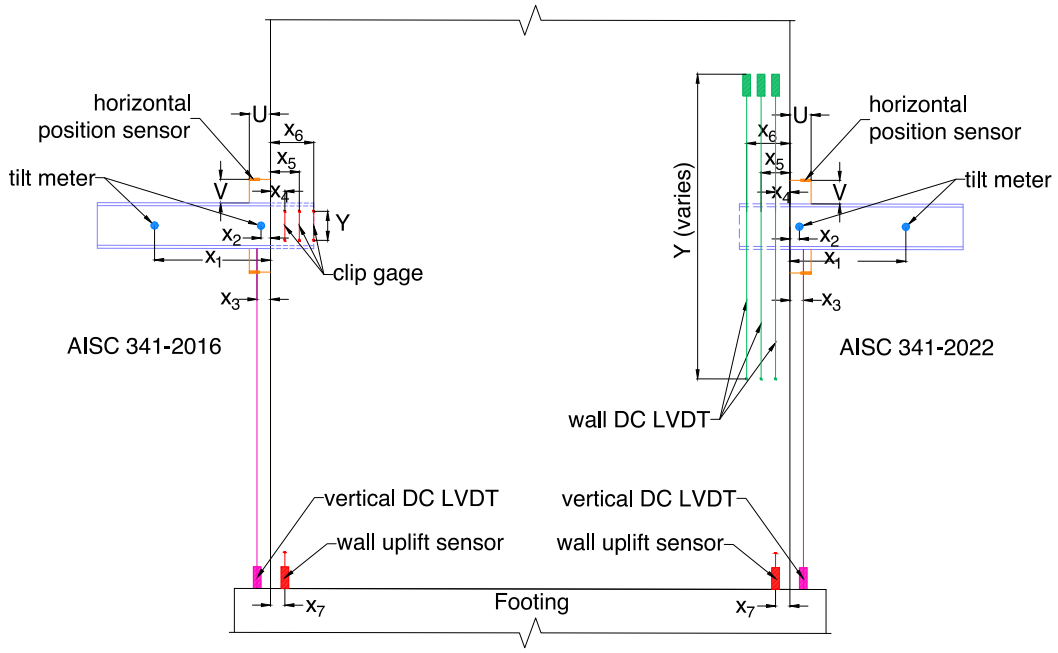

Sensors for specimen 1a (AISC 341-2016)	**Position**	
Tilt meter 1	X_1 = 16-1/16 in.	
Tilt meter 2	X_2 = 1-1/16 in.	
Vertical DC LVDT	X_3 = 1-7/8 in.	
Clip gage 1	X_4 = 2 in.	Y = 4 in. (south and north faces)
Clip gage 2	X_5 = 4 in.	Y = 4 in. (south and north faces)
Clip gage 3	X_6 = 6 in.	Y = 4 in. (south and north faces)
Wall uplift sensor	X_7 = 2 in.	
Horizontal position sensor (top and bottom)	U = 2-15/16 in.	V = 3-1/4 in.
Sensors for specimen 1b (AISC 341-2022)	**Position**	
Tilt meter 1	X_1 = 16-1/16 in.	
Tilt meter 2	X_2 = 1-1/16 in.	
Vertical DC LVDT	X_3 = 1-7/8 in.	
Wall DC LVDT 1	X_4 = 2 in.	Y = 42-13/16 in. (south face) Y = 42-1/16 in. (north face)
Wall DC LVDT 2	X_5 = 4 in.	could not be installed on the south face Y = 42-15/16 in. (north face)
Wall DC LVDT 3	X_6 = 6 in.	Y = 43-1/16 in. (south face) Y = 42-15/16 in. (north face)
Wall uplift sensor	X_7 = 2 in.	
Horizontal position sensor (top and bottom)	U = 2-15/16 in.	V = 3-1/4 in.

Figure 2.17 Locations of external instruments for specimens 1a and 1b (test 1 and test 2).

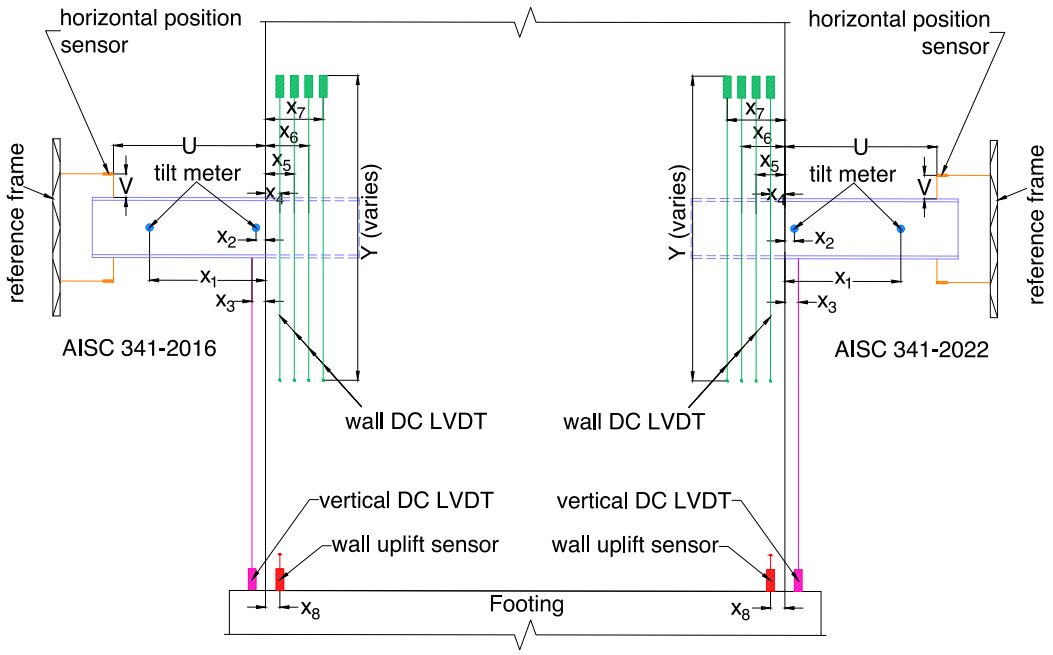

Sensors for specimen 2a (AISC 341-2016)	Position	
Tilt meter 1	X_1 = 16-1/16 in.	
Tilt meter 2	X_2 = 1-5/16 in.	
Vertical DC LVDT	X_3 = 2 in.	
Wall DC LVDT 1	X_4 = 2 in. (south face) X_4 = 2 in. (north face)	Y = 48-1/4 in. (south face) Y = 48-1/4 in. (north face)
Wall DC LVDT 2	X_5 = 5.5 in. (south face) X_5 = 6 in. (north face)	Y = 48-1/4 In. (south face) Y = 48-1/4 In. (north face)
Wall DC LVDT 3	X_6 = 9 in. (south face) X_6 = 9 in. (north face)	Y = 48-1/4 in. (south face) Y = 48-1/4 in. (north face)
Wall DC LVDT 4	X_7 = 12.5 in. (south face) X_7 = 12.5 in. (north face)	Y = 48-1/4 in. (south face) Y = 48-1/4 in. (north face)
Wall uplift sensor	X_8 = 2 in.	
Horizontal position sensor (top and bottom)	U = 25-1/8 in.	V = 2-1/8 in.
Sensors for specimen 2b (AISC 341-2022)	**Position**	
Tilt meter 1	X_1 = 16-1/4 in.	
Tilt meter 2	X_2 = 1-1/2 in.	
Vertical DC LVDT	X_3 = 2-5/8 in.	
Wall DC LVDT 1	X_4 = 2 in.	Y = 49-3/4 in. (south face) Y = 48-1/4 in. (north face)
Wall DC LVDT 2	X_5 = 5.5 in.	Y = 48-1/4in. (south face) Y = 48-1/4 in. (north face)
Wall DC LVDT 3	X_6 = 9 in.	Y = 48-1/4 in. (south face) Y = 48-1/4 in. (north face)
Wall DC LVDT 4	X_7 = 12.5 in.	Y = 48-1/4 in. (south face) Y = 48-1/4 in. (north face)
Wall uplift sensor	X_8 = 2 in.	
Horizontal position sensor (top and bottom)	U = 24-3/4 in.	V = 2-1/8 in.

Figure 2.18 Locations of external instruments for specimens 2a and 2b (test 3 and test 4).

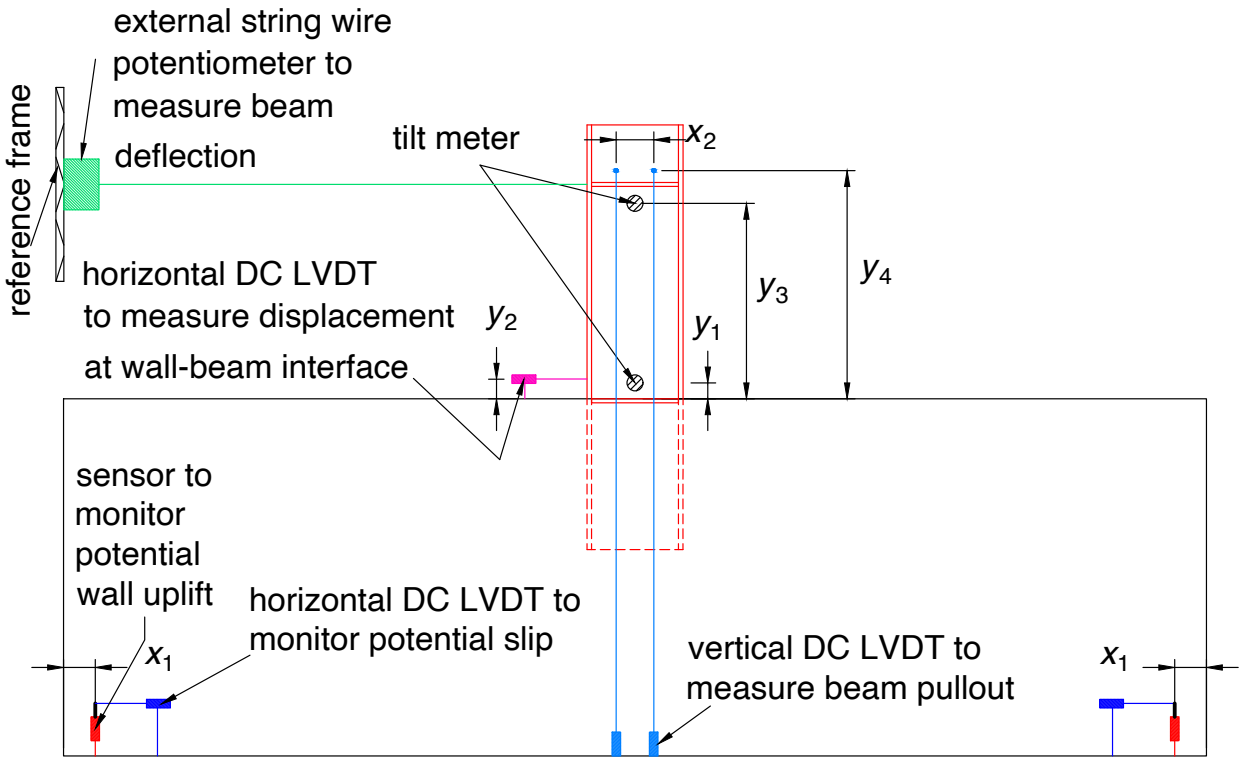

Specimen I.D.	Test I.D.	x_1 (in.)	x_2 (in.)	y_1 (in.)	y_2 (in.)	y_3 (in.)	y_4 (in.)
2	5	4	5-1/2	2	2-5/8	24-5/8	28-1/8
3	6	4	5-1/2	2	2-5/8	24-5/8	28-3/4
4	7	4	5-1/2	2	2-9/16	24-1/2	29
5	8	4	4-3/4	2	2-1/2	24-5/8	28-3/4

Figure 2.19 Locations of external instruments for phase 2 specimens.

2.7 Testing protocol

The loading protocol for specimen 1a (test 1) was different from that for the remaining tests. For test 1, the goal was to subject the connection to: 250 cycles at $0.15M_{pr}$, 500 cycles at $0.40M_{pr}$, 75 cycles at $0.75M_{pr}$, 5 cycles at $1.2\theta_y$, 2 cycles at $1.5\theta_y$, 5 cycles at $1.2\theta_y$, 75 cycles at $0.75M_{pr}$, 500 cycles at $0.40M_{pr}$, and 250 cycles at $0.15M_{pr}$, where M_{pr} is coupling beam probable moment capacity and θ_y is coupling beam yield rotation. However, due to an issue with data acquisition computer, the connection was subjected to 495 cycles at $0.15M_{pr}$ (corresponding to $0.54V_n$ where V_n is the nominal shear force for which the connection was designed) and testing

was terminated after 40 cycles at $0.40M_{pr}$ (equivalent to $1.43V_n$) as the connection had lost its integrity and could not resist additional loads.

Based on the lessons learned from the first test, the loading protocol was changed for the remaining specimens. The goal was to subject each specimen to 543 cycles with increasing and decreasing force amplitudes. If possible, the remaining specimens were to be subjected to a series of load-controlled cycles followed by a "standard" seismic protocol. The intended testing protocol is summarized in Table 2.9. As noted in this table; however, not all the steps/cycles could be completed for some of the specimens due to unanticipated failure, or additional cycles were conducted because an instrument had malfunctioned and had to be replaced.

Table 2.9 Testing protocol.

Wind		Seismic	
Load Step	Description	Displacement Cycle	Description
1	100 cycles @ 0.25V_n	1	3 cycles @ θ[a]= 0.50%
2	100 cycles @ 0.40V_n	2	3 cycles @ θ = 0.75%
3	50 cycles @ 0.50V_n	3	3 cycles @ θ = 1.0%
4	15 cycles @ 0.67V_n	4	3 cycles @ θ = 1.5%
5	5 cycles @ 0.83V_n	5	3 cycles @ θ = 2.0%
6	3 cycles @ V_n	6	3 cycles @ θ = 3.0%
7	5 cycles @ 0.83V_n	7	2 cycles @ θ = 4.0%
8	15 cycles @ 0.67V_n	8	2 cycles @ θ = 6.0%
9	50 cycles @ 0.50V_n	9	1 cycle@ θ = 8.0%
10	100 cycles @ 0.40V_n		
11	100 cycles @ 0.25V_n		

[a] θ = chord rotation

Variations from the target testing protocol:

- Specimen 1b (test 2): 45 additional cycles @ 0.50V_n and 15 additional cycles @ 0.67V_n, 2 cycles @ θ = 1.5%, 1 cycle @ θ = 2.0%, 1 cycle @ θ = 3.0%, 1 cycle @ θ = 4.0%, 1 cycle @ θ = 6.0%, cycle 9 (1 cycle @ θ = 8.0%) could not be completed.
- Specimen 2a (test 3): 1 cycle @ V_n, load steps 7–11 were not conducted, displacement cycles 1 and 2 were not performed, 1 cycle @ θ = 1.5%, displacement cycles 8–9 were not conducted.
- Specimen 2b (test 4): 1 cycle @ V_n, load steps 9-11 were not conducted, displacement cycles 1–3 were not performed, 1 cycle @ θ = 1.5%.
- Specimen 3 (test 5): Only one-half of cycle for load step 6 could be completed. The following protocols were not conducted: load steps 7–11 and displacement cycles 1–2. Due to excessive damage, displacement cycles 8–9 were not performed.
- Specimen 4 (test 6): Only one complete cycle for load step 6 could be completed. Due to excessive damage, loading was stopped during one-half cycle of the second cycle at V_n. Seismic displacement cycles were not conducted.
- Specimen 5 (test 7): The wind loading protocol was completed. Displacement cycles 1–2 were not conducted. Testing of this specimen was stopped after completing displacement cycle 7 because of excessive damage.
- Specimen 6 (test 8): The connection lost its integrity during the first half cycle of loading step 5. Seismic displacement cycles were not conducted.

This page left blank intentionally.

Chapter 3 Test Results and Discussions

3.1 Introduction

The performances of the connections are described through visual observations and synthesis of the measured test data. The results for each test are first presented separately. The influence of different design method and detailing is discussed by evaluating comparable specimens.

3.2 Specimen 1a (test 1)

The applied shear was normalized with respect to the connection nominal shear strength V_n = 10 kips. The relationship between the normalized shear and chord rotation (tip displacement divided by the shear span) is shown in Figure 3.1. Using the actual embedment length, as-built dimensions, and measured concrete strength, the connection capacity was determined to be 11.8 kips. This capacity, referred to as "provided", was used to normalize the applied shear shown on the secondary y-axis.

Through the first 495 cycles at $0.54V_n$, the chord rotation became progressively larger indicating gradual loss of stiffness. No damage was detected during or at the conclusion of these cycles. The research team (RT) hypothesizes this behavior is because of small, localized deterioration of the bearing of the steel coupling flanges against the surrounding concrete over the embedment length; such damage is not visible on the wall surface. The stiffness was noticeably reduced after the first excursion beyond V_n (i.e., when the normalized shear strength on the primary y-axis is 1). When subjected to 40 cycles of loading at $1.43V_n$, the connection stiffness significantly deteriorated leading to major pinching of the hysteretic response. The results from the last 10 cycles of $1.43V_n$ are not included in Figure 3.1 because the target force could not be reached due to excessive damage.

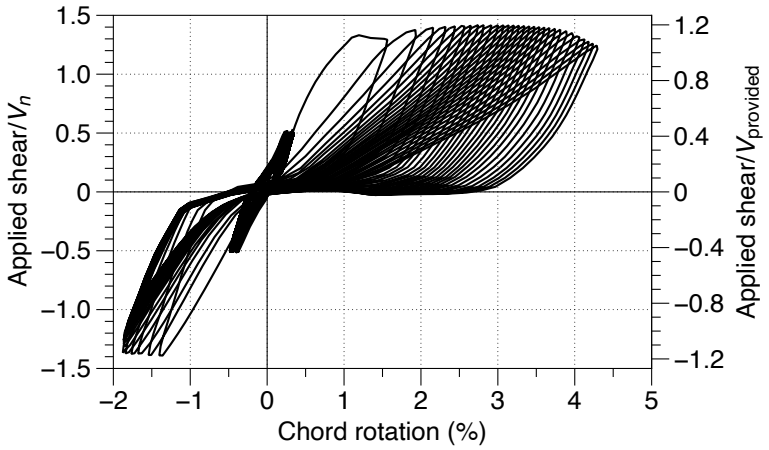

Figure 3.1 Normalized applied shear vs. chord rotation – specimen 1a (test 1).

The coupling beam did not yield, the largest measured flange strain (excluding the last 10 cycles at $1.43V_n$) was 815 micro strains, which corresponds to 24 ksi. Considering that the beam remained elastic, the relationship between the applied shear and deflection is expected to remain elastic. Hence, the nonlinearity seen in Figure 3.1 is attributed to damage in the connection region. The connection flexibility is also evident from Figure 3.2. The coupling beam displacement at 1-7/8 in. from the face reached a maximum value of nearly 0.15 in., which is nearly 0.19 times the maximum tip deflection and significantly larger than the expected value had the coupling beam been fixed at the face of the wall.

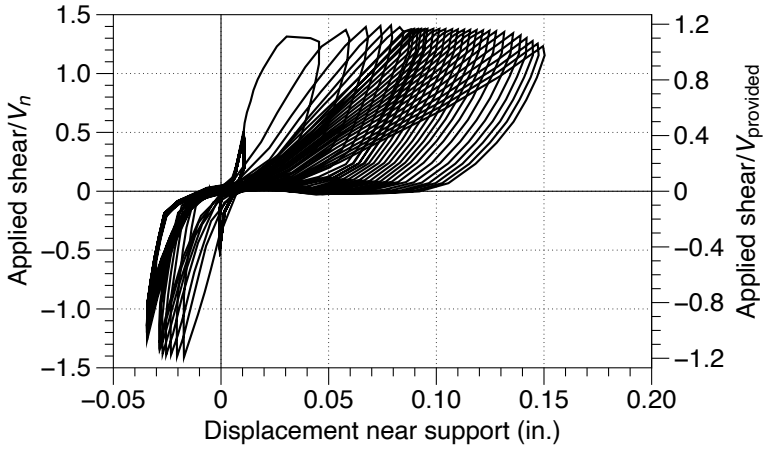

Figure 3.2 Normalized applied shear vs. displacement near support – specimen 1a (test 1).

The photograph in Figure 3.3 illustrates the level of damage at the conclusion of loading. After 5 cycles at $1.43V_n$, a major crack was found between the flanges. The concrete within the flanges was completely lost on one side. The damage penetrated 3 in., i.e., one-half of the total provided embedment length, into the wall. The damage shown in the photograph corroborates the loss of stiffness and pinching behavior observed in Figure 3.1.

Figure 3.3 State of connection at the conclusion of testing – specimen 1a (test 1).

3.3 Specimen 1b (test 2)

The applied shear was normalized with respect to the connection nominal shear strength V_n = 10 kips. The relationship between the normalized shear and chord rotation is shown in Figure 3.4. Using the actual embedment length, as-built dimensions, and measured concrete strength, the connection capacity was determined to be 15.5 kips. This capacity, referred to as "provided", was used to normalize the applied shear shown on the secondary y-axis. The wind loading protocol consisted of 543 cycles with 3 cycles at V_n. As evident from the inset in Figure 3.4, the connection response during wind load protocol was nonlinear with some pinching. Visual inspection did not, however, indicate any cracking around the connection. The nonlinearity is attributed to the localized bearing failure of concrete around the flanges in the

embedded region. The level of nonlinearity increased during seismic tests. Prior to failure, the connection was subjected to several cycles of shears that exceeded the nominal and "provided" capacities. The connection suddenly lost its load carrying capacity during the negative half of the first cycle at 6% chord rotation as indicated in Figure 3.4. The failure occurred after reaching $2.03V_n$ (1.32 times the "provided" connection capacity) at 4.74% chord rotation.

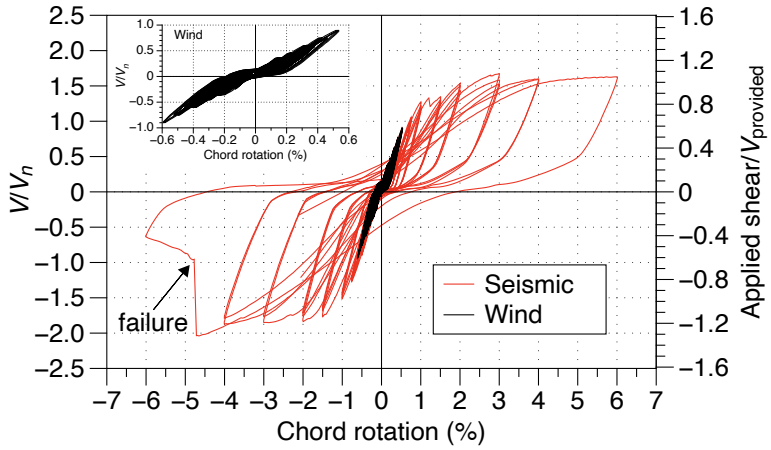

Figure 3.4 Normalized applied shear vs. chord rotation – specimen 1b (test 2).

Similar to specimen 1a (test 1), the coupling beam remained elastic during both the wind and seismic test protocols. The maximum flange strain indicates a maximum stress of $0.66F_y$, where F_y is the measured flange yield strength. Considering that the beam remained elastic, the observed nonlinearities are due to the damage in the connection region, which is also evident from the displacement measured at 1-7/8 in. from the face of the support, see Figure 3.5. During wind load tests, the maximum displacement near the support, which is expected to be small, was 0.10 times the peak tip deflection. For the seismic cycle at 6%, the ratio between maximum displacement near support and tip deflection was 0.22.

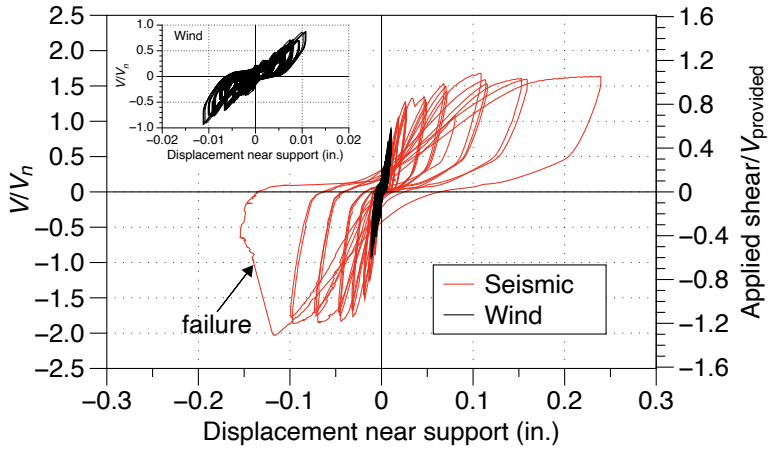

Figure 3.5 Normalized applied shear vs. displacement near support – specimen 1b (test 2).

The damage after completing the wind protocol load cycle and subjecting the connection to a series of chord rotations reaching a maximum value of 6% is shown in Figure 3.6. The loss of load-carrying capacity is primarily attributed to crushing above the top flange and between the flanges.

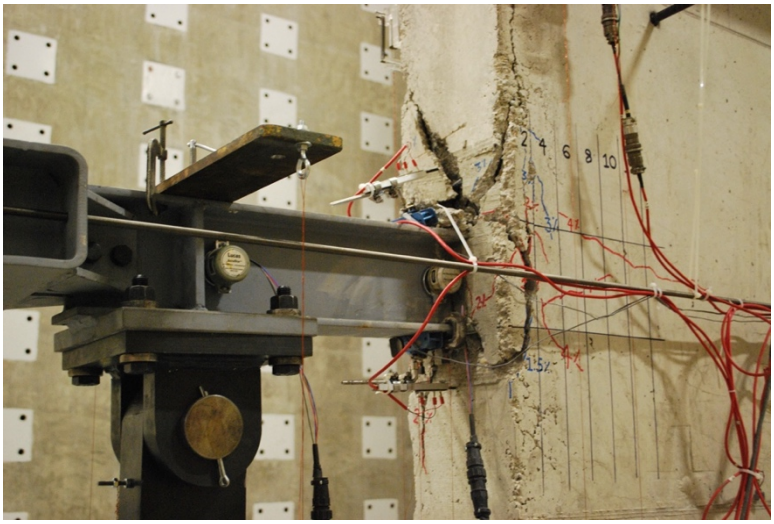

Figure 3.6 State of connection at the conclusion of testing – specimen 1b (test 2).

3.4 Specimen 2a (test 3)

The applied shear was normalized with respect to V_n (49.4 kips) and the "provided" connection capacity (56.0 kips) that was calculated using the measured material strengths and as-built dimensions. The normalized applied shear versus the chord rotation is plotted in Figure 3.7.

The connection lost significant stiffness during the first cycle of wind load step 6 (i.e., 3 cycles at V_n). For instance, the chord rotation was increased by a factor of 4.1 when the shear was increased from $0.83V_n$ to $0.95V_n$ (from 0.73 to 0.84 times the "provided" capacity). The condition of the specimen after unloading and removal of loose concrete is documented in Figure 3.8. It should be noted that prior to this stage of loading, the specimen had been subjected to a total of 270 cycles with increasing load amplitudes less than V_n (100 cycles @ $0.25V_n$, 100 cycles @ $0.40V_n$, 50 cycles @ $0.50V_n$, 15 cycles @ $0.50V_n$, and 5 cycles @ $0.83V_n$). Considering the significant loss of connection integrity, the remaining wind load steps (see Table 2.9) were not conduced. Deterioration of connection integrity is evident from the seismic tests: the load resisted by the connection was at most $0.77V_n$ and $0.96V_n$ for the positive and negative half cycles, respectively, even though the connection was subjected to 6% chord rotation.

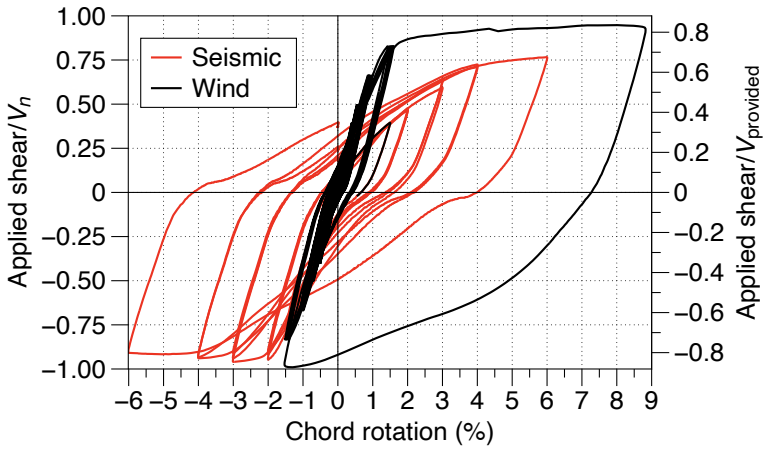

Figure 3.7 Normalized applied shear vs. chord rotation – specimen 2a (test 3).

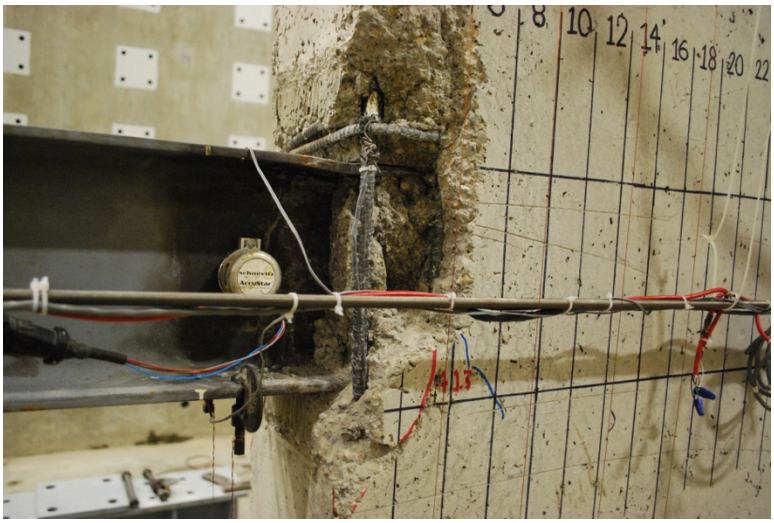

Figure 3.8 Condition of connection at the conclusion of wind load protocol tests – specimen 2a (test 3).

A still image captured from video recordings (Figure 3.9) suggests the formation of a "plastic hinge" in the coupling beam. The "plastic hinge" is attributed to excessive yielding, local flange bending, and web buckling. Flange yielding is seen from Figure 3.10. At $0.93V_n$, the bottom flange yielded. The strain in the top flange began to change sign, which is attributed to local flange bending, at $0.94V_n$. The maximum strain in the top and bottom flange was $2.83\varepsilon_y$ (ε_y = yield strain) and $1.65\varepsilon_y$, respectively. The residual bottom flange strain was nearly twice the yield strain. Flange bending and web buckling can be seen in the photographs shown in Figure 3.11.

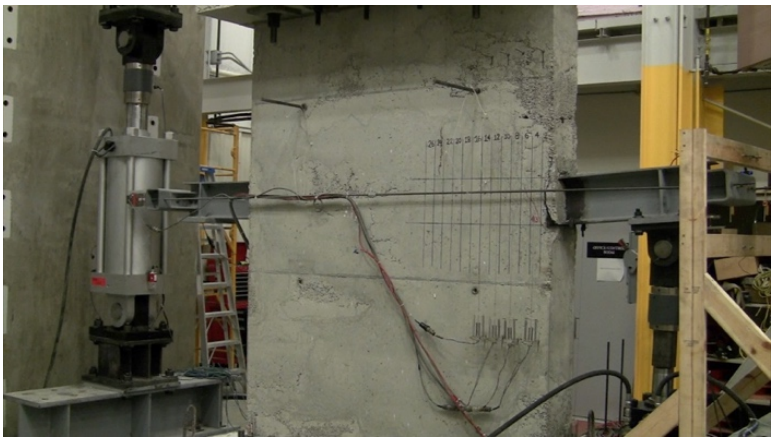

Figure 3.9 Deformation at peak chord rotation = 8.76% – specimen 2a (test 3)

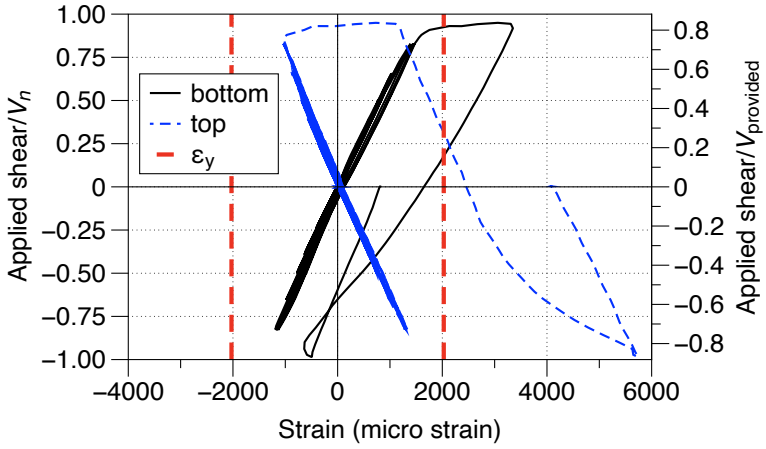

Figure 3.10 Normalized applied shear vs. beam flange strains – specimen 2a (test 3) during wind loading protocol.

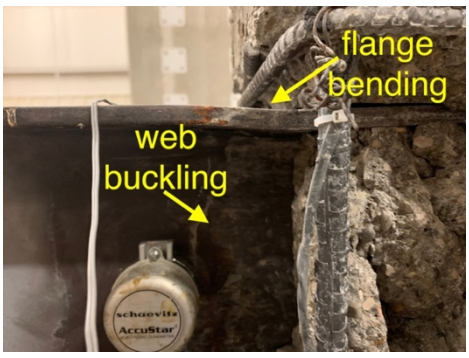

(a) After one cycle at V_n

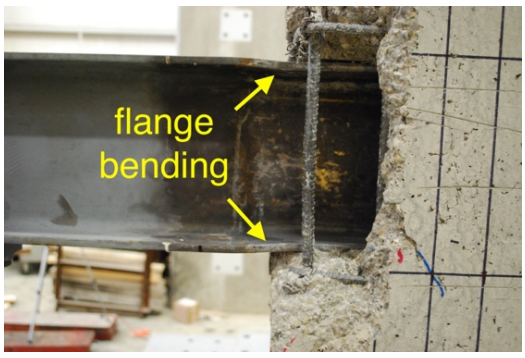

(b) At the completing seismic cycles

Figure 3.11 Flange bending and web buckling – specimen 2a (test 3).

The relationship between the normalized applied shear and beam displacement at 2 in. from the face of the wall is shown in Figure 3.12. Prior to the sudden loss of stiffness, the beam

displacement at this location was nearly 0.05 in., which corresponds to 17% of the maximum tip displacement. The hysteretic loops up to the sudden increase and relatively large displacement near the wall suggest connection flexibility. The same trend was observed for specimen 1b (test 2).

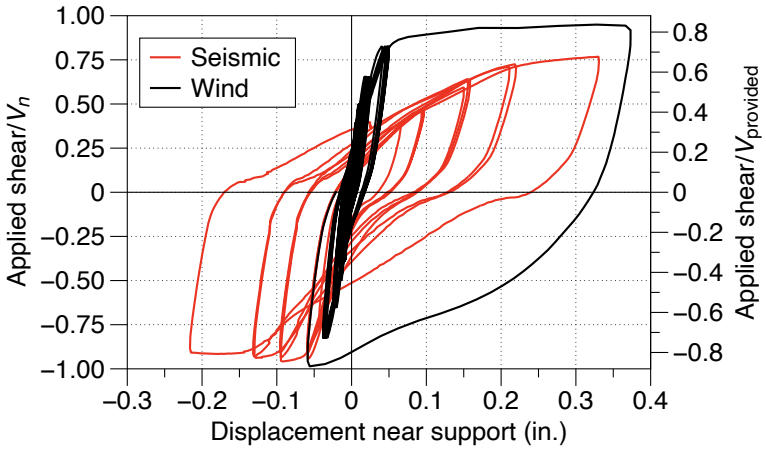

Figure 3.12 Normalized applied shear vs. displacement near support – specimen 2a (test 3).

As evident from Figure 3.13, the coupling beam was progressively being "pulled out" of the wall leading to an increase in the axial restraint apparatus's force. This trend is consistent with the results discussed previously. The permanent axial deformation and corresponding force were 0.25 in. and 6.1 kips at the conclusion of the first 270 cycles.

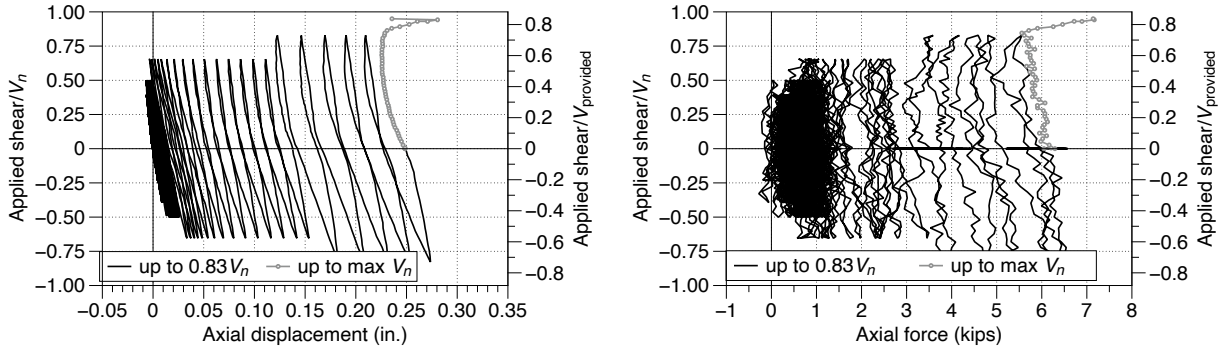

(a) Axial displacement (b) Axial force

Figure 3.13 Normalized applied shear vs. coupling beam axial displacement and axial force during wind load protocol tests – specimen 2a (test 3).

The excessive loss of stiffness correlates with the condition of the connection at the conclusion of wind load protocol testing, see Figure 3.14. The steel coupling beam flange was found to have bent, and the web had buckled (Figure 3.15). Damage had penetrated the wall between 5 in. and 6 in., reducing the available embedment length to approximately 0.58 times the original length (13 in.). After subjecting the connection to the post-wind seismic displacement protocol (see Table 2.9), the connection experienced further damage. The available embedment length had been reduced to between 4.5 in. and 6 in., i.e., a loss of more than 50%. Furthermore, the flange experienced more bending, web buckling became more pronounced, and the wall longitudinal bar buckled. These damages are shown in Figure 3.15.

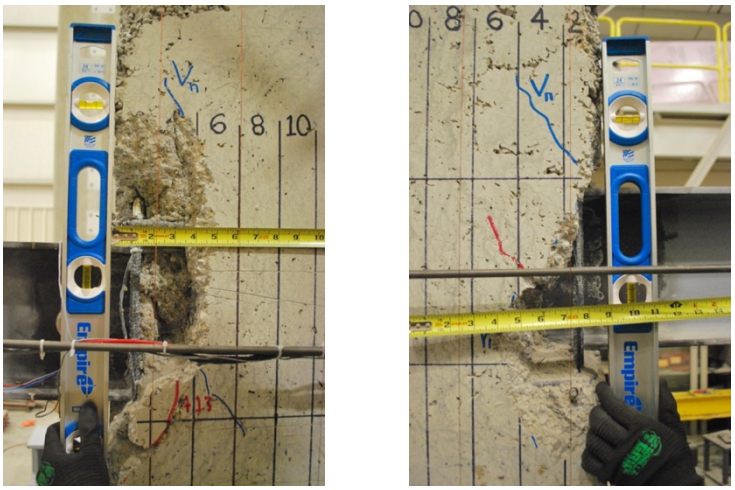

(a) South face (b) North face

Figure 3.14 Damage at the conclusion of wind load protocol testing and after removing loose concrete – specimen 2a (test 3).

(a) Flange bending and extent of damage

(b) Buckling of web and wall longitudinal reinforcement

Figure 3.15 Damage at the conclusion of seismic load protocol testing and after removing loose concrete – specimen 2a (test 3).

3.5 Specimen 2b (test 4)

The difference between this specimen and specimen 2a was the additional longitudinal reinforcement along the embedment length. Despite having more reinforcement, the performance of specimen 2b (test 4) was rather similar to specimen 2a (test 3). The connection lost a significant amount of stiffness during the first cycle at V_n (see Figure 3.16), which was also observed for specimen 2a (Figure 3.7). The sudden loss of stiffness is apparent by, for example, comparing the chord rotation of 1.43% at $0.83V_n$ versus 5.36% at $0.96V_n$, which was the largest shear that the connection could resist. The chord rotation was increased by a factor of nearly 4 when the applied shear was increased by $0.13V_n$ (6.43 kips).

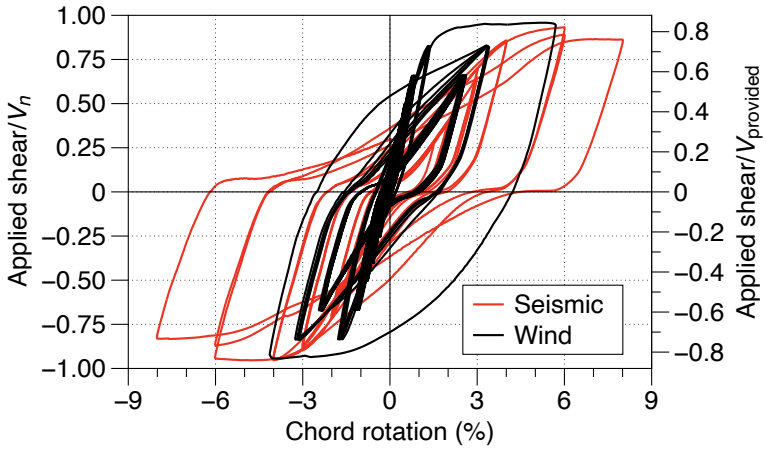

Figure 3.16 Normalized applied shear vs. chord rotation – specimen 2b (test 4).

The effect of the sudden loss of stiffness is also evident from Figure 3.17, which shows the relationship between the normalized applied shear and the beam displacement measured at 2-5/8 in. from the wall. The hysteresis loops prior to the rapid increase in the displacement point to the connection flexibility.

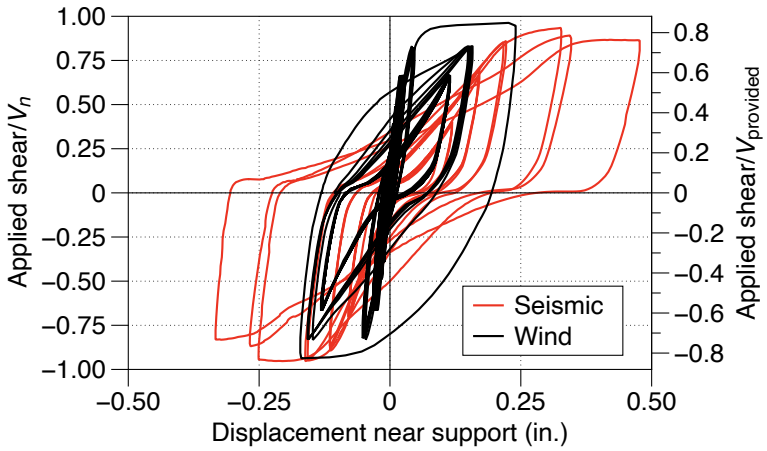

Figure 3.17 Normalized applied shear vs. displacement near support – specimen 2b (test 4).

The trends of the strains in the coupling beam top and bottom flanges are like those in specimen 2a (Figure 3.18). During the last cycle of wind-load protocol, which was aimed at subjecting the connection to V_n, the bottom flange yielded at an applied shear equal to $0.96V_n$. At nearly the same load, the sign of top flange strain began to reverse (from being in compression to

becoming positive), which suggests flange bending. Prior to load reversal, i.e., at peak chord rotation of 5.70%, the bottom flange strain was $1.24\varepsilon_y$ (ε_y = yield strain). The residual stress on the bottom flange was nearly equal to the yield stress. Although compression strain was expected in the top flange, flange bending resulted in a tensile strain equal to $0.34\varepsilon_y$.

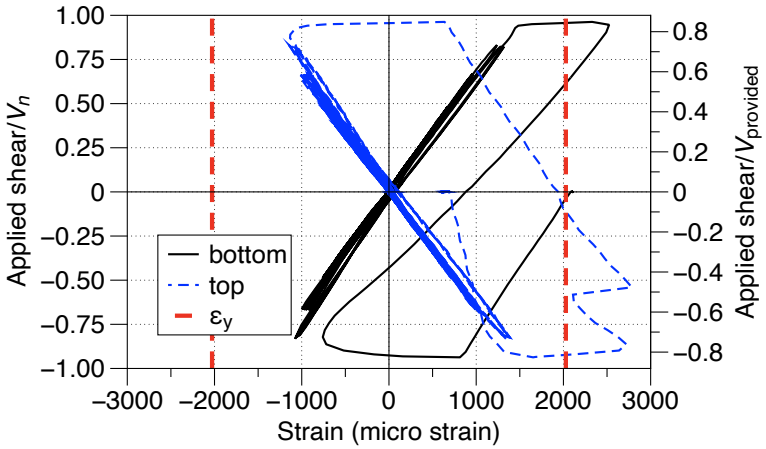

Figure 3.18 Normalized applied shear vs. beam flange strains – specimen 2b (test 4) during wind loading protocol.

The coupling beam in this specimen was also progressively "pulled out" of the wall as the level of the applied shear was increased, see Figure 3.19. Prior to attempting to subject the connection to V_n, the coupling beam had been "pulled out" 0.30 in. The corresponding force in the axial restraint apparatus was 7.2 kips.

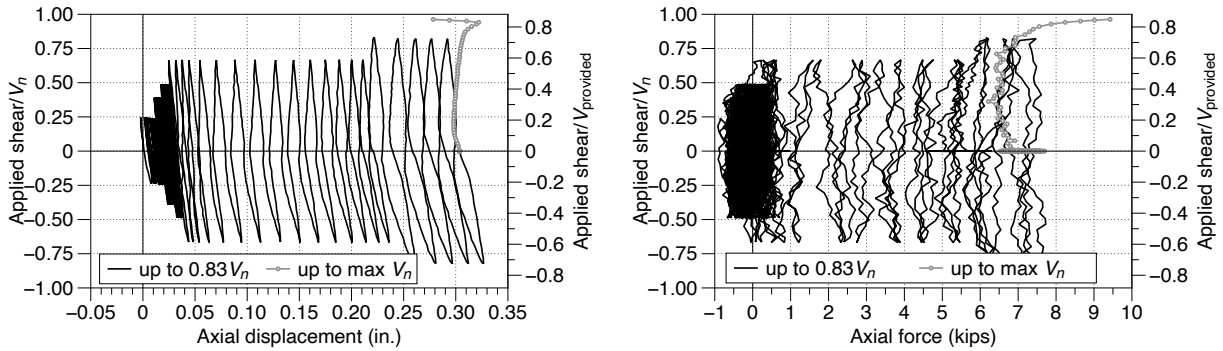

(a) Axial displacement (b) Axial force

Figure 3.19 Normalized applied shear vs. coupling beam axial displacement and axial force during wind load protocol tests – specimen 2b (test 4).

At the conclusion of the wind load protocol, the wall above and below the beam had been damaged extensively. The extensive level of damage had reduced the available embedment length to between 9 in. and 11 in., i.e., between 15% and 31% of the embedment length had been lost. The smaller embedment reduces the connection stiffness, which is consistent with a sudden increase of chord rotation observed in Figure 3.16. The level of damage was, expectedly, increased with additional applications of wind load protocol (5 cycles at $0.83V_n$ and 15 cycles at $0.67V_n$) and seismic protocol (see Table 2.9). At the conclusion of the tests, between 5 in. and 7.5 in. of embedment length had been lost (0.39 and 0.58 times the embedment length). Moreover, both the top and bottom flanges were bent, and the web clearly had buckled. The condition of specimen 2b at the conclusion of the testing program is illustrated in Figure 3.21.

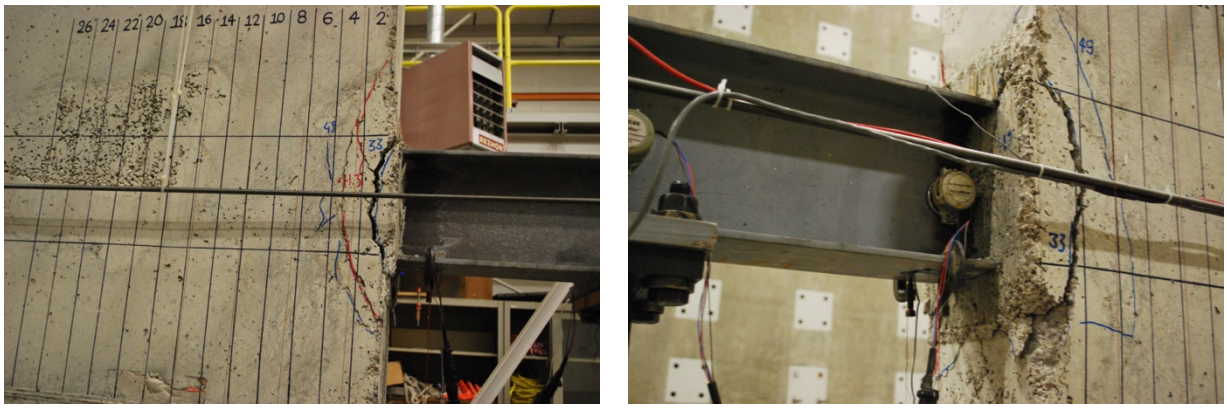

(a) North face (b) South face

Figure 3.20 Damage at the conclusion of wind load protocol testing (loose concrete was not removed) – specimen 2b (test 4).

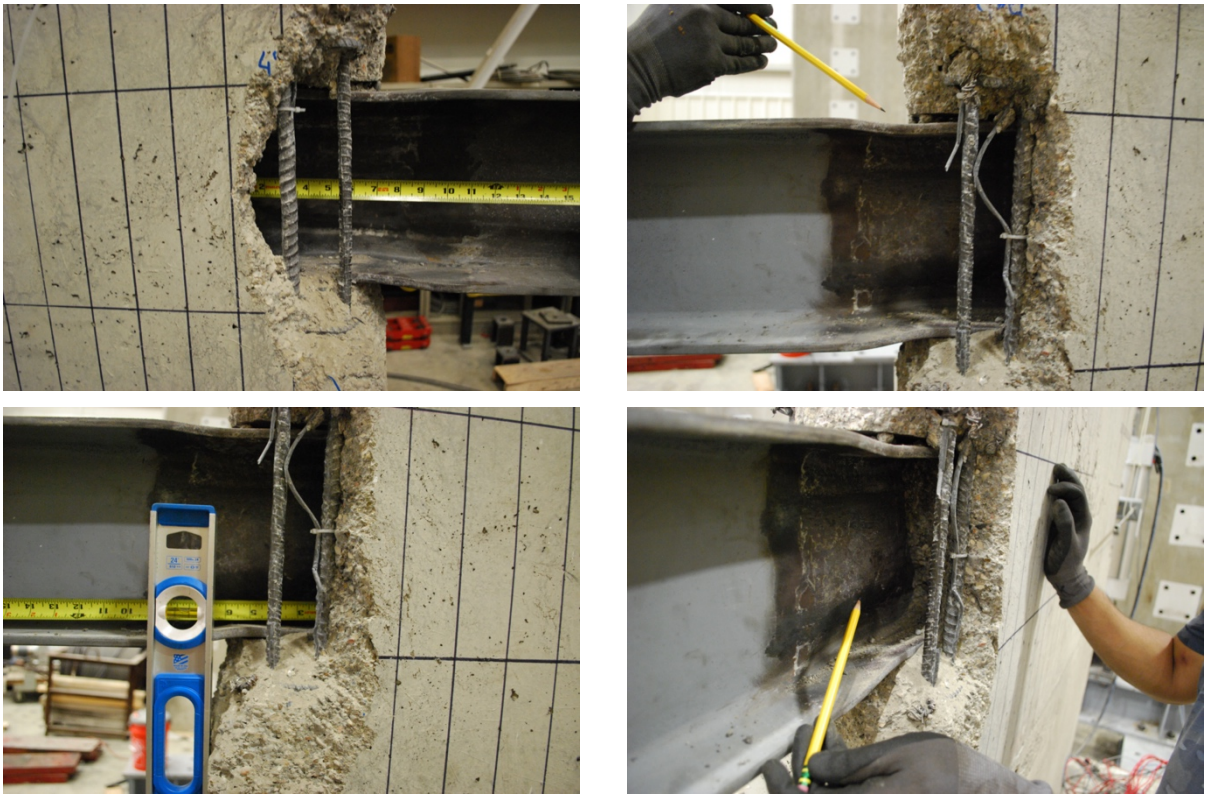

(a) Penetration of damage into wall (b) Flange bending and web buckling

Figure 3.21 Damage at the conclusion of seismic load protocol testing and after removing loose concrete – specimen 2b (test 4).

3.6 Specimen 3 (test 5)

The applied shear was normalized with respect to the target value of V_n = 113 kips. The relationship between the normalized shear chord rotation is shown in Figure 3.22. Using the

actual embedment length, as-built dimensions, and measured concrete strength, the "provided" connection capacity is 122 kips. This capacity was used to normalize the applied shear shown on the secondary y-axis. During the first cycle of step 6 (3 cycles at V_n), the connection suddenly lost stiffness after reaching $0.96V_n$. As a result, the tip deflection abruptly jumped to 1.03 in. (corresponding to 3.8% chord rotation), exceeding the safety displacement limit set in the controller, and loading was stopped. The photographs in Figure 3.23 show the status of the connection at this stage. The excessive permanent deformation of the beam is evident from Figure 3.23(b). As intended, the face bearing plates prevent local bending and buckling of the flanges and web.

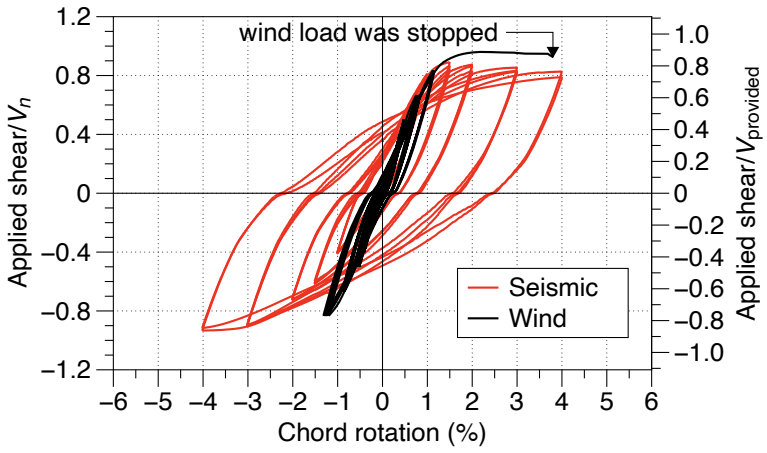

Figure 3.22 Normalized applied shear vs. chord rotation – specimen 3 (test 5).

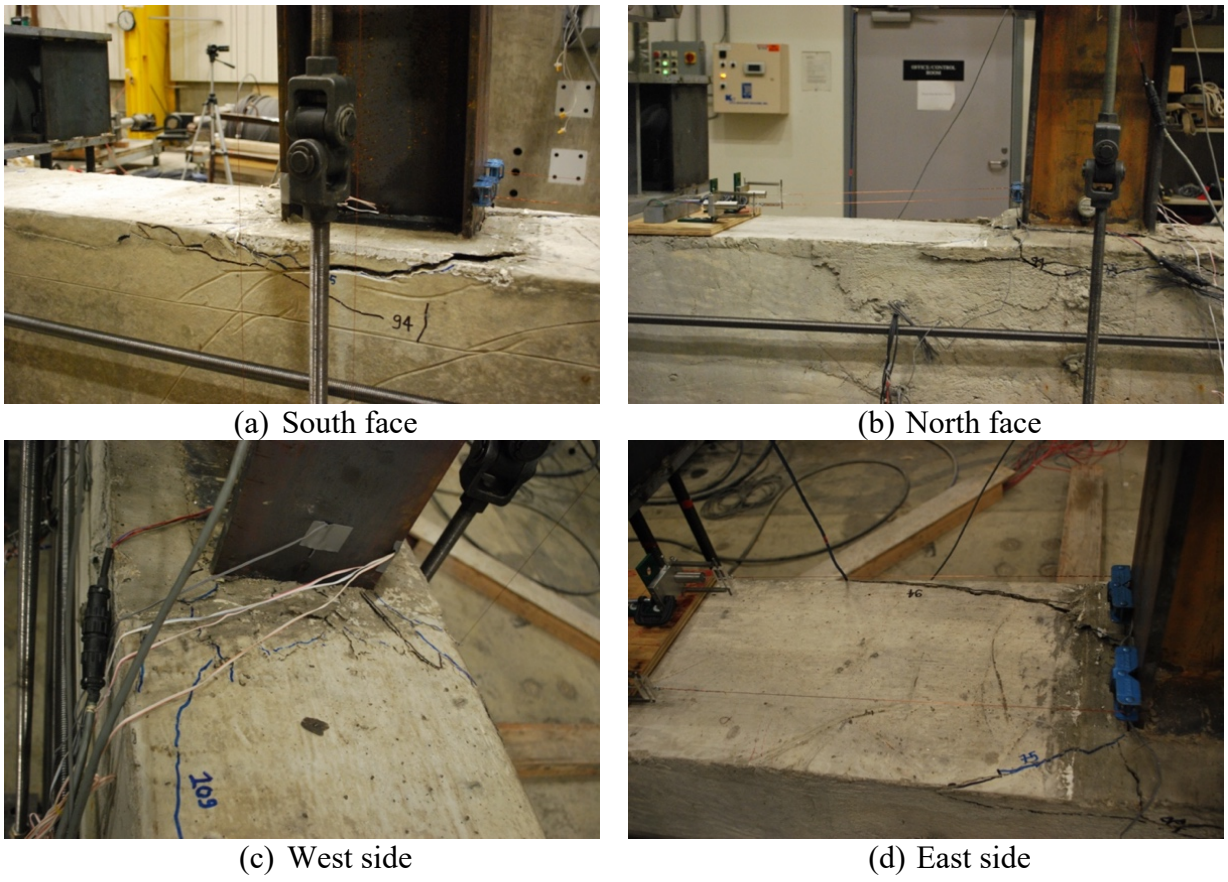

(a) South face (b) North face

(c) West side (d) East side

Figure 3.23 Damage at 0.96V_n for specimen 3 (test 5).

Although the specimen had failed before reaching V_n, the connection was subjected to the seismic protocol shown in Table 2.9 in an attempt to get data regarding post-damage behavior. The influence of damage is easily seen in the curves for the seismic segment. The maximum shear that could be resisted during seismic cycles was 0.89V_n. Considering the significant level of damage at the end of the wind load protocol and the performance during 3 cycles at 1.5%, 2%, and 3% chord rotation, loading was stopped after completing 2 cycles at 4% chord rotation.

The connection flexibility can be seen from Figure 3.24, which shows the coupling beam displacement at 2-5/8 in. from the face of the wall. Prior to failure, reflected by the sudden jump, the peak displacement near the support was nearly 0.14 times the peak deflection at the load point. At the conclusion of wind load protocol tests, the flanges did not yield (Figure 3.25); the

maximum strain was $0.88\varepsilon_y$, where ε_y is the yield strain. Figure 3.27 shows the shear stress (V/dt_w) vs. maximum shear strain determined from a rosette strain gage bonded to the web at the coupling beam's mid-depth – see Figure 3.26 for the relevant formulae. The shear strain at yield ($\gamma_y = \left(F_y/\sqrt{3}\right)/G$ with G taken as $0.39E$ by assuming the Poisson ratio is 0.27) is also plotted in Figure 3.27. A sudden increase in shear strain is observed when the applied shear reached $0.89V_n$; however, the largest maximum shear strain did not exceed γ_y– it was $0.98\gamma_y$. Therefore, the sudden loss of stiffness leading to a jump in the displacements at the tip or near the support is primarily attributed to the loss of connection integrity. When subjected to seismic protocol, both the flange and web yielded. Although the level of yielding was more significant for the web, the maximum flange strain was $1.07\varepsilon_y$ and the maximum shear strain in the web at the coupling beam's mid-depth reached a value of nearly $2\gamma_y$.

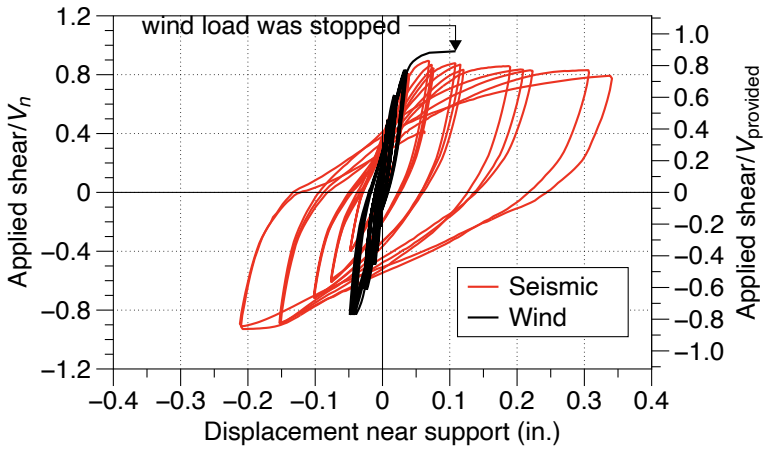

Figure 3.24 Normalized applied shear vs. displacement near support – specimen 3 (test 5).

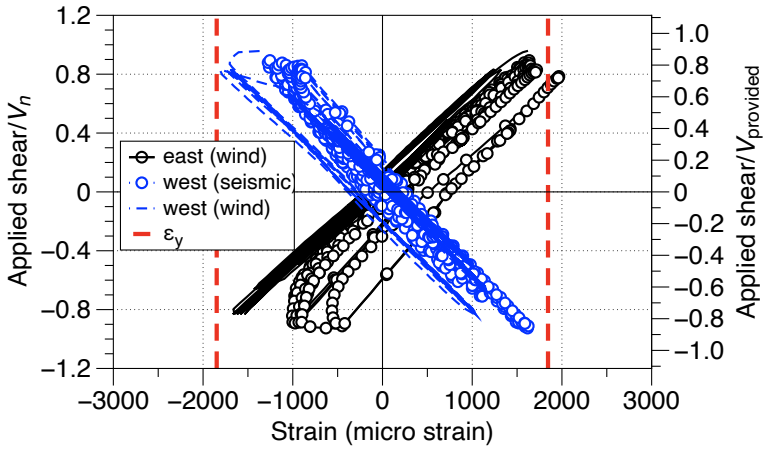

Figure 3.25 Normalized applied shear vs. beam flange strains – specimen 3 (test 5).

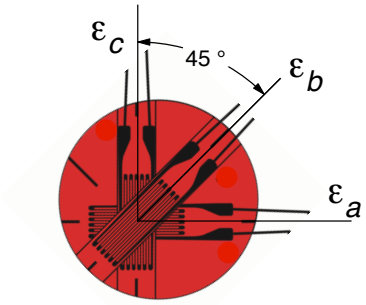

image modified from https://tml.jp/e

maximum and minimum principal strains:

$$\varepsilon_{max} = 0.5\left\{\varepsilon_a + \varepsilon_c + \sqrt{2[(\varepsilon_a - \varepsilon_b)^2 + (\varepsilon_b - \varepsilon_c)^2]}\right\}$$

$$\varepsilon_{min} = 0.5\left\{\varepsilon_a + \varepsilon_c - \sqrt{2[(\varepsilon_a - \varepsilon_b)^2 + (\varepsilon_b - \varepsilon_c)^2]}\right\}$$

maximum shear strain:

$$\gamma_{max} = \sqrt{2[(\varepsilon_a - \varepsilon_b)^2 + (\varepsilon_b - \varepsilon_c)^2]}$$

Figure 3.26 Calculation of peak normal and shear strains from rosette strain gage data.

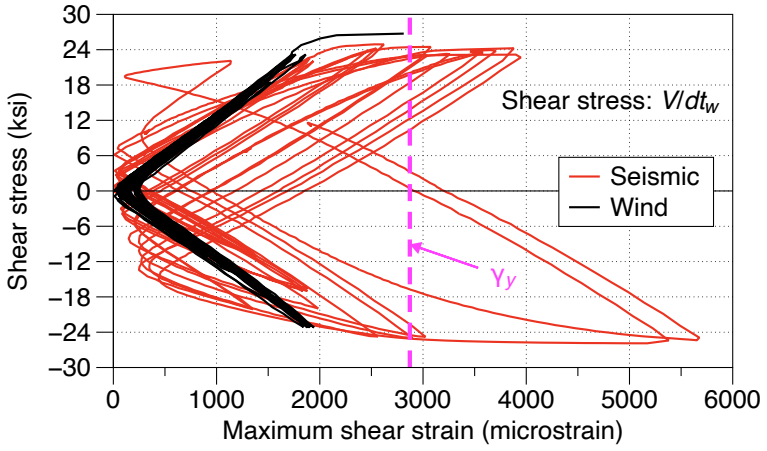

Figure 3.27 Shear stress vs. maximum shear strain – specimen 3 (test 5).

The coupling beam in this specimen was also progressively "pulled out" of the wall as the level of applied shear was increased, see Figure 3.28. At the end of wind load protocol

testing, the connection had been moved axially by 0.17 in. (0.0063 times the original shear span of 27 in.) with a corresponding force of 15.8 kips (0.15 times the maximum applied shear) in the axial restraint apparatus.

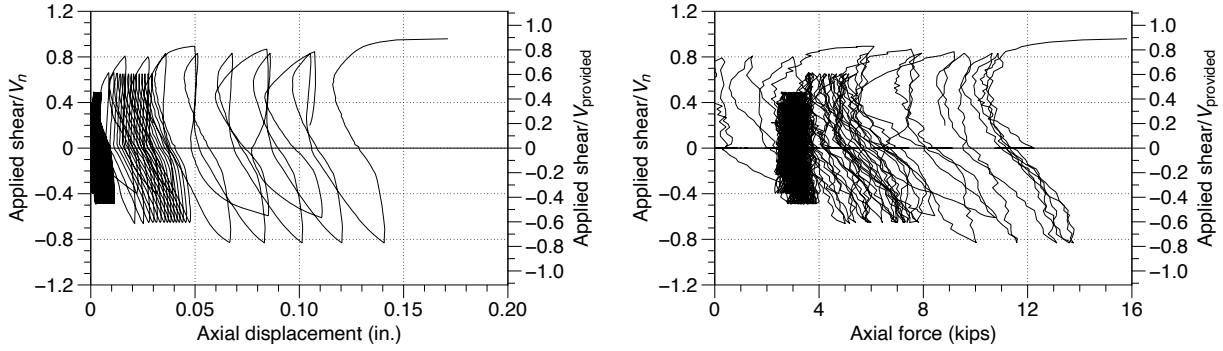

(a) Axial displacement (b) Axial force

Figure 3.28 Normalized applied shear vs. coupling beam axial displacement and axial force during wind load protocol tests – specimen 3 (test 5).

The connection had been damaged significantly at the conclusion of the seismic loading protocol, see Figure 3.29. Out of the total embedment length of 19 in., 7 and 9.5 in. of concrete between the flanges had been damaged significantly on the South and North face, respectively (Figure 3.29c). Over a depth ranging between 4 and 8.5 in., there was a gap between the flange and wall, suggesting bearing failure (Figure 3.29d). At the conclusion of loading, no evidence of local bending and buckling of the flanges and web was found; the face bearing plates performed at expected.

(a) South face

(b) North face

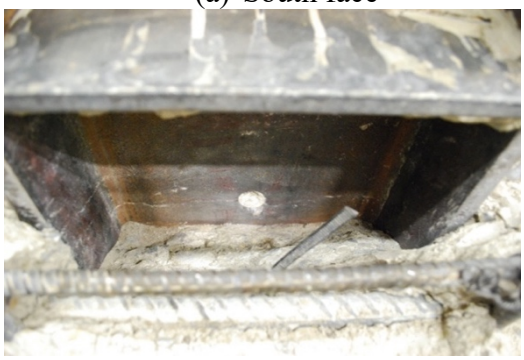

(c) Damage penetration

(d) Gap opening between flange and wall

Figure 3.29 Damage at the conclusion of seismic load protocol testing and after removing loose concrete – specimen 3 (test 5).

3.7 Specimen 4 (test 6)

The embedment length was 24 in. compared to 19 in. for specimen 3 (test 5). In contrast to specimen 3, one cycle at V_n could be applied, but the connection failed after reaching $0.99V_n$ during the application of the second cycle at 5.7% chord rotation. The connection had experienced significant damage during the first cycle at V_n as evident from the normalized applied shear force versus chord rotation shown in Figure 3.30. The positive chord rotation increased substantially with little increase in shear. This connection was not subjected to seismic protocol considering the large chord rotation at which it failed. Similar sudden increases are observed in the displacement at 2-5/8 in. from the wall (Figure 3.31), axial displacement (Figure 3.32a), and axial force in the axial restraint apparatus (Figure 3.32b). Due to delays in placing

concrete in this specimen, water had to be added onsite to the concrete mix. The unexpected bad performance of this specimen is attributed to the concrete quality.

During the first cycle at V_n, the flange on the west side yielded (see Figure 3.33): the maximum strain $1.24\varepsilon_y$ (ε_y = yield strain based on the measured yield strength) with a residual strain (after completing the first cycle at V_n) of $0.33\varepsilon_y$. At the conclusion of loading, the residual strain in the west flange was $0.94\varepsilon_y$. The east flange remained elastic except during the last cycle before failure (i.e., the attempt to conduct the second cycle at V_n) when it marginally yielded: the maximum strain was $1.02\varepsilon_y$. The residual strain in the east flange was $0.084\varepsilon_y$ at the conclusion of loading.

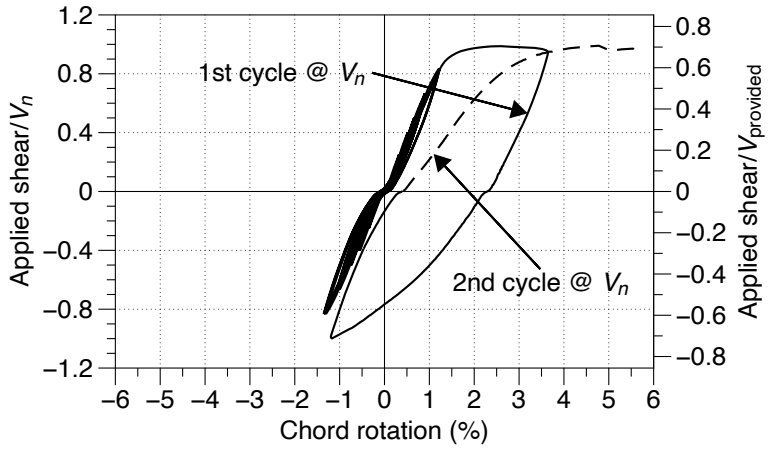

Figure 3.30 Normalized applied shear vs. chord rotation – specimen 4 (test 6).

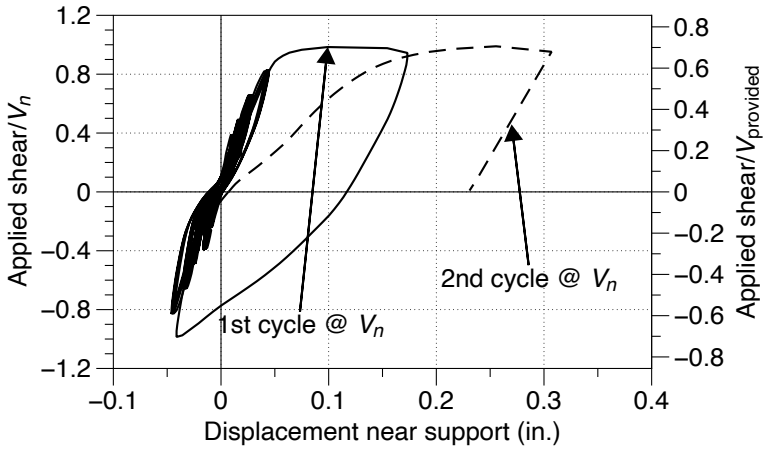

Figure 3.31 Normalized applied shear vs. displacement near support – specimen 4 (test 6).

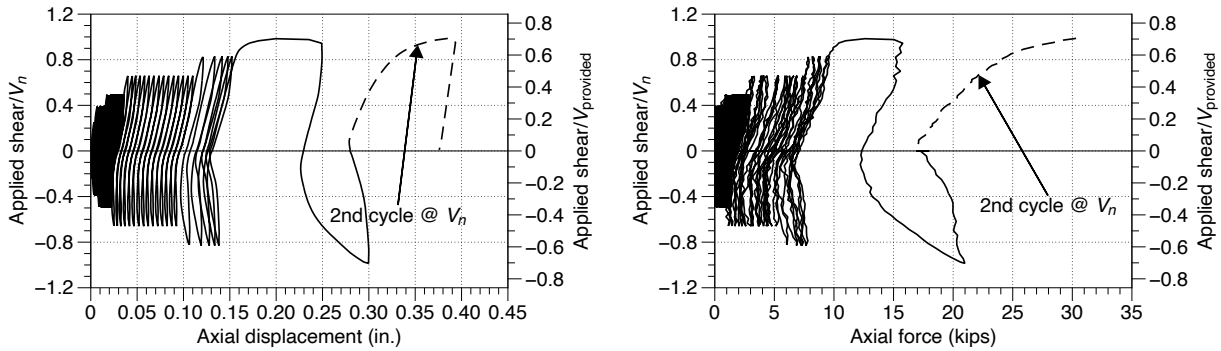

(a) Axial displacement (b) Axial force

Figure 3.32 Normalized applied shear vs. coupling beam axial displacement and axial force – specimen 4 (test 6).

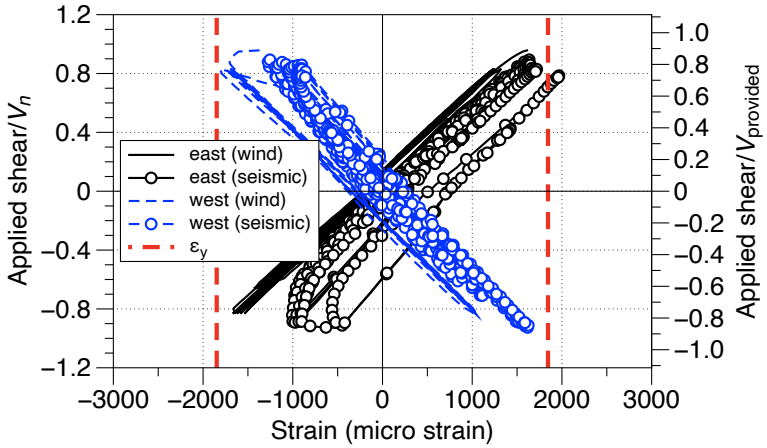

Figure 3.33 Normalized applied shear vs. beam flange strains – specimen 4 (test 6).

During the first 265 cycles (100 cycles @ $0.25V_n$, 100 cycles @ $0.40V_n$, 50 cycles @ $0.50V_n$, and 15 cycles @ $0.67V_n$), the relationship between shear stress and maximum shear strain (determined from the data measured by a rosette strain gage placed on the web at the mid-depth) does not depict any sudden increase (Figure 3.34). However, the maximum shear strain increased suddenly and exceeded γ_y during the first 2 cycles at $0.83V_n$; it reached a value of $1.09\gamma_y$. When subjected to 3 additional cycles at $0.83V_n$, the maximum shear strain did not increase noticeably (it was increased by 128 microstrains to $1.13\gamma_y$). The maximum shear strain more than doubled after the connection underwent one cycle at V_n: the maximum shear strain was $2.53\gamma_y$, i.e., 2.24 times larger than the value for the previous cycles. Before failure, the maximum shear strain was $3.01\gamma_y$, which is 1.19 times larger than the value measured during the first cycle at V_n. The sudden jumps of chord rotation and displacement near the support are not attributed to the extent of yielding of the web but primarily due to the damage in the connection region. This assessment is supported by examining the performance of specimen 5 (test 7) discussed in Section 3.8.

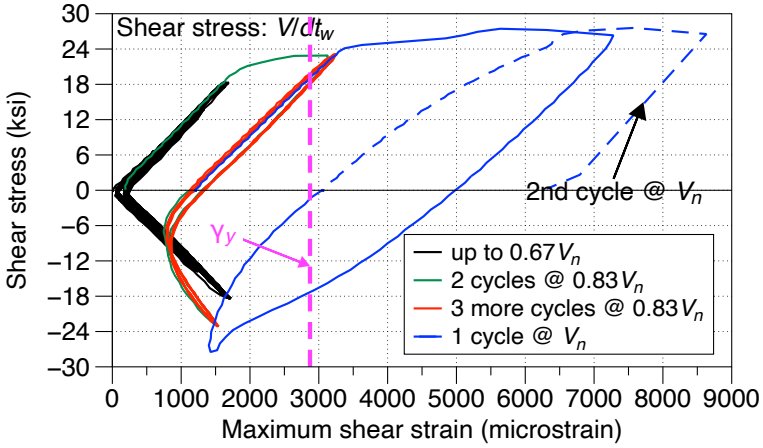

Figure 3.34 Shear stress vs. maximum shear strain – specimen 4 (test 6).

The level of damage, shown in Figure 3.35, is less than that observed in specimen 3 (test 5). In contrast to specimen 3, distributed cracks were found in the wall. Moreover,

approximately 3 in. of loose/crushed concrete between the flanges could be removed, and the maximum depth of gap between the flange and wall was 3-3/8 in. The longer embedment length reduced the level of damage, but this specimen could resist only one cycle of V_n, whereas specimen 3 failed during the first attempt at applying V_n. Similar to specimen 4 (test 6), the face bearing plates prevented flange and web local bending and buckling.

(a) South face

(b) North face

(c) Damage penetration

Figure 3.35 Damage in specimen 4 (test 6) after removing loose concrete.

3.8 Specimen 5 (test 7)

In contrast to specimens 3 and 4 (tests 5 and 6), the entire wind loading protocol could be completed for this specimen that had auxiliary transfer bars. The specimen could develop its target V_n with a maximum chord rotation of nearly 1.6%. Due to localized damages in the connection region during wind loading, the specimen could resist only $0.91V_n$ when subjected to the seismic protocol. At the maximum applied chord rotation of 4%, the load-carrying capacity

was between 0.82V_n and -0.86V_n. The benefits of auxiliary transfer bars are evident from the coupling displacement measured at 2-9/16 in. from the face of the wall (Figure 3.37), axial displacement of the coupling beam (Figure 3.38a), and force in the axial restraint apparatus (Figure 3.38b). For specimen 4 (test 6), which could only resist one cycle at V_n, the displacement near the support, axial displacement, and the axial restraint apparatus force were 2.9, 6.0, and 5.9 times their counterparts in specimen 5 (test 7), respectively. The lower values suggest the benefits of using auxiliary transfer bars in specimen 5. These bars are attached to the flange and provide a direct transfer of forces into the concrete rather than just relying on bearing stresses. The connection integrity was gradually lost during seismic tests as evident from higher values of displacement near the face of the wall, axial deformation of the coupling beam, and force in the axial restraint apparatus.

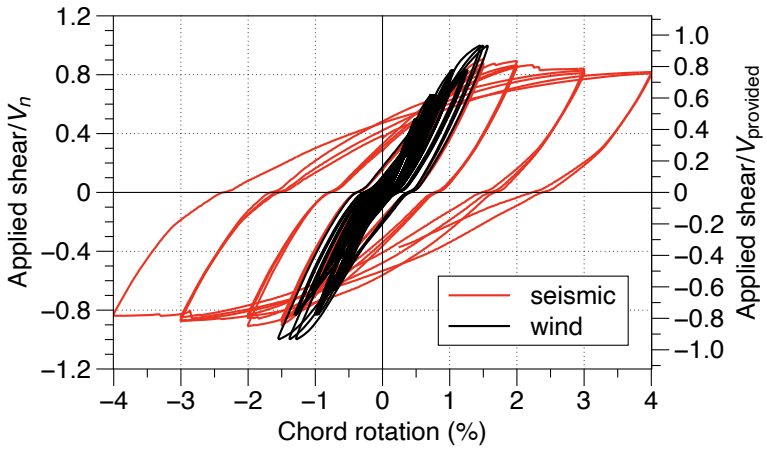

Figure 3.36 Normalized applied shear vs. chord rotation – specimen 5 (test 7).

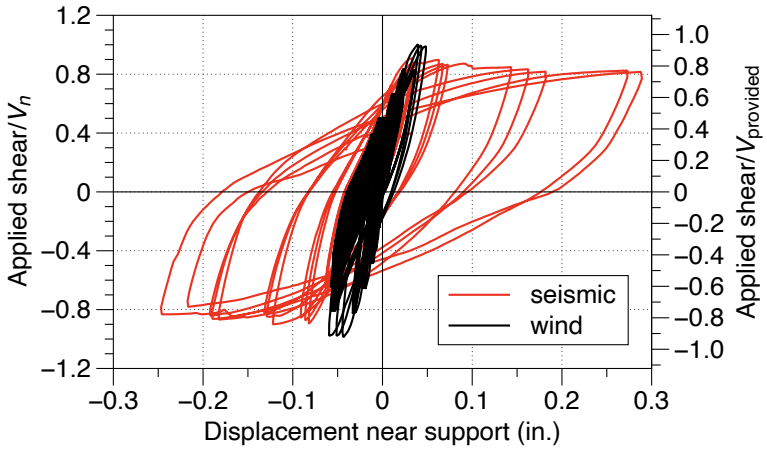

Figure 3.37 Normalized applied shear vs. displacement near support – specimen 5 (test 7).

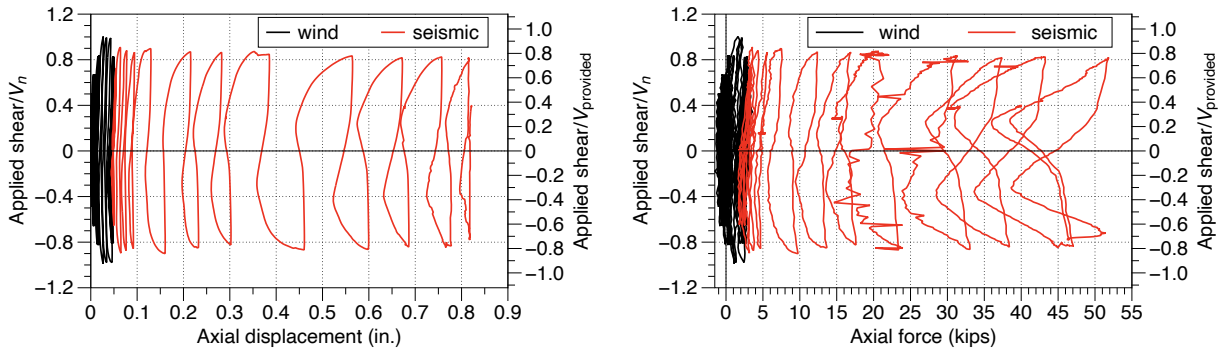

(a) Axial displacement (b) Axial force

Figure 3.38 Normalized applied shear vs. coupling beam axial displacement and axial force – specimen 5 (test 7).

The flanges yielded during the application of wind load protocol, see Figure 3.39. The maximum strain in the west flange and east flange was 1.29 and 1.06 times the yield strain, respectively. The variation of maximum shear strain in the web at the midspan is plotted against the applied shear stress in Figure 3.40. For clarity, the results are shown separately for wind and seismic protocols. Up to $0.83V_n$, there is no sudden jump in the maximum shear strain and the maximum shear strain remained below shear yield strain, but the web at the mid-depth of the beam in specimen 4 (test 6) yielded when it was subjected to $0.83V_n$. During the first cycle at V_n, the web in specimens 4 and 5 yielded although the strain in specimen 4 ($2.53\gamma_y$) was about 1.3 times larger than in specimen 5 ($1.47\gamma_y$). The maximum shear strain in specimen 4 increased

appreciably before failure when subjected to the second cycle at V_n whereas the maximum shear strain in specimen 5 became slightly smaller: $3.01\gamma_y$ vs. $1.34\gamma_y$. When subjected to seismic cycles, the maximum shear strain did not increase because the shear forces that could be resisted were smaller than V_n as a result of damage in the connection region that reduced the stiffness during the win loa tests.

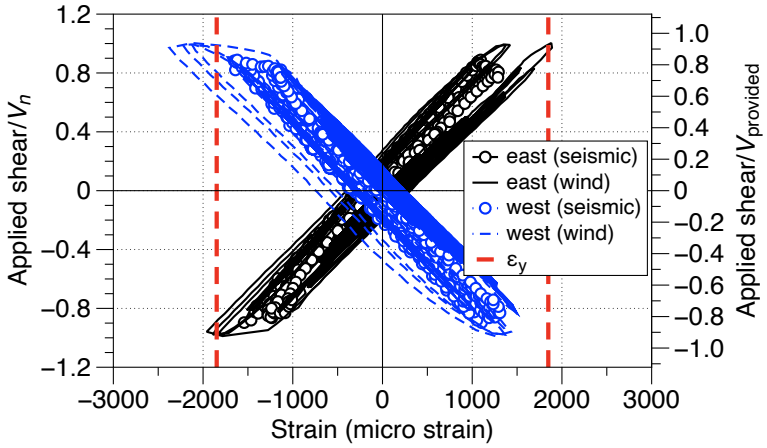

Figure 3.39 Normalized applied shear vs. beam flange strains – specimen 5 (test 7).

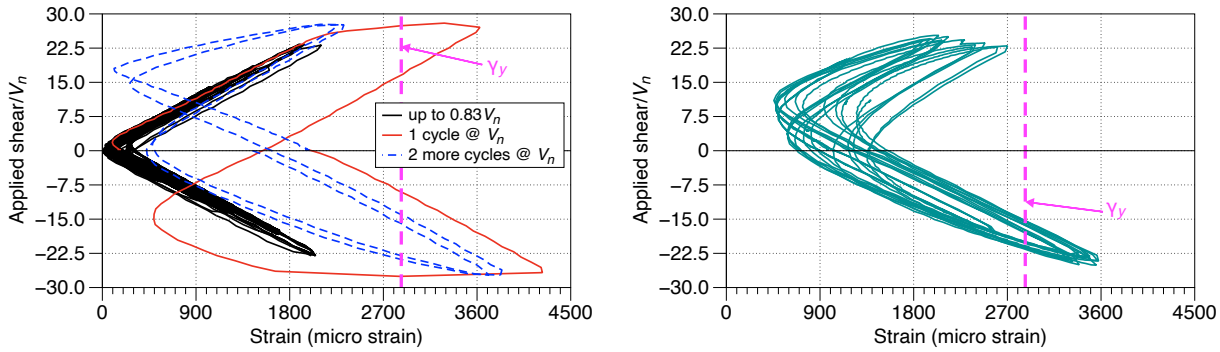

(a) Wind protocol (b) Seismic protocol

Figure 3.40 Shear stress vs. maximum shear strain – specimen 5 (test 7).

Specimen 4 had a longer embedment length than specimen 5 but did not have auxiliary transfer bars. Although the web in both specimens yielded, the responses of these two specimens were quite different. Specimen 4 failed after one cycle at V_n, but specimen 5 did not fail and the entire wind load protocol could be completed. Therefore, the sudden loss of stiffness of

specimen 4 (Figure 3.30 or Figure 3.31) and its eventual failure is attributed to connection failure and not yielding of the coupling beam. The auxiliary transfer bars in specimen 5 prevented connection failure.

The level of damage was generally similar to specimen 3 (test 5), which had the same embedment length as specimen 5 (test 7), see Figure 3.41. No evidence of flange and web local bending and buckling could be found. On the South and North face, 8 in. and 9.75 in. of concrete had been crushed between the flanges and could be removed. However, the depth of the gap between the flange and wall was less than specimen 3: 5-3/8 in. compared to 8.5 in. The auxiliary transfer bars served two purposes: (1) they provided an additional source to resist bearing forces against the coupling beam's flanges in the embedment region, and (2) they contributed significantly towards restraining the "ratcheting effect" from the actuator. The latter contribution is evident from Figure 3.41c and Figure 3.41d that show excessive bending of the bars and weld fracture of the couplers. The presence of auxiliary transfer bars is attributed to specimen 5 (test 7) being able to resist V_n and completing the full wind load protocol followed by performing the seismic cycles.

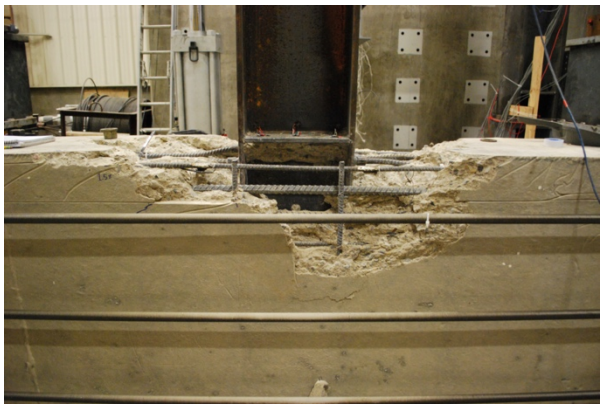

(a) South face

(b) North face

(c) Bending in auxiliary transfer bar

(d) Coupler weld fracture

Figure 3.41 Damage in specimen 5 (test 7) at the conclusion of seismic load protocol testing after removing loose concrete.

3.9 Specimen 6 (test 8)

The difference between this specimen and specimen 3 (test 5) and specimen 5 (test 7) is the presence of additional reinforcement to confine the concrete around the embedment length. However, specimen 6 suddenly failed at $0.79V_n$ during the first cycle aimed at achieving $0.83Vn$. The sudden loss of stiffness leading to failure is evident from Figure 3.42 and Figure 3.43. The chord rotation was increased from nearly 2% at the maximum applied shear of $0.79V_n$ to 5.6% when the applied shear was $0.76V_n$, or the coupling displacement at 2-1/2 in. from the face of the support was increased more than threefold. A similar trend is observed from the axial displacement of the coupling beam and the axial restraint apparatus's force shown in Figure 3.44a and Figure 3.44b, respectively. The flange on the east side had marginally yielded (the

strain was 1.06 times the yield strain) before failure, see Figure 3.45. Immediately before the loss of load-carrying capacity, the web at the mid-depth yielded – the maximum shear strain reached a value of $1.05\gamma_y$ at $0.76V_n$. Considering the level of strains in the flange and web, the sudden loss of stiffness and failure is attributed to extensive damage in the connection region. It is not clear why the connection performed poorly despite having confining reinforcement.

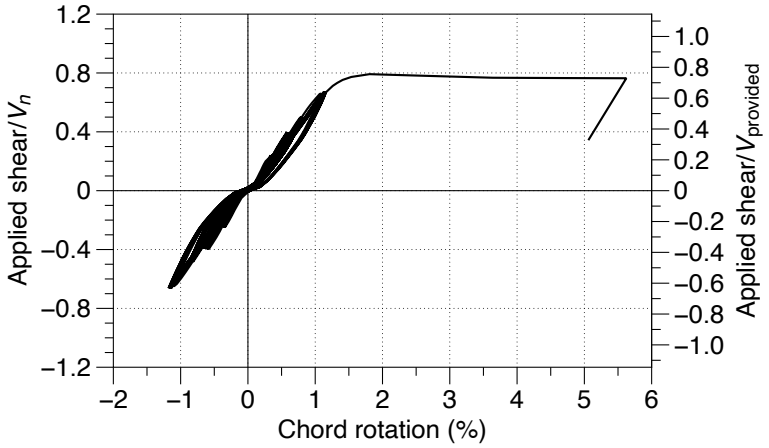

Figure 3.42 Normalized applied shear vs. chord rotation – specimen 6 (test 8).

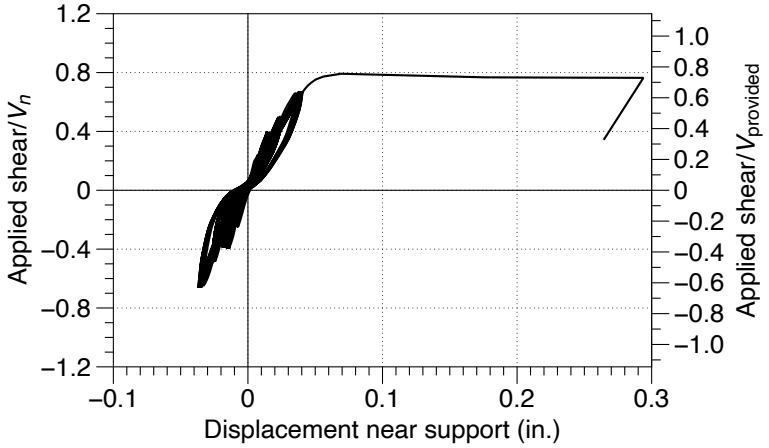

Figure 3.43 Normalized applied shear vs. displacement near support – specimen 6 (test 8).

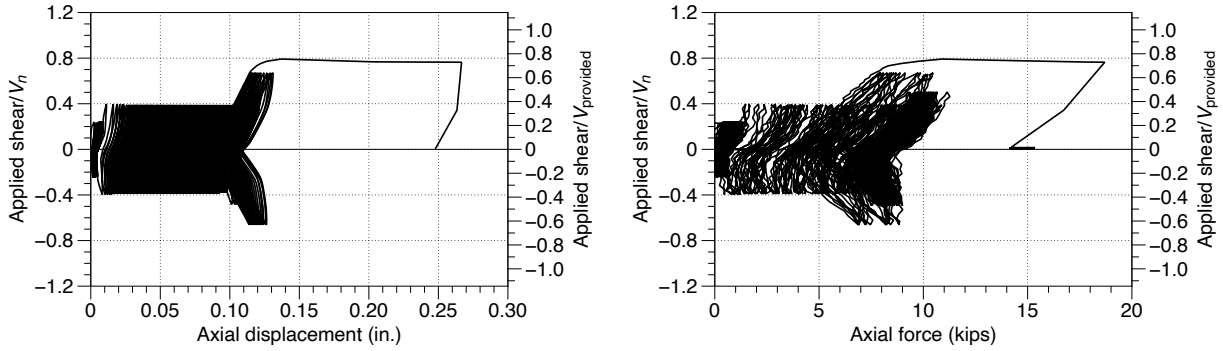

(a) Axial displacement (b) Axial force

Figure 3.44 Normalized applied shear vs. coupling beam axial displacement and axial force – specimen 6 (test 8).

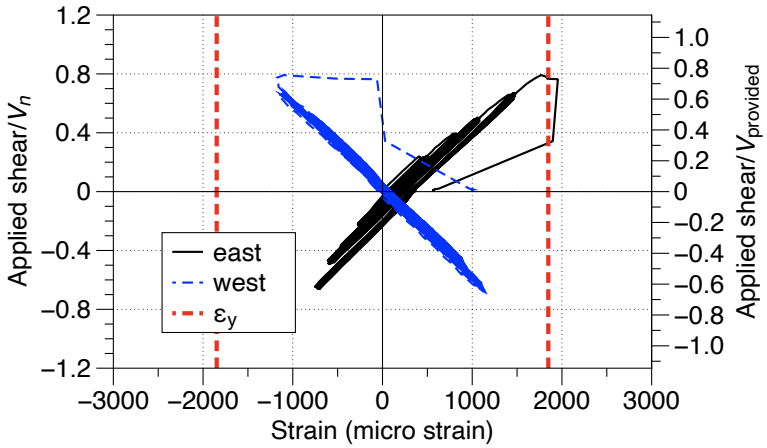

Figure 3.45 Normalized applied shear vs. beam flange strains – specimen 6 (test 8).

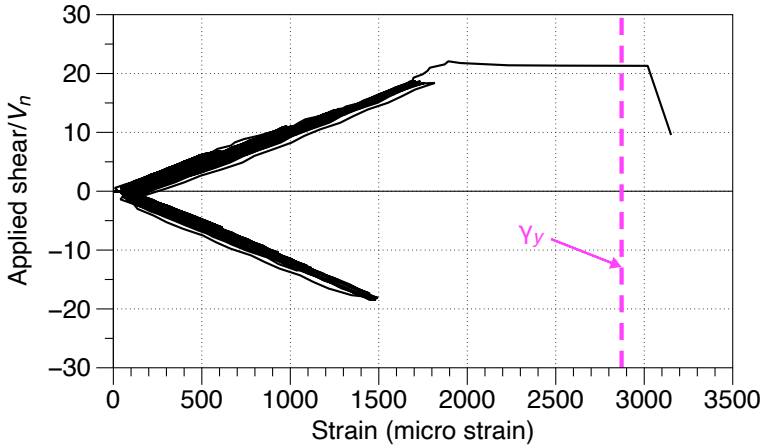

Figure 3.46 Shear stress vs. maximum shear strain – specimen 6 (test 8).

The level of damage was similar to the other specimens that could undergo more cycles and larger forces (Figure 3.47a and Figure 3.47b). Despite the presence of confinement reinforcement, major crushing occurred near the flanges (Figure 3.47e). Approximately 3 in. of concrete had been crushed and could easily be removed. A 4.5-in. deep gap was found between the flange and wall. The concrete between the flanges had been crushed and could easily be removed. The depth of the crushed concrete between the flanges was 9-5/8 in. on the North face and 10 in. on the South face (Figure 3.47c). Additionally, the flange on the north-west corner was found to have been locally bent below the face bearing plates (Figure 3.47d), but the web did not bend nor did it buckle locally.

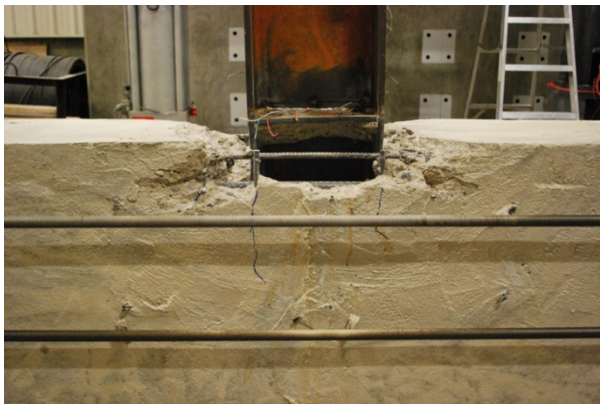

(a) South face

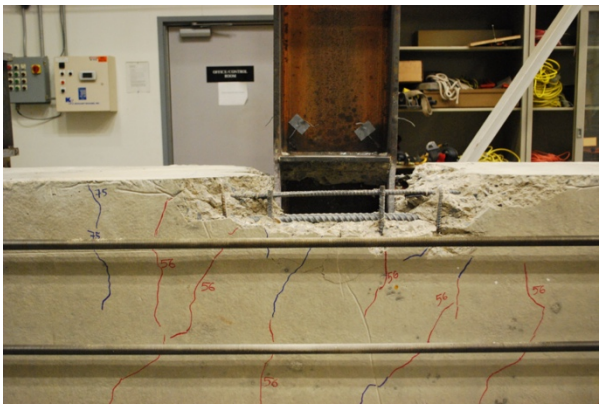

(b) North face

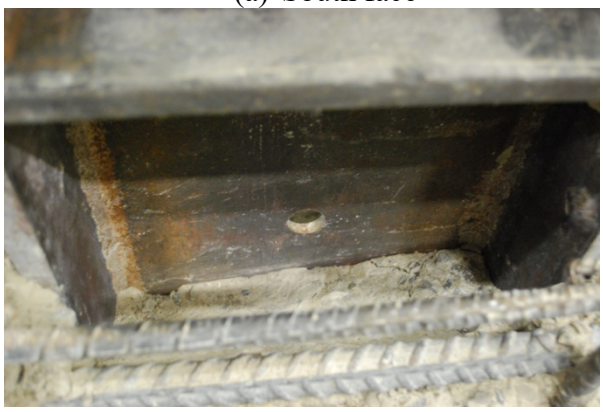

(c) Crushing between flanges

(d) Local flange bending

(e) Damage around flange

Figure 3.47 Damage in specimen 6 (test 8) after removing loose concrete.

3.10 Evaluation of comparable specimens

Several metrics were used to assess the impact of embedment length and detailing of the embedded region. Most of these comparisons are limited to the results obtained from wind load protocol tests.

3.10.1 Backbone curves and stiffness

The peak value of the applied load and the corresponding displacement at the coupling beam's tip were determined for each cycle. These values were averaged to obtain the peak values for each load step. The resulting values were used to define the backbone curves that are shown in Figure 3.48. In the following discussions, the backbone curves of similar specimens are compared. To see potential differences, only the data within $V/V_n = \pm 1.2$ and chord rotation = ± 2% are shown. Additionally, peak-to-peak stiffness for each cycle was determined. The variation of stiffness throughout testing is illustrated in Figure 3.49. As expected, the connection stiffness degraded as the load level was increased. For a few cases, the stiffness during the second set of loading became larger than that during the first set of loading. This trend, which also has been observed by others (Hill et al., 2023), is deemed to be because the "shakedown" effects occurring during the first set of loading were overcome when the load was increased in the subsequent loading steps.

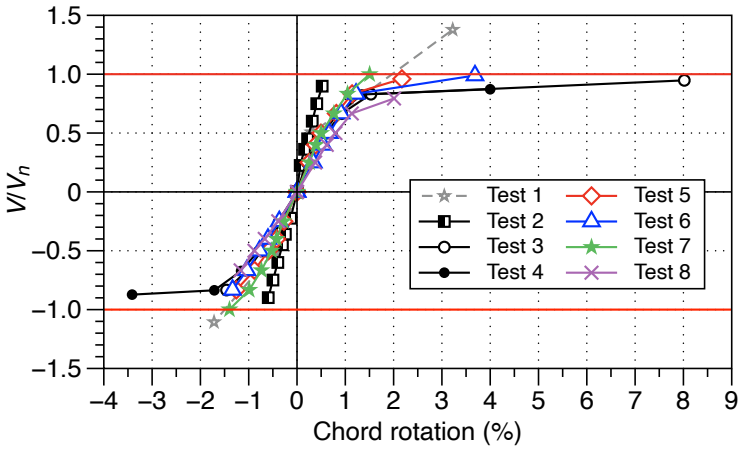

Figure 3.48 Backbone curves.

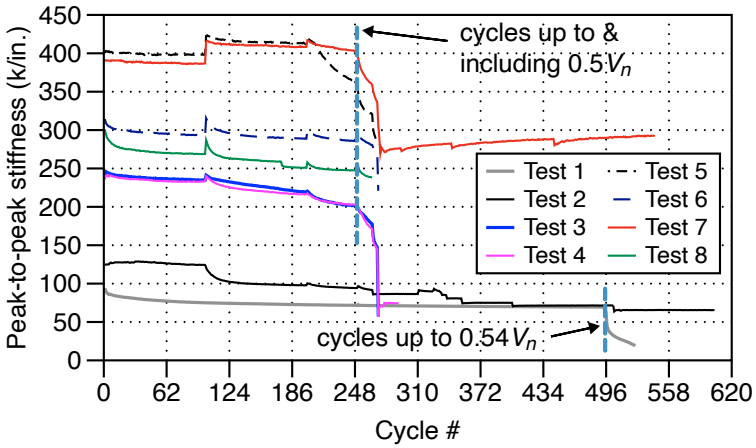

Figure 3.49 Variation of peak-to-peak stiffness.

Specimens 1a (test 1) and 1b (test 2) were identical except for the embedment length and reinforcement along the embedded region; specimen 1a was designed per AISC 341-16 while specimen 1b was designed according to AISC 341-22. As discussed in Chapter 2, specimen 1a was subjected to 495 load cycles corresponding to $0.54V_n$ before being subjected to $1.43V_n$. Up to approximately $0.54V_n$, specimen 1b was subjected to 100 cycles at $0.25V_n$, 100 cycles at $0.40V_n$, and 50 cycles at $0.50V_n$. As seen from Figure 3.50, specimen 1a exhibits a smaller stiffness (indicated by a shallower slope of the normalized applied shear – chord rotation backbone curve) than specimen 1b. A similar trend is observed by comparing the peak-to-peak

stiffness (Figure 3.49). The lower stiffness is attributed to specimen 1a being subjected to more cycles with larger load levels than specimen 1b. Specimen 1a lost a significant amount of stiffness when subjected to $1.43V_n$, which should be expected as the load exceeded the design force (V_n) by 43%.

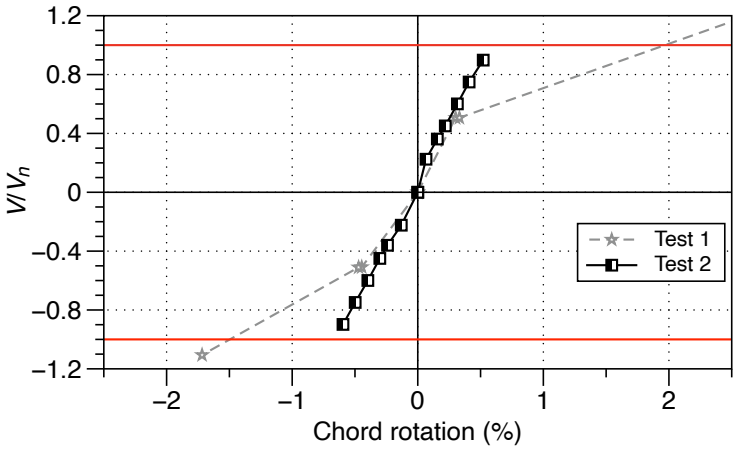

Figure 3.50 Comparison of backbone curves of specimen 1a (test 1) and specimen 1b (test 2).

Specimens 2a and 2b (test 3 and test 4, respectively) were also comparable except for the additional longitudinal reinforcement required by AISC 341-22 over the embedment length. These two specimens were subjected to identical loading protocols. The backbone curves of these two specimens are nearly identical (Figure 3.51) even though specimen 2b (test 4), which had been designed according to AISC 341-22, had more longitudinal reinforcement than specimen 2b (test 3). The stiffness of these two specimens is also similar (Figure 3.49).

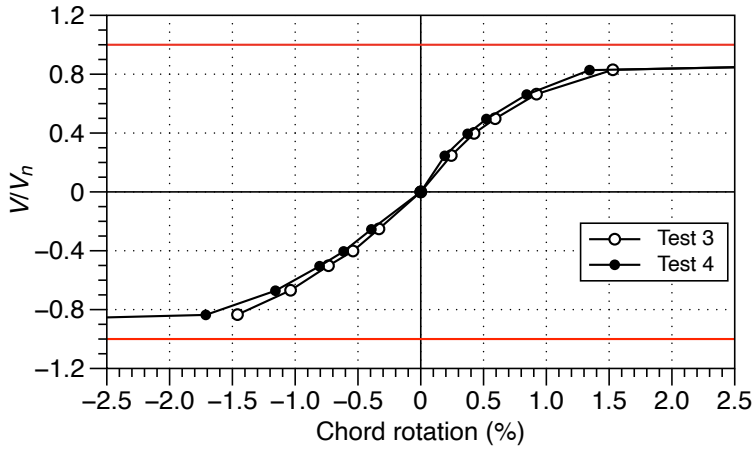

Figure 3.51 Comparison of backbone curves of specimen 2a (test 3) and specimen 2b (test 4).

In terms of the amount of longitudinal reinforcement along the embedment length, specimens 3 to 6 (tests 5 to 8) were very similar as they all had been designed per AISC 341-22. The longer embedment length in specimen 4 (test 6) resulted in a slightly different amount of longitudinal reinforcement. As discussed in Section 3.9, specimen 6 (test 8) performed much worse than the other specimens. This trend is visible from Figure 3.52; specimen 6 (test 8) had the lowest stiffness (among tests 5-8), particularly for the positive cycles. The peak-to-peak stiffness shown in Figure 3.49 also indicates the same observation. Although specimen 4 (test 6) had the longest embedment length, its stiffness (assessed from the backbone curve's slope and peak-to-peak stiffness) was less than what specimen 3 (test 5) or specimen 5 (test 7) could achieve. The concrete quality in specimen 4 is somewhat questionable due to the extra water that had to be added onsite to the concrete mix. The difference between specimen 3 (test 5) and specimen 5 (test 7) was the presence of auxiliary transfer bars in specimen 5. There is no discernable difference between the backbone curves of these specimens up to $0.87V_n$ for the positive cycles. Specimen 5 (test 7) exhibited a larger stiffness (i.e., a steeper slope) for the negative cycles, but its peak-to-peak stiffness is rather similar to specimen 3 (test 5) as evident

from Figure 3.49. The auxiliary transfer bars did not apparently enhance stiffness but increased the load-carrying capacity.

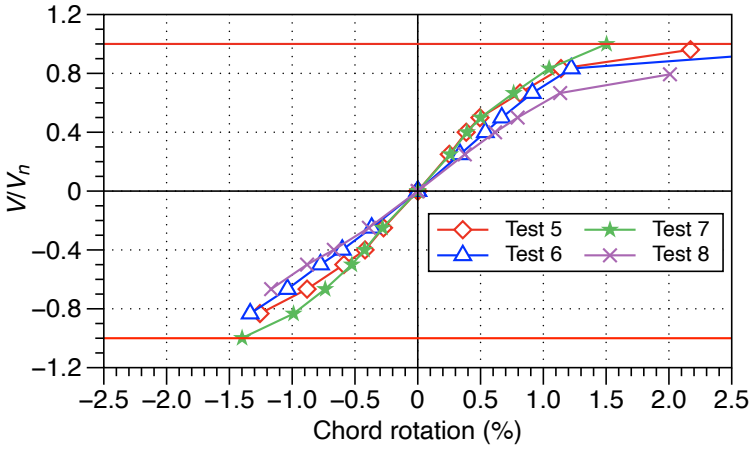

Figure 3.52 Comparison of backbone curves of specimens 3–6 (tests 5–8).

3.10.2 Strains in reinforcing bars

As discussed in Chapter 1, one of the changes in AISC 341-2022 results in more longitudinal reinforcement over the embedment length. Strain gages were bonded to a number of key reinforcing bars (see Chapter 2) primarily to examine the influence of the additional reinforcement. The strains corresponding to the largest applied shear are summarized in Table 3.1 and Table 3.2 for the specimens in phase 1 and phase 2, respectively in terms the yield strain (ε_y) determined from material testing. In specimen 6 (test 8), which failed suddenly when the applied shear was only $0.79V_n$, the longitudinal reinforcing bars farthest from the face of the wall marginally yielded – the maximum strain was 1.1 ε_y. For the other specimens, the longitudinal reinforcing bars did not yield. The maximum strain in specimens 2a and 2b (tests 3 and 4) is not appreciably different even though specimen 2b had more longitudinal reinforcement as required by AISC 341-22, e.g., $0.29\varepsilon_y$ vs. $0.19\varepsilon_y$ for specimen 2a and specimen 2b, respectively for the reinforcing bars closest to the exterior face of the wall (gage 1). The additional reinforcement in specimen 2b could not be engaged, i.e., did not yield, before the connection failed.

The discussions in Section 3.10.1 indicate that specimen 3 (test 5) and specimen 5 (test 7) performed similarly in terms of the backbone curves and peak-to-peak stiffness. However, the strains in comparable reinforcing bars in specimen 5 are much smaller than their counterparts in specimen 3, e.g., the largest strain during wind load tests is $0.90\varepsilon_y$ in specimen 3 vs. $0.093\varepsilon_y$ in specimen 5. The additional resistance mechanism provided by the auxiliary transfer bars reduced the demands in the longitudinal reinforcing bars.

Table 3.1 Strains in instrumented reinforcement at peak load– phase 1 specimens.

Specimen 1a (test 1)			Specimen 2a (test 3)		
Gage ID[a]	497 cycles @ 0.54Vn	30 cycles @ 1.43Vn	Gage ID	Wind	Seismic
SG 1	$0.0070\varepsilon_y$	$0.39\varepsilon_y$	SG 1	$0.29\varepsilon_y$	$0.15\varepsilon_y$
SG 2	$0.0081\varepsilon_y$	$0.41\varepsilon_y$	SG 2	$0.13\varepsilon_y$	$0.046\varepsilon_y$
Specimen 1b (test 2)			SG 3	$0.12\varepsilon_y$	$0.042\varepsilon_y$
Gage ID	Wind	Seismic	SG 4	$0.11\varepsilon_y$	$0.15\varepsilon_y$
SG 1	$0.038\varepsilon_y$	$0.54\ \varepsilon_y$	Specimen 2b (test 4)		
SG 2	$0.029\varepsilon_y$	$0.71\varepsilon_y$	Gage ID	Wind	Seismic
SG 3	$0.024\varepsilon_y$	$0.98\varepsilon_y$	SG 1	$0.19\varepsilon_y$	$0.13\varepsilon_y$
SG 4	$0.059\varepsilon_y$	$0.39\varepsilon_y$	SG 2	$0.16\varepsilon_y$	$0.11\varepsilon_y$
SG 5	$0.054\varepsilon_y$	$0.61\varepsilon_y$	SG 3	$0.10\varepsilon_y$	$0.015\varepsilon_y$
SG 6	$0.037\varepsilon_y$	$0.43\varepsilon_y$	SG 4	$0.087\varepsilon_y$	$0.17\varepsilon_y$
			SG 5	$0.052\varepsilon_y$	---[b]
			SG 6	$0.087\varepsilon_y$	$0.068\varepsilon_y$
			SG 7	$0.070\varepsilon_y$	$0.056\varepsilon_y$
			SG 8	$0.081\varepsilon_y$	$0.17\varepsilon_y$

[a] see Figure 3.53
[b] strain gage was lost.

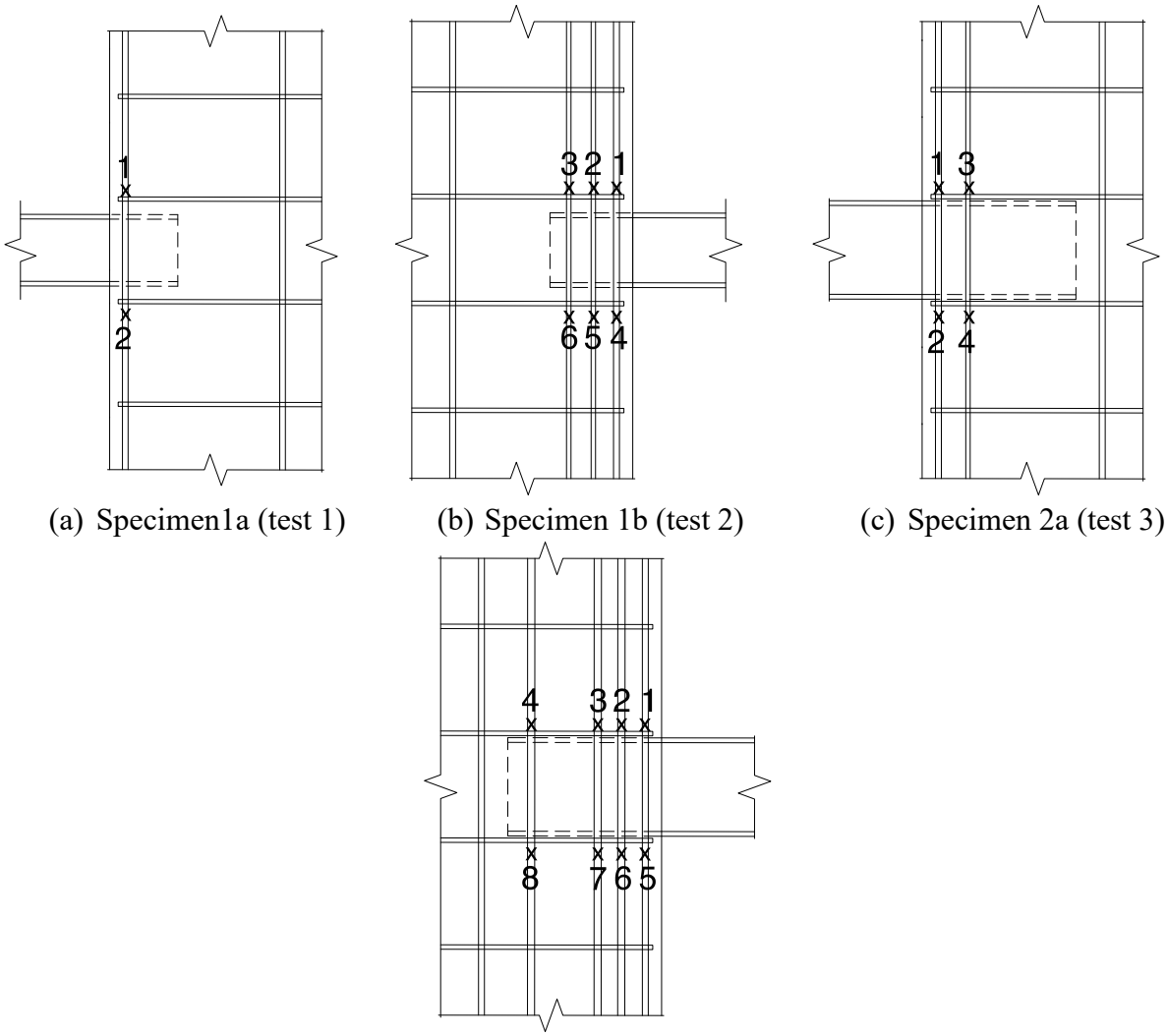

(a) Specimen1a (test 1) (b) Specimen 1b (test 2) (c) Specimen 2a (test 3)

(d) Specimen 2b (test 4)

Figure 3.53 Locations of strain gages – phase1 specimens.

Table 3.2 Strains in instrumented reinforcement at peak load – phase 2 specimens.

Specimen 3 (test 5)			Specimen 4 (test 6)		
Gage ID[a]	Wind	Seismic	Gage ID	Wind	Seismic
SG1	$0.27\varepsilon_y$	$0.17\varepsilon_y$	SG1	$0.70\varepsilon_y$	not conducted
SG2	$0.063\varepsilon_y$	$0.061\varepsilon_y$	SG2	$0.30\varepsilon_y$	
SG3	$0.90\varepsilon_y$	$0.54\varepsilon_y$	SG3	$0.74\varepsilon_y$	
SG4	$0.20\varepsilon_y$	$0.057\varepsilon_y$	SG4	$0.35\varepsilon_y$	
SG5	$0.039\varepsilon_y$	$0.052\varepsilon_y$	SG5	$0.18\varepsilon_y$	
SG6	$0.25\varepsilon_y$	$0.03\varepsilon_y$	SG6	$0.28\varepsilon_y$	
SG7	$0.27\varepsilon_y$	$0.43\varepsilon_y$	SG7	$0.34\varepsilon_y$	
SG8	$0.033\varepsilon_y$	$0.038\varepsilon_y$	SG8	$0.30\varepsilon_y$	
Specimen 5 (test 7)			Specimen 6 (test 8)		
Gage ID	Wind	Seismic	Gage ID	Wind	Seismic
SG1	$0.087\varepsilon_y$	$0.16\varepsilon_y$	SG1	$0.45\varepsilon_y$	not conducted
SG2	$0.086\varepsilon_y$	$0.023\varepsilon_y$	SG2	$0.21\varepsilon_y$	
SG3	$0.025\varepsilon_y$	$0.022\varepsilon_y$	SG3	$0.20\varepsilon_y$	
SG4	$0.018\varepsilon_y$	$0.041\varepsilon_y$	SG4	$1.1\varepsilon_y$	
SG5	$0.078\varepsilon_y$	$0.32\varepsilon_y$	SG5	$0.94\varepsilon_y$	
SG6	$0.026\varepsilon_y$	$0.045\varepsilon_y$	SG6	$0.26\varepsilon_y$	
SG7	$0.093\varepsilon_y$	$0.017\varepsilon_y$	SG7	$0.38\varepsilon_y$	
SG8	$0.062\varepsilon_y$	$0.094\varepsilon_y$	SG8	$1.0\varepsilon_y$	
[a] see Figure 3.54					

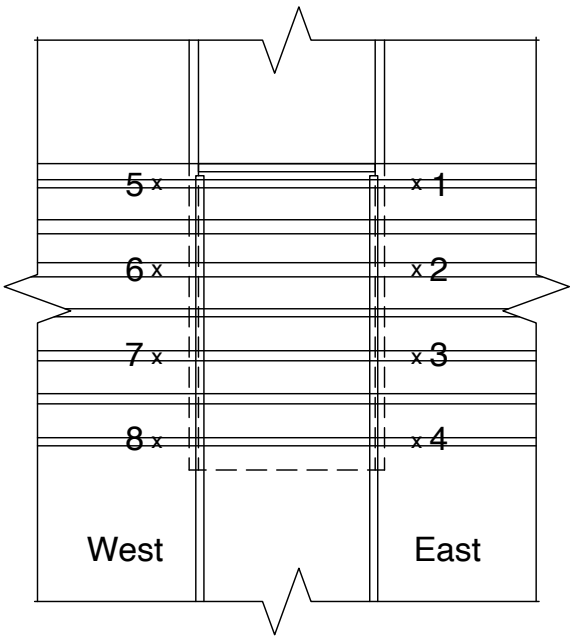

Figure 3.54 Locations of strain gages – phase2 specimens.

3.10.3 Energy dissipation

The area of the hysteresis loops from beam applied shear-tip deflection curves indicates the dissipated energy. The level of energy dissipation denotes the level of inelasticity and damage. The cumulative dissipated energies are compared in Figure 3.55. The x-axis denotes the wind loading steps presented in Table 2.9. The comparison is made separately for the specimens in phase 1 and phase 2 because of their differences. The loading protocol was different for specimen 1a and 1b (tests 1 and 2); therefore, the energy dissipation of these two specimens is not compared.

Consistent with the previous observations made from backbone curves, stiffness, and strains in longitudinal reinforcement along the embedment length, no discernable difference is observed between specimen 2a (test 3) and specimen 2b (test 4) even though specimen 2b had more longitudinal reinforcement per AISC 341-22. Specimen 6 (test 8), which failed at a much smaller load than the other second phase specimens, dissipated the most amount of energy. The larger energy dissipation is consistent with this specimen having the lowest stiffness. Specimen 5 (test 7), which had auxiliary transfer bars, dissipated the least amount of energy up to the last step that the other specimens could be tested. The additional resistance mechanism provided by the auxiliary transfer bars minimized the level of damage in the connection region.

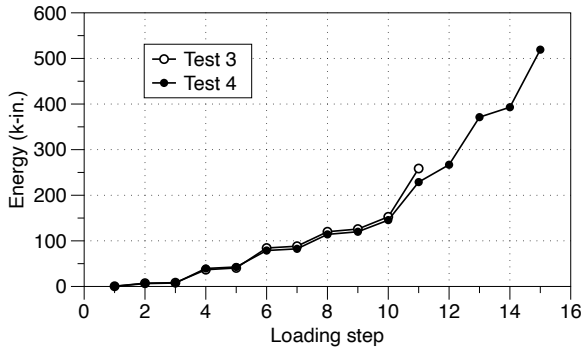

(a) Phase 1 specimens

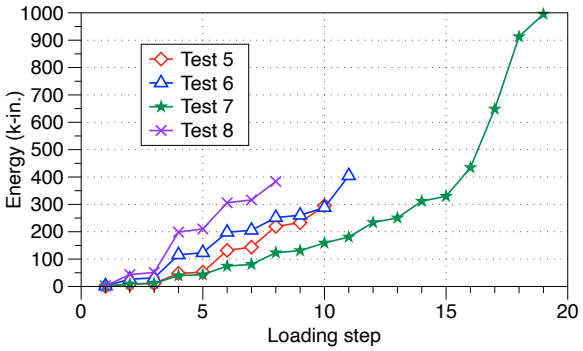

(a) Phase 2 specimens

Figure 3.55 Comparison of dissipated energy.

3.11 Strength

The connections were designed using Eq 3.1, which is the current equation H4-1 in AISC 341-22. Using the measured material properties and the as-built dimensions, the connection capacities were calculated according to Eq 3.1. Table 3.3 compares the maximum applied shear against the design shear and the calculated value.

$$V_n = 1.54\sqrt{f_c'}\left(\frac{b_w}{b_f}\right)^{0.66}\beta_1 b_f L_e\left[\frac{0.58-0.22\beta_1}{0.88+\frac{g}{2L_e}}\right] \quad \textbf{Eq 3.1}$$

Only specimen 1a (test 1), specimen 1b (test 2), specimen 4 (test 6), and specimen 5 (test 7) could reach their target design V_n although specimen 4 failed during the second application of V_n. However, none of the specimens could develop their respective calculated capacities except for specimens 1a and 1b (tests 1 and 2). Therefore, the application of Eq 3.1 for low seismic regions needs to be reexamined. This equation is based on assuming a linear strain distribution, maximum concrete strain (ε_f) of 0.003, and the ratio of the neutral axis depth to the embedment length (c/L_e) = 0.66 – see Figure 3.56.

Table 3.3 Calculated and measured connection capacity.

Specimen ID	Test ID	Design V_n (kips)	V_n (kips) from Eq 3.1[a]	Test V_{max} (kips)	Test/ Design V_n	Test/ Calculated
1a	1	10	11.8	14.2	1.42	1.20
1b	2	10	15.5	20.4	2.04	1.32
2a	3	49.4	56	49	0.99	0.88
2b	4	49.4	56	47.4	0.96	0.85
3	5	113	122	109	0.96	0.89
4	6	113	158	113[b]	1.00	0.72
5	7	113	121	113[c]	1.00	0.93
6	8	113	118	89.7	0.79	0.76

[a] based on as-built dimensions and measured material properties
[b] failed during the second application of V_n
[c] maximum load used for testing

Eq 3.1 has been found to be adequate based on a large of number of past studies focused on special coupled walls (with boundary element reinforcement) for which the embedment length had been calculated to develop the coupling member capacity, i.e., the lesser of $2(1.1R_y)M_p/g$ and $1.1R_yV_p$. The past specimens were subjected to a relatively small number of cycles (approximately 60 or less) of loads/displacements with increasing amplitudes. The experimental data from the current research indicate Eq 3.1 is inadequate for ordinary coupled walls with no boundary element reinforcement, cases in which the embedment length is determined to develop V_n, and when the connection is subjected to many cycles (more than 500) of loads/displacements with increasing amplitudes. Therefore, a new equation is necessary for computing the required embedment length in ordinary coupled walls.

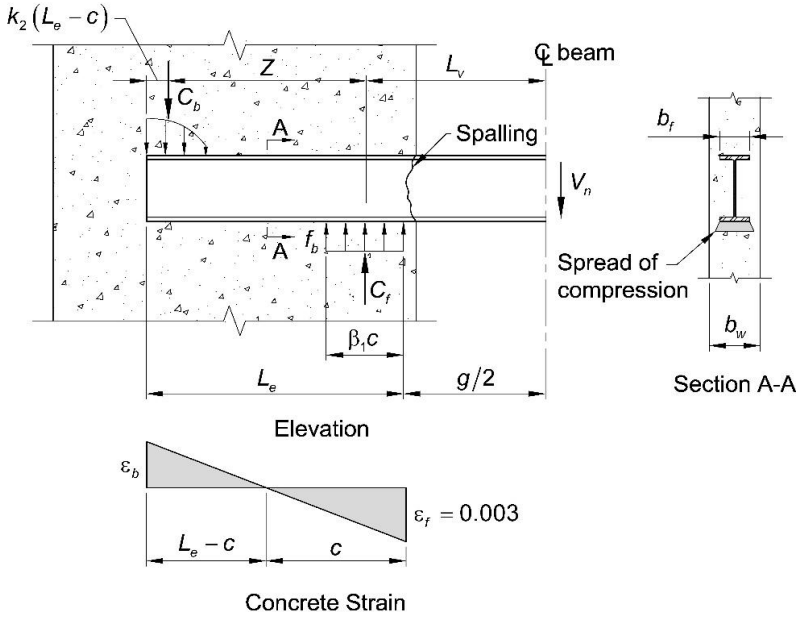

Figure 3.56 Modeling assumptions for Eq 3.1 (Source: AISC 341-22).

3.11.1 Development of a new design equation

The model shown in Figure 3.57 was used to assess the measured capacities. The strain at the wall-coupling beam interface (ε_f) and the depth of the neutral axis (c) were allowed to vary in order to maintain equilibrium of the vertical forces and moment. The concrete constitutive

relationship consisted of a parabolic ascending branch with a linear post-peak descending branch. The selected model is illustrated in Figure 3.58. The peak concrete strength (f_c) was taken as $0.85f'_c$. Figure 3.57 illustrates two cases with $\varepsilon_f \leq \varepsilon_{01}$ and $\varepsilon_f > \varepsilon_{01}$ with strain at the end of the connection (ε_b) being less than ε_{01}. However, the actual calculations were based on $\varepsilon_b \leq \varepsilon_{01}$ or $\varepsilon_b > \varepsilon_{01}$. The bearing forces were determined using the coupling beam flange width, i.e., no "spreading" beyond the flange width was considered. On the other hand, in the derivation of Eq 3.1, the term $1.54\sqrt{f'_c}\left(b_w/b_f\right)^{0.66}$ implicitly is based on relying on the bearing stresses beyond the flange width. The value of applied shear (V) was incrementally increased, and the values of ε_f and c were iterated until equilibrium could be achieved. The connection capacity was taken as the maximum V for which equilibrium was possible.

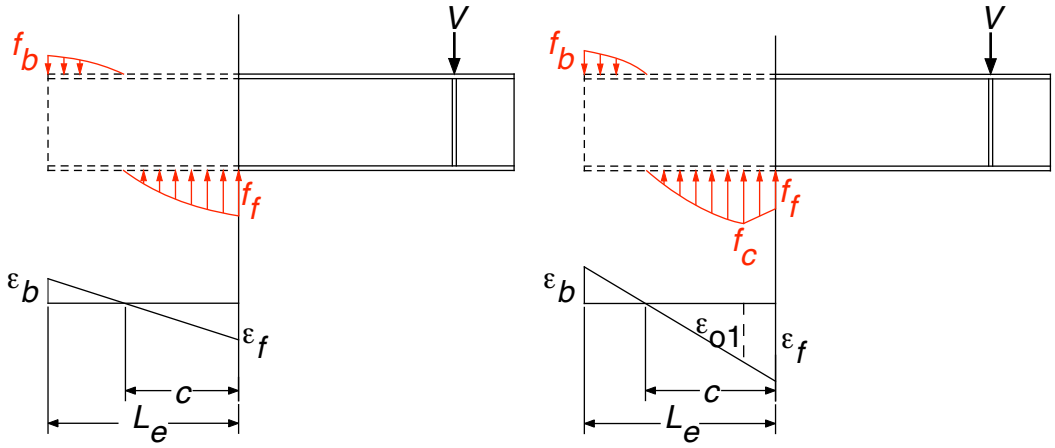

Figure 3.57 Model for computing connection capacity.

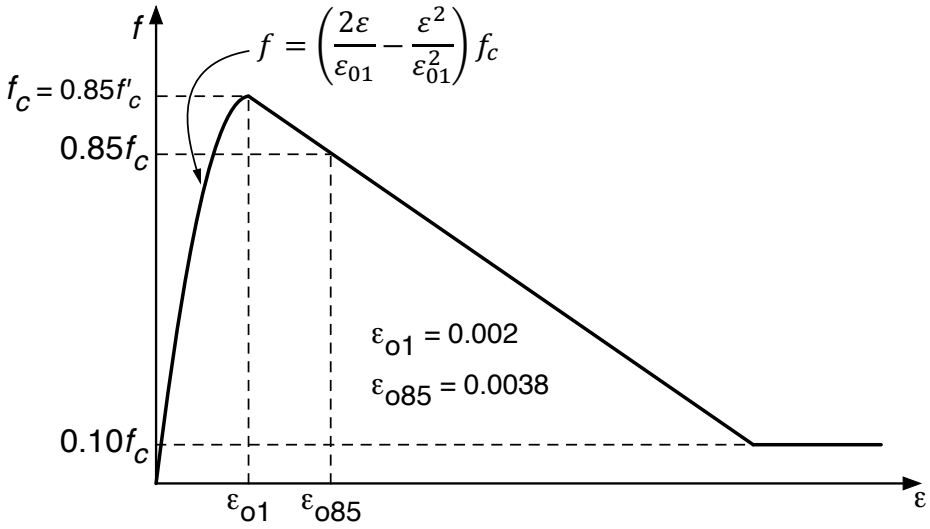

Figure 3.58 Concrete constitutive model.

For specimen 5 (test 7), which had auxiliary transfer bars, the same modeling approach was used except for adding forces from the auxiliary transfer bars – see Figure 3.59. The strain in the bars was limited to the maximum measured strain.

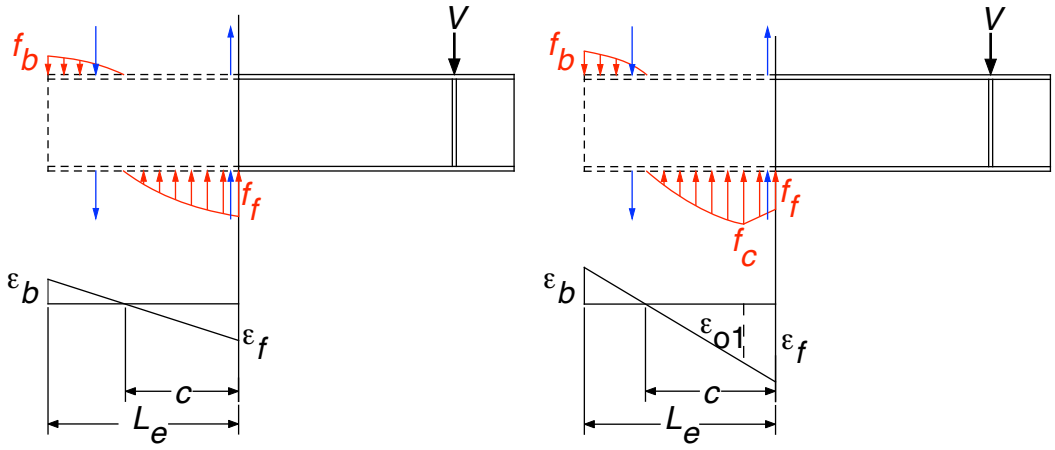

Figure 3.59 Model for computing connection capacity for specimen 5 (test 7) with auxiliary transfer bars.

Using the aforementioned methodology, the capacity of specimens 2a through 6 (tests 3 through 8) was determined. For specimens 1a and 1b (tests 1 and 2), the ratio of embedment length to coupling beam depth (L_e/d) is 1 or smaller. For such scenarios, a linear distribution of strain is not appropriate. The strut-and-tie model shown in Figure 3.60 was developed to

compute the capacities of specimens 1a and 1b. Similar to the model used for the other specimens, the strut forces were computed by limiting the bearing width to the coupling beam flange width. The strut capacity was based on using $0.85f'_c$. The value of applied shear (V) was incrementally increased, and the locations of vertical bearing forces (y_1 and y_2) were iterated until equilibrium could be achieved. The connection capacity was taken as the maximum V for which equilibrium was possible.

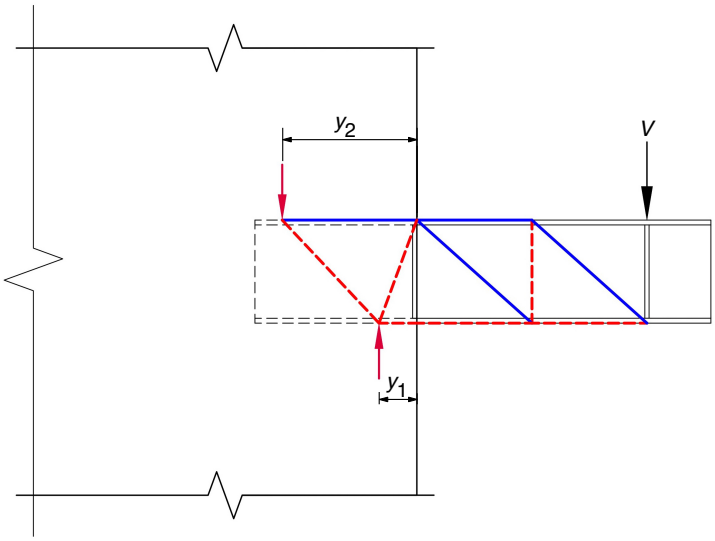

Figure 3.60 Strut-and-tie model.

As evident from Table 3.4, the calculated capacities are reasonably close to the measured values. The largest difference is for specimen 4 (test 6). As mentioned previously, water had to be added onsite to the concrete mix because of delays in casting this specimen. As a result, the "exact" concrete compressive strength for this specimen is somewhat unclear. For instance, if the concrete compressive strength is assumed to be 300 psi higher than the value obtained from the cores taken from this specimen, the measured capacity is 1.02 times the calculated capacity instead of 1.09 times.

Table 3.4 Measured vs. calculated capacity.

Specimen ID	Test ID	Measured/ Calculated	ε_f	c/L_e
1a	1	1.04	---[a]	---
1b	2	1.04	---	---
2a	3	1.03	0.00342	0.564
2b	4	1.00	0.00342	0.564
3	5	1.04	0.00337	0.563
4	6	1.09[b]	0.00370	0.575
5	7	1.04	0.00370	0.569
6	8	0.98	0.00346	0.563
		Average = 1.03 COV = 0.031 [a] Not applicable as a strut-and-tie model was used for specimens 1a and 1b. [b] Concrete strength is not reliably available for this specimen.		

3.11.2 Proposed equation

Ignoring specimen 4 (test 6), the average values of ε_f and c/L_e (provided in Table 3.4) are 0.0035 and 0.56, respectively. Ensuring equilibrium with reference to the model shown in Figure 3.61, the following equation is derived.

$$V_n = \frac{0.193 f_c' b_f L_e}{0.56 + \frac{g}{2L_e}} \qquad \textbf{Eq 3.2}$$

Using this equation, the capacities were computed. The measured and calculated equations are compared in Table 3.5. As discussed previously, a strut-and-tie model is more appropriate for specimens 1a and 1b (tests 1 and 2) with L_e/d being 1 or less than 1. Specimen 5 (test 7) had auxiliary transfer bars, which are not considered in the proposed equation nor in Eq 3.1 (AISC Eq. H4-1). The relatively large difference for specimen 4 (test 6) is attributed to the "exact" concrete strength not being known due to adding extra water onsite to the concrete mix. Excluding test 1a, 1b, and 4, the measured capacities, on average, are 3% higher than the value

obtained from the proposed equation. To simplify and be slightly conservative, it is proposed to change 0.193 to 0.19 in Eq 3.2, i.e., use Eq 3.3.

$$V_n = \frac{0.19 f_c' b_f L_e}{0.56 + \frac{g}{2L_e}} \qquad \textbf{Eq 3.3}$$

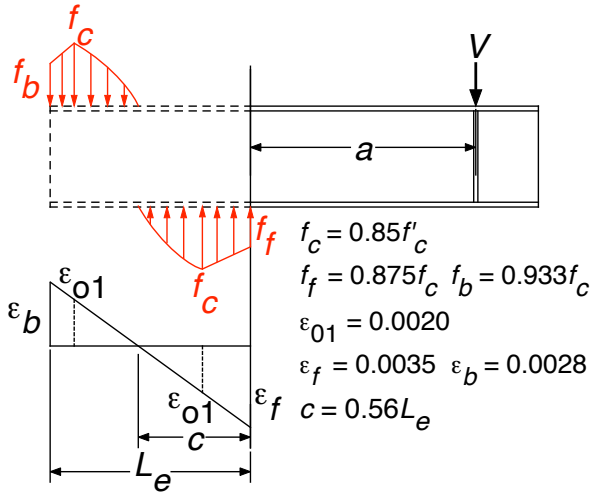

Figure 3.61 Model for derivation of proposed equation.

Table 3.5 Comparison of measured capacity vs. proposed equation.

Specimen ID	Test ID	Measured/Eq 3.3
1a	1	2.62[a]
1b	2	2.84[a]
2a	3	1.04
2b	4	1.00
3	5	1.04
4	6	1.09
5	7	1.13[b]
6	8	0.98
	Average [c]	1.03
	COV [c]	0.04

[a] Strut-and-tie model needs to be used because $L_e/d \leq 1$

[b] Specimen 5 had auxiliary transfer bars

[c] Average and COV by ignoring specimens 1a, 1b, and 5

3.11.3 Evaluation of proposed equation

The proposed equation (Eq 3.3) was further evaluated through a case study involving the archetypes used in several previous studies (Fortney, 2005; Gong, 1998; Kunwar, 2020; Remmetter, 1992; Shahrooz et al., 2018). Knowing the shear design forces, wall geometry, and selected coupling beam dimensions, the embedded length was determined from Eq 3.1. The larger of the calculated length and coupling beam depth was selected and rounded up to the nearest whole number. Using the provided embedment length, the connection capacity (V_n) was obtained by using Eq 3.1. The modeling procedure described in Section 3.11.1 was employed to compute the capacities. Considering the very good correlation of the measured capacities of the test specimens, the resulting capacities are deemed to represent the "actual" connection capacity. The connection capacity was also determined according to the proposed equation (Eq 3.3). Excluding the cases for which a strut-and-tie model is appropriate (i.e., those with $L_e/d \leq 1$), a total of 102 cases (including the test specimens) were evaluated. As seen from Figure 3.62, the current equation overestimates the calculated connection capacity, which is consistent with the observations made for the test specimens. On average, Eq 3.1 overestimates the connection capacity on average by a factor of 1.5 and by as much as a factor of 2 (see Table 3.6). For all the cases, Eq 3.1 (AISC Eq. H4-1) overestimates the connection capacity; the minimum value of V_n from Eq 3.1 is 1.17 times the computed capacity. Overestimation of the connection capacity suggests the embedment length obtained from Eq 3.1 would be insufficient. However, the capacity from the proposed equation is nearly identical to the calculated connection capacity (Figure 3.62). Similar conclusions may be arrived from the average, maximum, and minimum values of the ratio of the proposed equation (Eq 3.3) to the calculated connection capacity: 0.99, 1.00, and 0.98, respectively. Therefore, the proposed equation provides a simple yet slightly conservative method to determine the connection capacity of steel coupling beams interfaced

with ordinary structural walls, and the embedment length from the proposed equation would be adequate to develop the connection capacity.

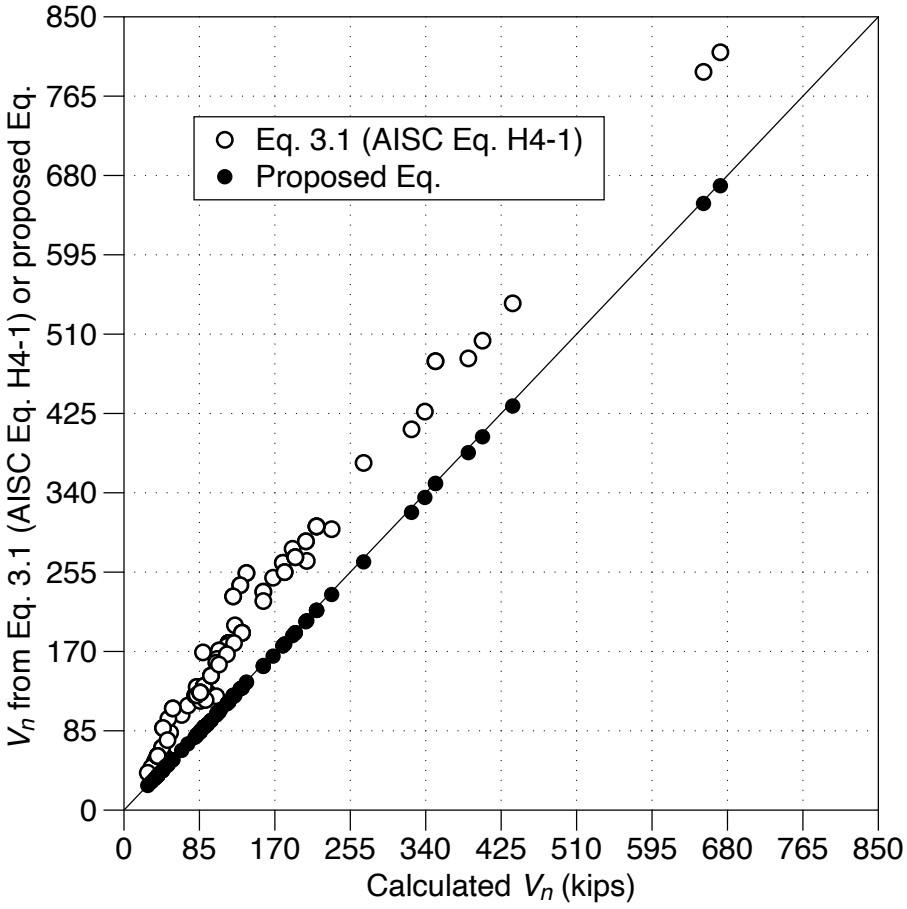

Figure 3.62 Calculated capacity vs. capacity from Eq 3.1 (AISC Eq. H4-1) and proposed equation (Eq 3.3).

Table 3.6 Comparison of V_n from Eq 3.1 and Eq 3.3 against calculated connection capacity.

	Eq 3.1 / Calculated	Eq 3.3 / Calculated
Average	1.50	0.99
COV	0.12	0.0043
Maximum	2.00	1.00
Minimum	1.17	0.98

3.11.4 Comparison of embedment length from proposed equation and current equation

The proposed equation results in a longer embedment length than the value determined from the current equation Eq 3.1. To assess the additional length, the embedment lengths for the

design cases discussed in Section 3.11.3 were calculated by using the current and proposed equations, i.e., Eq 3.1 and Eq 3.3.

Figure 3.63 illustrates the change in the required embedment lengths as calculated by the proposed equation versus the values obtained from Eq 3.1 (current AISC Eq. H4-1). In this figure, the embedment lengths required to develop the member capacity (R_yV_p) are also compared against those from Eq 3.1. The proposed equation increases the required embedment by at most 52% and 23% on average. As expected, significantly longer embedment lengths are required to develop the member capacity: 107% and 217% on average and maximum, respectively. The embedment length from the proposed equation is the same as that found from Eq 3.1, i.e., 0% change, if the beam depth controls the final value. The values shown in Figure 3.63 indicate that the proposed equation does not result in excessively long embedment lengths.

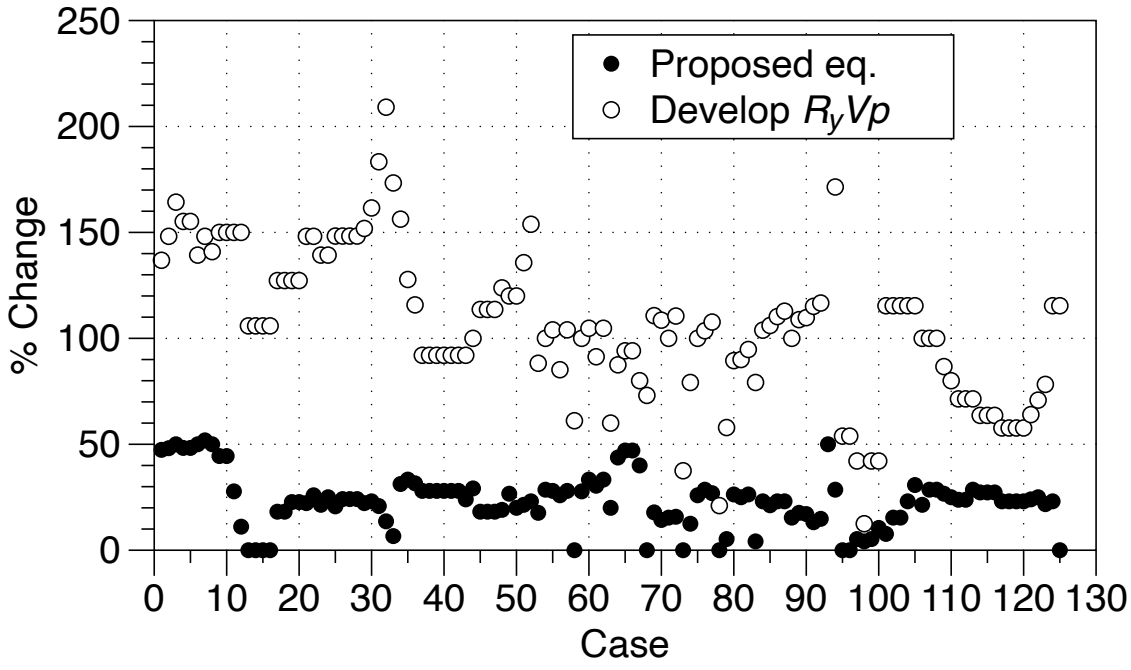

Figure 3.63 Change in embedment length compared to Eq 3.1 (AISC Eq. H4-1).

3.12 Stiffness

3.12.1 Evaluation of current equation for effective moment of inertia

The values of peak-to-peak stiffness were normalized with respect to the stiffness obtained by using the effective moment of inertia calculated from AISC Eq C-H4-1, which is provided herein as Eq 3.4.

$$I_{eff} = 0.60I\left(1 + \frac{12\lambda EI}{g^2 GA_w}\right)^{-1} \qquad \textbf{Eq 3.4}$$

The normalized peak-to-peak stiffness for each cycle is plotted in Figure 3.64. As expected, the connection stiffness degraded as the load level was increased. With few exceptions, the experimentally obtained stiffness is smaller than the value calculated from Eq 3.4 (AISC Eq C-H4-1). With 95% confidence, the average of measured stiffness (0.722) is between 0.713 and 0.730 times the value calculated using Eq 3.4 for cycles up to and including $0.54V_n$. If all the cycles are considered, the average value (0.685) is between 0.678 and 0.692 with 95% confidence.

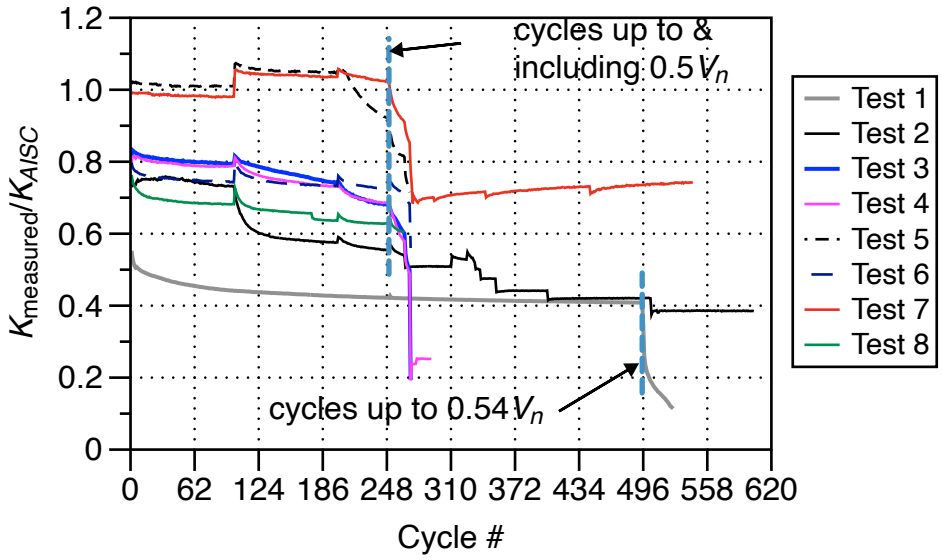

Figure 3.64 Comparison of measured stiffness vs. stiffness based on AISC I_{eff}.

The results demonstrate that the coefficient 0.60 needs to be 0.43 or 0.41 if cycles up to and including $0.5V_n$ or all cycles are considered, respectively. Therefore, it is proposed to change 0.60 to 0.40 for steel coupling beams linking ordinary reinforced concrete walls.

3.12.2 Impact of revision of effective moment of inertia

The archetype was designed based on the effective moment of inertia (I_{eff}) from Eq 3.4, which is intended to account for connection flexibility. The computer program used for design (ETABS) accounts for shear deformation; therefore, the equation's parenthetical term need not be included in the model. The coupling beam moment of inertia was multiplied by 0.6 in the computer model for design. The experimental data described in Section 3.12.1 indicate that this multiplier should be taken as 0.4. To understand the impact of this change, the archetype was reanalyzed for the same loads used in the original design but the coupling beams' moment of inertias were multiplied by 0.4.

The revised model of the archetype has lower coupling beam moments of inertia than those in the original design; hence, the distribution of forces in the wall piers are affected and the drifts are expected to be larger than the original values. The potential implications of these changes were examined by evaluating the performance of the archetype subjected to the design wind loads. The demand-to-capacity ratios of the wall piers shown in Figure 65a indicate the strength of the first-story wall is marginally insufficient; the capacity is exceeded by about 3%. More importantly, the inter-story drifts between stories 9 and 21 exceed $h/450$, but all the values are lower than $h/400$, where h is the story height. The archetype, as designed originally, had sufficient capacity, and the inter-story drift limits were satisfied.

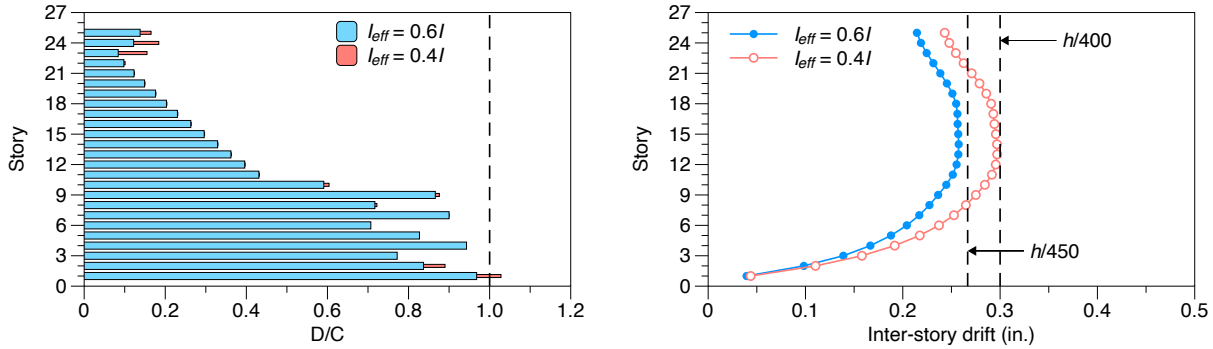

(a) Wall demand-to-capacity ratios for wind loads

(b) Inter-story drifts for wind loads

Figure 65 Comparison of original and revised performances of archetype.

Chapter 4 Summary, Conclusions, and Recommendations

4.1 Project overview

Coupled structural (shear) walls (CSW) are a common structural system. This system is comprised of two or more structural walls that are typically linked at each floor by coupling beams. Based on the expected level of inelastic deformations, composite structural (shear) walls can be classified as Composite Ordinary Shear Wall (COSW) or Composite Special Shear Wall (CSSW). The design and detailing of COSW and CSSW are presented in Sections H4 and H5 of AISC 341 *Seismic Provision*, respectively. COSW systems are used in regions with low-to-moderate seismic demands and are expected to undergo limited inelastic deformations. On the other hand, CSSW systems are used in regions with high seismic demands and are expected to undergo significant inelastic deformations. One common composite system involves linking reinforced concrete wall piers by steel (or steel-concrete composite) coupling beams that are embedded in the wall piers. Design and detailing of steel coupling beam-wall connection in COSW was the focus of the research herein.

In the 2010 and earlier versions of AISC 341 *Seismic Provisions*, the coupling beam-wall connection was designed to develop the coupling beam's expected capacity. This provision in the 2016 version was replaced by the requirement that the connection in COSW be designed only to develop the demand from the coupling beam as calculated by linear-elastic analysis with no ductile detailing requirements. As a result, design and detailing of embedment region has been relaxed. This change leads to shorter embedment lengths and smaller reinforcement in the embedment region.

Analytical studies conducted at the University of Cincinnati indicated the shorter embedment length could accelerate the loss of coupling beam-wall connection integrity, leading

to a reduction in the level of coupling action between the wall piers. The loss of coupling action will affect the demands in the wall piers, and their capacities could be exceeded. Moreover, inter-story and overall drifts could surpass acceptable limits. Partly to remedy these observations, AISC 341 was modified in 2022 by specifying a minimum embedment length of not being less than the coupling beam's depth and requiring additional longitudinal reinforcement along the embedded region.

A coordinated experimental and analytical study was conducted to examine the current design provisions for steel coupling beams in COSW outlined in AISC 341-2022. It is important to note that the current (and previous) AISC 341 *Seismic Provisions* for coupling beams in COSW and CSSW are mostly (if not entirely) based on experimental research focused on coupling beam-wall connection details intended to resist high seismic loads. To the best of the authors' knowledge, no experimental research had been conducted to understand the performance of COSW prior to the study presented in this report.

The test specimens were selected based on a 25-story archetype located in Cincinnati, Ohio. With the exception of a few upper stories, where seismic demands were slightly higher than those from wind loads, the design was controlled by wind loads. Two half-scale and four three-quarter beam-wall subassemblies, each representing a steel coupling beam-wall connection, were fabricated and tested. The experimental test data were used to evaluate the current AISC 341 requirements and develop new design and detailing provisions for COSW.

4.2 Observations and conclusions

The following conclusions and observations are based on the information presented in this report.

1. The additional longitudinal reinforcement required by AISC 341-22 did not appreciably impact the connection performance in terms of the initial stiffness, stiffness degradation, dissipated energy, maximum load that could be resisted, and mode of failure.
2. Except for the specimens with embedment length/coupling beam depth ≤ 1 and the specimen with auxiliary transfer bars attached to the flanges, the other specimens did not fully develop their target shear of V_n. These specimens failed at $0.96V_n$ or $0.99V_n$, failed after the application of one cycle with the applied shear being equal to V_n, or failed prematurely at $0.79V_n$. The force resistance mechanism with short embedment lengths (i.e., when embedment length/coupling beam depth ≤ 1) is attributed to the formation of struts and ties instead of the formulation used in the development of the current ASIC 341-22 equation for determining the required embedment length. AISC 341-22 embedment length equation is based on assuming a linear strain distribution, which becomes questionable for cases with embedment length/coupling beam depth ≤ 1. Although AISC 341-22 equation underestimates the connection capacity and is conservative for cases with embedment length/coupling beam depth ≤ 1, the use of strut-and-tie models is more appropriate. The addition of auxiliary transfer bars provides additional resistance from the couple formed by the forces in the bars. Furthermore, the auxiliary transfer bars reduce the magnitude of the forces that need to be developed from the flange-concrete bearing stresses. Due to these benefits, the specimen with auxiliary transfer bars could successfully be subjected to the complete wind load and seismic displacement protocols.

3. The auxiliary transfer bars provide a direct load path for transferring the forces in the coupling beam to the surrounding concrete. This direct load path is not offered by longitudinal reinforcement along the embedment length. The lack of a direct load path is deemed to be the main reason for the similarities of the performance of the specimens with or without the higher longitudinal reinforcement required by AISC 341-22.
4. For the specimens without face bearing plates, which act as a bearing stiffener, the coupling beam's flange and web experienced local bending and buckling. In one specimen with face bearing plates, the flange experienced a small amount of bending within the connection region – the bending occurred at a location that was away from the face bearing plates. This specimen failed prematurely at $0.79V_n$, and its connection had experienced excessive damage.
5. Except for the specimens with embedment length/coupling beam depth ≤1, none of the specimens could develop the capacities calculated from the current equation (AISC Eq. H4-1) if the as-built dimensions and measured properties are used in the calculations. This trend is attributed to the fundamental assumptions in the derivation of the current equation, i.e., the depth of neutral axis/embedment length is taken as 0.66, concrete strain is 0.003 at the interface between the beam and wall pier, and the implicit hypothesis of "spreading" of bearing stresses beyond the flange width. It should be noted that loading for the specimen with auxiliary transfer was stopped prior to reaching the full capacity. For this reason, the measured maximum load for this specimen is less than its calculated capacity.
6. A new equation for calculating the required embedment length was developed based on analysis of the test results. In this equation, the strain at the coupling beam-wall interface

is taken as 0.0035 (instead of 0.003 in the current ASIC Eq. H4-1), and the depth of the neutral axis is set equal to 0.56 times the embedment length (compared to 0.66 in ASIC Eq. H4-1). The measured capacities were found to be within 3% of the capacities calculated by the new equation. Additional analytical studies of archetypes from a number of previous research indicate an excellent correlation between the capacities determined based on a detailed, mechanistic procedure and those from the new equation. Not only does the new equation closely capture the connection capacity but it is also simpler than the current equation (AISC Eq. H4-1).

7. The use of the new equation results in longer embedment lengths than the values computed from the current AISC Eq. H4-1. However, the embedment lengths are much shorter than those needed to develop the member capacity, which was required in the 2010 or earlier versions of AISC 341 *Seismic Provisions*.
8. With 95% confidence, the average value of the experimental stiffness is between 0.678 and 0.692 times the value obtained by using the effective moment of inertia calculated from AISC Eq. C-H4-1. Therefore, the coefficient of 0.6 in this equation needs to be changed to 0.4.
9. The archetype, which was used to select and detail the test specimens, had been designed by using the current AISC Eq. C-H4-1. By using the modified version of this equation (i.e., using 0.4 instead of 0.6), the first-floor wall piers of the archetype were found to be slightly inadequate (demand/capacity became 1.03 instead of 0.97 in the original design). Furthermore, the wind load inter-story drifts for several stories exceeded the limit of $h/450$, where h is the story height, but all the inter-story drifts remained below $h/400$.

4.3 Recommendations

Based on the results presented in this report, the following revisions to AISC 341 seismic provisions are recommended.

1. Replace the current AISC Eq. H4-1 by

$$V_n = \frac{0.19 f_c' b_f L_e}{0.56 + \frac{g}{2L_e}}$$

2. Replace the current AISC Eq. C-H4-1 by

$$I_{eff} = 0.40I\left(1 + \frac{12\lambda EI}{g^2 G A_w}\right)^{-1}$$

3. Require a bearing stiffener at the interface between steel coupling beams and reinforced concrete walls. This requirement may be waived if the adequacy of flanges and web against bending and buckling is ensured. It should be noted that face bearing plates could also simplify the formwork around the flanges and web.

Ballot items reflecting these proposed changes have been developed and are currently being reviewed by AISC Task Committee 5 (Composite Design).

References

AISC 341 (2010) *Seismic Provisions for Structural Steel Buildings-ANSI/AISC 341-10*, American Institute of Steel Construction, Chicago, IL.

AISC 341 (2016) *Seismic Provisions for Structural Steel Buildings-ANSI/AISC 341-16*, American Institute of Steel Construction Chicago, IL.

AISC 341 (2022) *Seismic Provisions for Structural Steel Buildings-ANSI/AISC 341-22*, American Institute of Steel Construction Chicago, IL.

American Concrete Institute (ACI) Committee 318, (2019) *Building Code Requirements for Structural Concrete (ACI 318-19) and Commentary (ACI 318R-19)*, American Concrete Institute, Farmington Hills, MI, 623 pp.

ASTM (2017) ASTM C496/C496M *Standard Test Method for Splitting Tensile Strength of Cylindrical Concrete Specimens*, ASTM International, West Conshohocken, PA, 5 pp.

ASTM (2020) ASTM C42/C42M *Standard Test Method for Obtaining and Testing Drilled Cores and Sawed Beams of Concretes*, ASTM International, West Conshohocken, PA, 7 pp.

ASTM (2021) ASTM C39/C39M *Standard Test Method for Compressive Strength of Cylindrical Concrete Specimens*, ASTM International, West Conshohocken, PA, 8 pp.

ASTM (2022) ASTM C39/C39M *Standard Test Methods and Definitions for Mechanical Testing of Steel Products*, ASTM International, West Conshohocken, PA, 51 pp.

ASTM (2022) ASTM E8/E8M *Standard Test Methods for Tension Testing of Metallic Materials, ASTM International*, West Conshohocken, PA, 31 pp.

Computers and Structures Inc. (2016), *ETABS version 16.2*, Berkeley, CA.

Fortney, J.P. (2005) *The Next Generation of Coupling Beams*, PhD Dissertation, University of Cincinnati, Cincinnati, OH, 370 pp. (http://rave.ohiolink.edu/etdc/view?acc_num=ucin1115837131)

Gong, B. (1998) Seismic Behavior of Composite Coupled Wall Systems, PhD Dissertation, University of Cincinnati, Cincinnati, OH, 293 pp.

Harries, K.A., Fortney, P.J., Shahrooz, B.M. Brienen, P.J. (2005) *Design of Practical Diagonally Reinforced Concrete Coupling Beams – A Critical Review of ACI 318 Requirements*, ACI Structural Journal, Vol. 102, No. 6, 876-882.

Harries, K.A., Mitchell, D., Redwood, R.G. and Cook, W.D. (1997). *Seismic Design of Coupling Beams—A Case for Mixed Construction*, Canadian Journal of Civil Engineering, Vol. 24, No. 3, pp. 448–459.

Hill, J., Forbes, J., Motter, C.J. (2023) *Nonlinear Wind Design of Steel Reinforced Concrete (SRC) Coupling Beams: Final Report and Design Recommendations*, Washington State University, Pullman, WA, 155 pp.

Kunwar, S. (2020) *Comprehensive Evaluation of Composite Core Walls for Low-Seismic Force and Wind Load Applications*, MS Thesis, University of Cincinnati, Cincinnati, OH, 72 pp. (http://rave.ohiolink.edu/etdc/view?acc_num=ucin1613750905724949)

Mattock, A. H., Gaafar, G. H. (1982) *Strength of Embedded Steel Sections as Brackets*, ACI Structural Journal, Vol. 79, No. 2, 83-93.

Mirza, A.R. (2018) *Evaluation of AISC Coupling Beam Embedment Length in Composite Ordinary Shear Walls*, MS Thesis, University of Cincinnati, Cincinnati, OH, 105 pp. (http://rave.ohiolink.edu/etdc/view?acc_num=ucin1543577095290297)

Motter, C.J. (2013), *Large-Scale Testing of Steel Reinforced Concrete (SRC) Coupling Beams Embedded into RC Shear Walls*, PhD Dissertation, University of California – Los Angeles, 199 pp.

Remmetter, M.E. (1992) *Investigation of Composite Connections for Coupled Shear Walls Utilizing Steel Coupling Beams*, MS Thesis, University of Cincinnati, Cincinnati, OH, 185 pp.

Shahrooz, B.M., Fortney, P.J., Harries K.A. (2018) *Steel Coupling Beams with a Replaceable Fuse*, Journal of Structural Engineering, ASCE, (144)(2)(2018): 04017210_1:11.

This page left blank intentionally.

Appendix A
Derivation of development length equation for specimen 4 (test 6)

A.1 Introduction

Figure A.1 shows the compressive stresses developed above and below the embedded steel section due to the applied load V_n acting at a distance a from the face of the wall. A linear strain distribution with a strain of 0.003 at the outer face of the wall is assumed. Hognestad concrete model (see Figure A.2) gives the parabolic stress-strain relationship for the concrete stresses and is mathematically represented by Eq. A.1. A strain of 0.002 is assumed for the maximum stress of f_c.

$$f_c = 1000 f_{max}[\varepsilon - 250\varepsilon^2] \qquad \textbf{Eq. A.1}$$

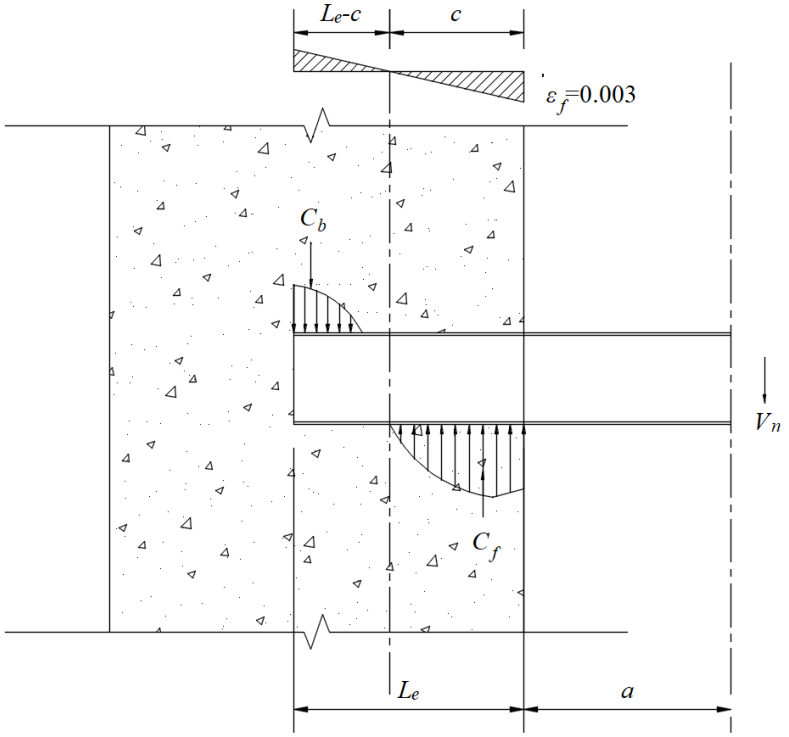

Figure A.1 Stresses in the embedment region.

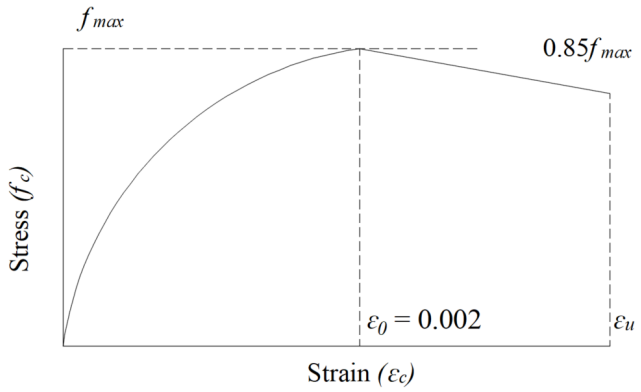

Figure A.2 Hognestad concrete model.

A.2 Calculation of front bearing force (C_f)

The front bearing force (C_f) is determined by recognizing that the stress-strain distribution consists of a parabolic section and a trapezoidal section, as shown in Figure A.3. For each section, the magnitude of forward bearing force and its location is calculated separately.

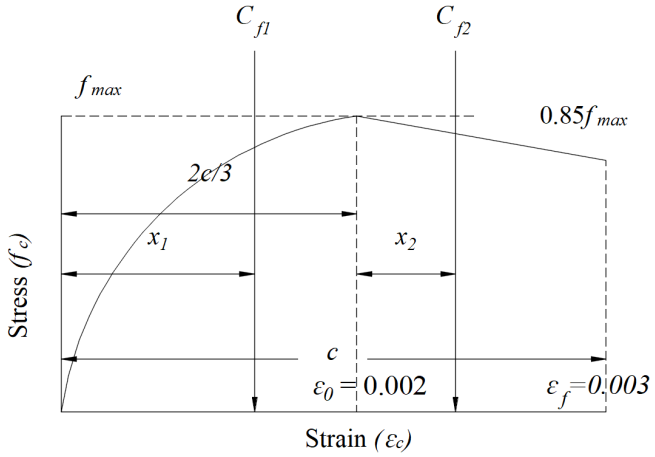

Figure A.3 Front bearing forces and their locations.

A.2.1 Parabolic segment

Force

$$C_{f_1} = \int_0^{\frac{2c}{3}} 1000 f_{max} (\varepsilon - 250\varepsilon^2) b_f dx \; where, b_f \; is \; flange \; width \; and \; \varepsilon = \frac{x\varepsilon_f}{c}$$

$$C_{f_1} = 1000 f_{max} b_f \frac{4\varepsilon_f c}{9}\left[\frac{1}{2} - \frac{500}{9}\varepsilon_f\right]$$

$$Substituting \; \varepsilon_f = 0.003$$

$$C_{f_1} = \frac{4}{9} f_{max} b_f c$$

Location

$$\bar{x} = \frac{\int_0^{\frac{2c}{3}} x 1000 f_{max}(\varepsilon - 250\varepsilon^2) dx}{\int_0^{\frac{2c}{3}} 1000 f_{max}(\varepsilon - 250\varepsilon^2) dx}$$

$$\bar{x} = \frac{\frac{2c}{3}\left(\frac{1}{3} - \frac{125}{3}\varepsilon_f\right)}{\left(\frac{1}{2} - \frac{500}{9}\varepsilon_f\right)}$$

$$Substituting \; \varepsilon_f = 0.003$$

$$\bar{x} = x_1 = \frac{5c}{12}$$

A.2.2 Trapezoidal segment

Force

$$C_{f_2} = \left(\frac{f_{max} + 0.85f_{max}}{2}\right)\frac{c}{3}b_f$$

$$C_{f_2} = 0.308 f_{max} c b_f$$

Location

$$\bar{x} = \frac{\frac{c}{3}(1.7f_{max} + f_{max})}{3(f_{max} + 0.85f_{max})}$$

$$\bar{x} = x_2 = \frac{6c}{37}$$

A.3 Back bearing force (C_b)

A parabolic stress distribution is assumed for the back portion of the connection, see Figure A.4.

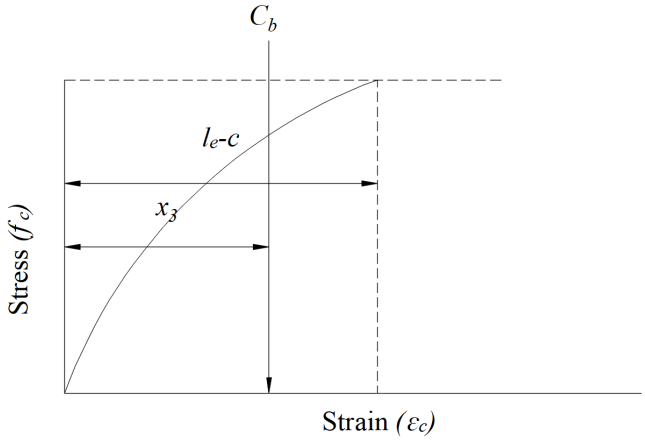

Figure A.4 Back bearing force.

Force

$$C_b = \int_0^{L_e - c} 1000 f_{max}(\varepsilon - 250\varepsilon^2)\, b_f dx \; where \; \varepsilon = \frac{\varepsilon_f x}{c}$$

$$C_b = 1000 f_{max} b_f \frac{\varepsilon_f}{c}(L_e - c)^2 \left[\frac{1}{2} - \frac{250}{3}\varepsilon_f\left(\frac{L_e}{c} - 1\right)\right]$$

$$Substituting \; \varepsilon_f = 0.003$$

$$C_b = 3 f_{max} \frac{b_f}{c}(L_e - c)^2 \left[\frac{1}{2} - \frac{1}{4}\left(\frac{L_e}{c} - 1\right)\right]$$

Location

$$\bar{x} = \frac{\int_0^{L_e-c} x1000f_{max}(\varepsilon - 250\varepsilon^2)dx}{\int_0^{L_e-c} 1000f_{max}(\varepsilon - 250\varepsilon^2)dx}$$

$$\bar{x} = \frac{(L_e - c)\left[\frac{1}{3} - \frac{250}{4}\varepsilon_f\left(\frac{L_e - c}{c}\right)\right]}{\left[\frac{1}{2} - \frac{250}{3}\varepsilon_f\left(\frac{L_e - c}{c}\right)\right]}$$

$Substituting\ \varepsilon_f = 0.003$

$$\bar{x} = x_3 = \frac{(L_e - c)\left[\frac{1}{3} - \frac{3}{16}\left(\frac{L_e - c}{c}\right)\right]}{\left[\frac{1}{2} - \frac{1}{4}\left(\frac{L_e - c}{c}\right)\right]}$$

The summary of forces and their locations are shown in Figure A.5.

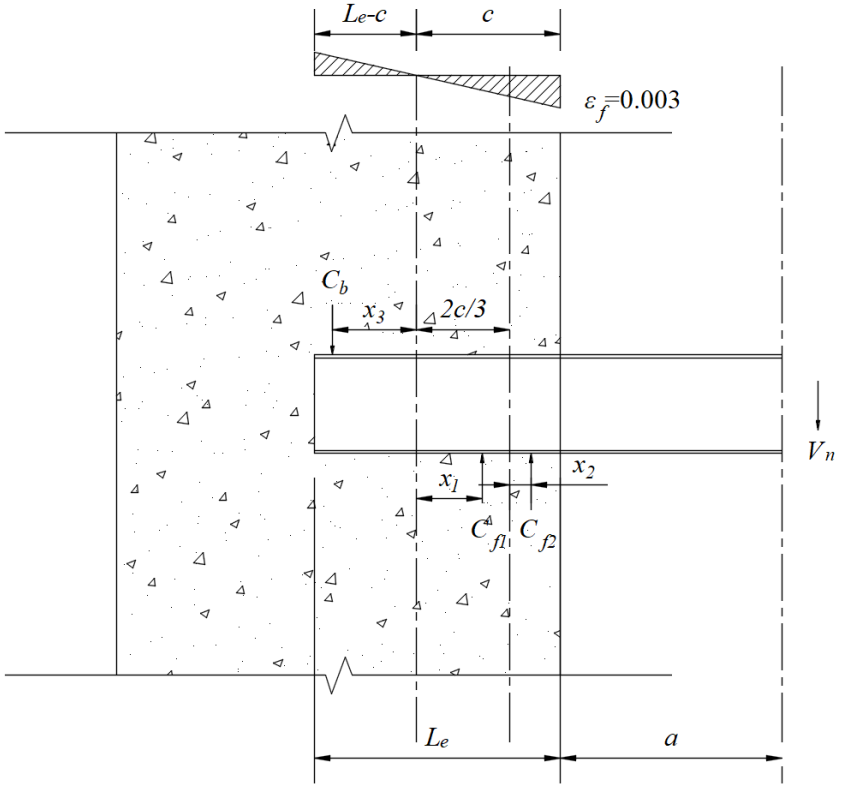

Figure A.5 Forces and their locations.

A.4 Relationship between depth of compressive zone (c) and embedment length (L_e)

In Figure A.5, sum the moments about V_n

$$C_b \times (x_3 + c + a) = C_{f_1} \times (a + c - x_1) + C_{f_2} \times \left(a + c - \frac{2c}{3} - x_2\right)$$

$$3f_{max}\frac{b_f}{c}(L_e-c)^2\left[\frac{(L_e-c)\left(\frac{1}{3}-\frac{3}{16}\left(\frac{L_e-c}{c}\right)\right)}{\frac{1}{2}-\frac{1}{4}\left(\frac{L_e-c}{c}\right)}+c+a\right]$$
$$=\frac{4}{9}f_{max}b_f c\left(a+c-\frac{5c}{12}\right)+\frac{37}{120}f_{max}cb_f\left(a+\frac{c}{3}-\frac{6c}{37}\right)$$

$$3\frac{c}{L_e}\left(\frac{L_e}{c}-1\right)^2\left(\frac{3}{4}-\frac{1}{4}\frac{L_e}{c}\right)\left[\frac{\left(1-\frac{c}{L_e}\right)\left(\frac{25}{58}-\frac{3}{16}\frac{L_e}{c}\right)}{\frac{3}{4}-\frac{1}{4}\frac{L_e}{c}}+\frac{c}{L_e}+\frac{a}{L_e}\right]$$
$$=\frac{4}{9}\frac{c}{L_e}\left(\frac{a}{L_e}+\frac{7}{12}\frac{c}{L_e}\right)+\frac{37}{120}\frac{c}{L_e}\left(\frac{a}{L_e}+\frac{19}{111}\frac{c}{L_e}\right)$$

Figure A.6 shows the variation of c/L_e for different values of a/L_e. The average value of c/L_e is found to be 0.59 with the coefficient of variation of 5.6%.

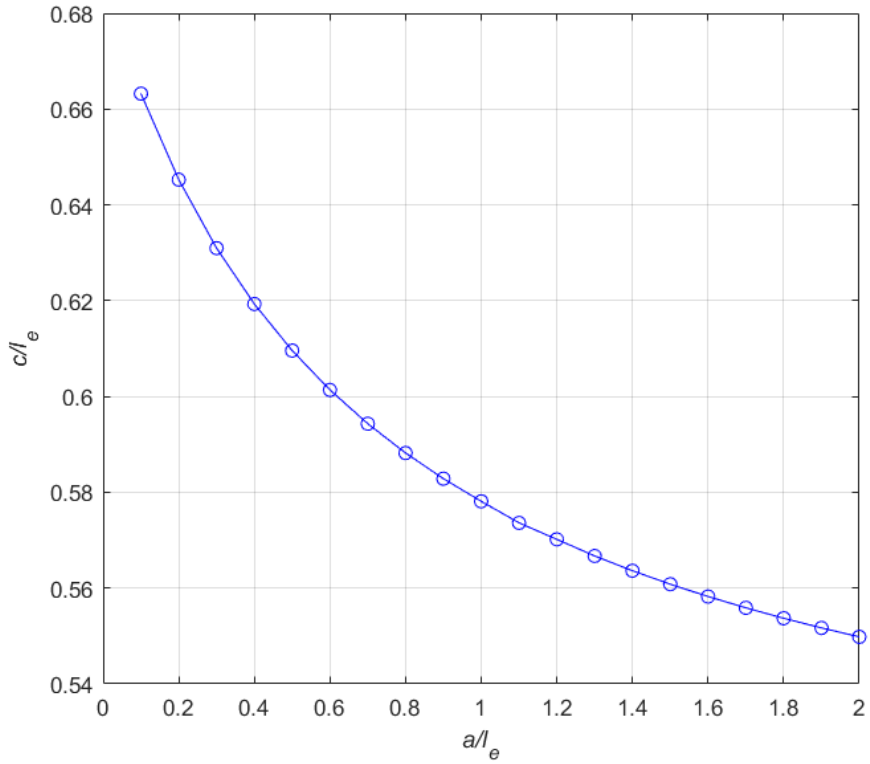

Figure A.6 Variation of c/L_e with respect to a/L_e.

A.5 Embedment length equation

In Figure A.5, sum the moments about the back bearing force

$$V_n\times(a+c+x_3)-C_{f_1}\times(x_1+x_3)-C_{f_2}\times\left(x_2+\frac{2c}{3}+x_3\right)=0$$

Simplify equations for $C_{f_1}, C_{f_2}, x_1, x_2$ and $x_3$by susbtituting ${}^{C}/_{L_e} = 0.59$.

$$V_n \times \left(\frac{a}{L_e} + \frac{c}{L_e} + \frac{0.255L_e}{L_e}\right) = \frac{4}{9} f_{max} b_f c \times 0.501L_e + \frac{37}{120} f_{max} b_f c \times 0.744L_e$$

$$V_n = \frac{0.267 f_{max} b_f L_e}{0.845 + \frac{a}{L_e}}$$

$Assume\ f_{max} = 0.85 f_c'$

$$V_n = \frac{0.227 f_c' b_f L_e}{0.845 + \frac{a}{L_e}}$$

This page left blank intentionally.

Appendix B
Measured stress-strain diagrams of reinforcement and steel coupling beams

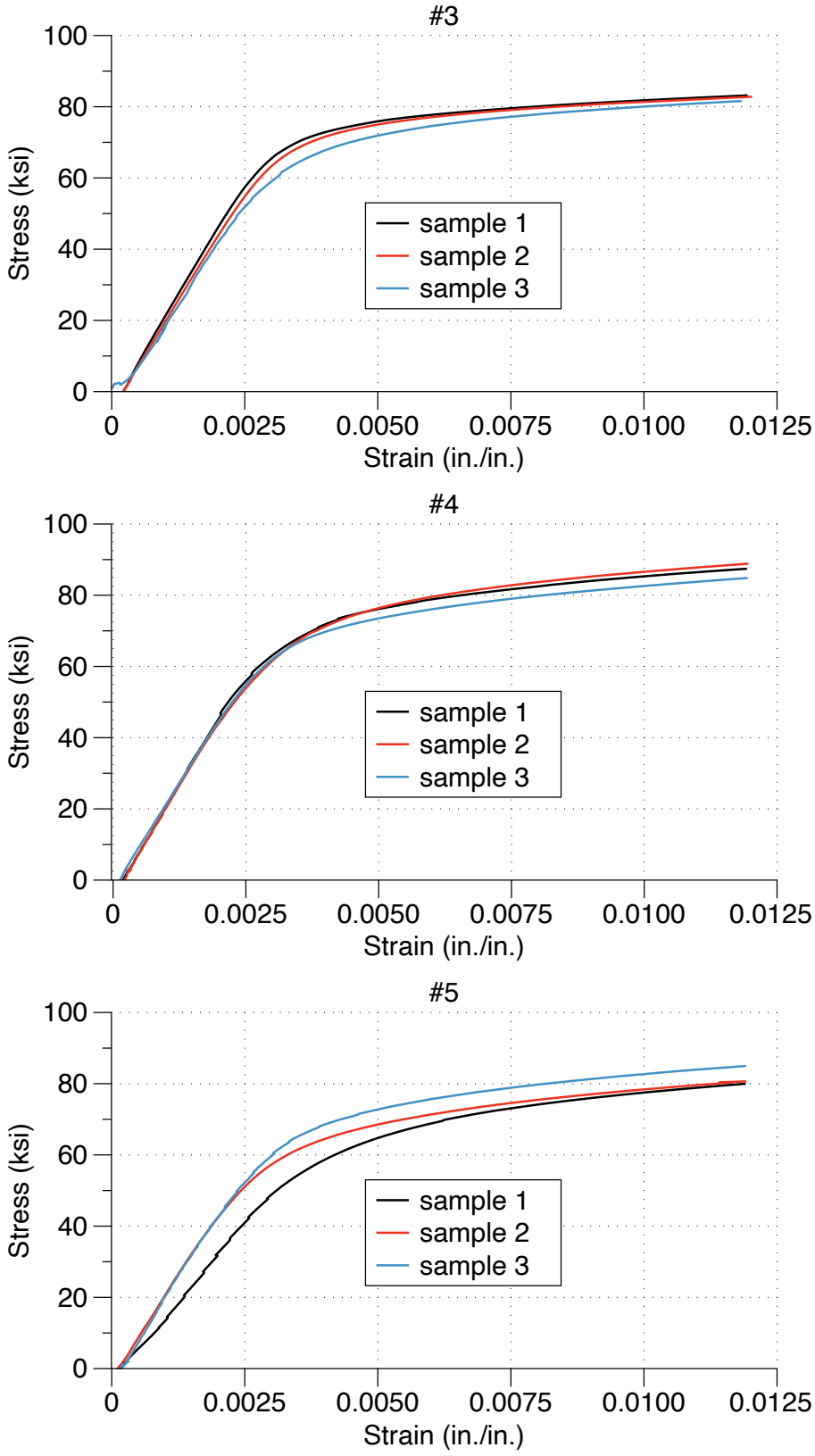

Figure B.1 Stress-strain diagrams – reinforcing bars in phase 1 specimens.

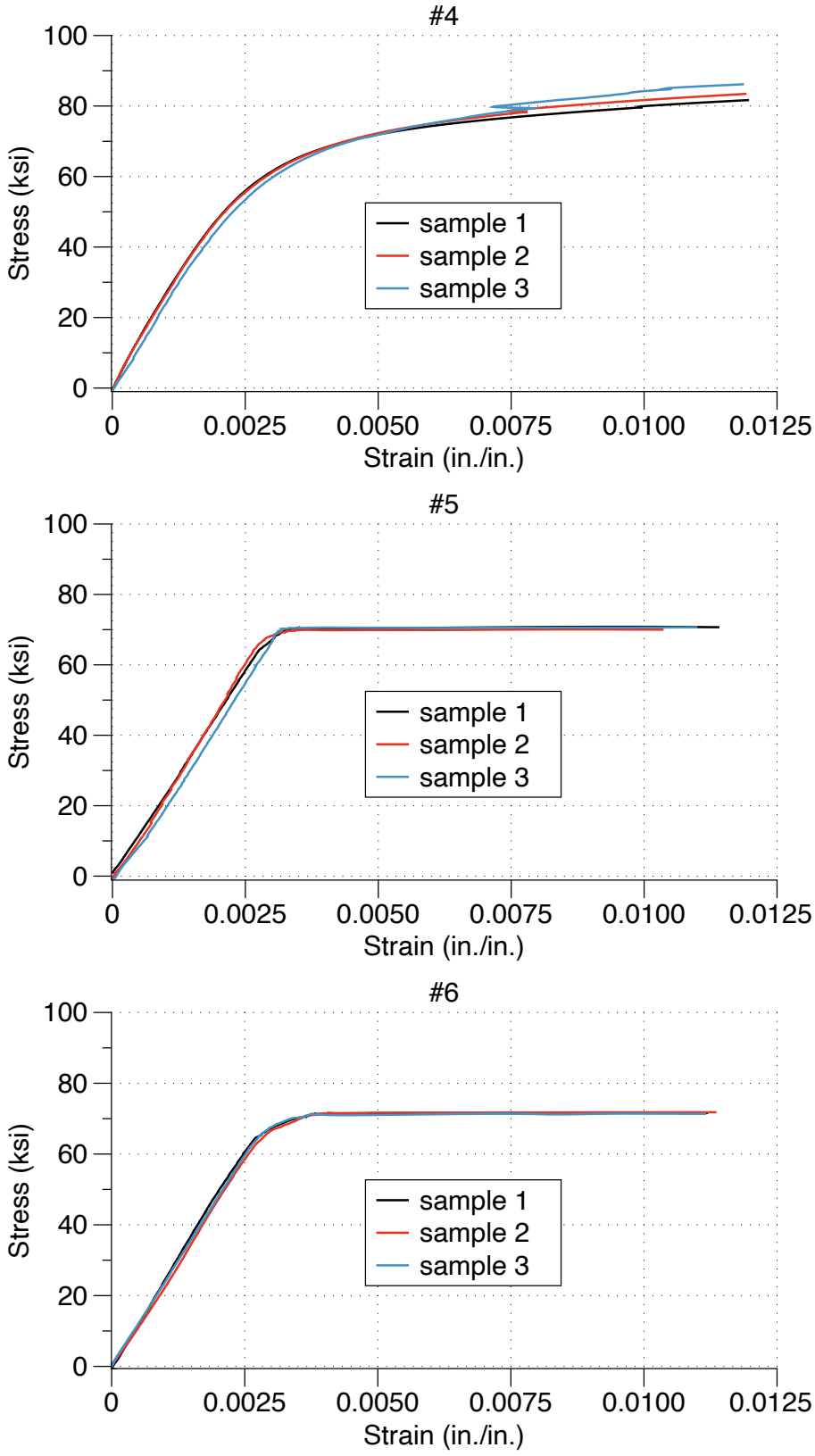

Figure B.2 Stress-strain diagrams – reinforcing bars in phase 2 specimens.

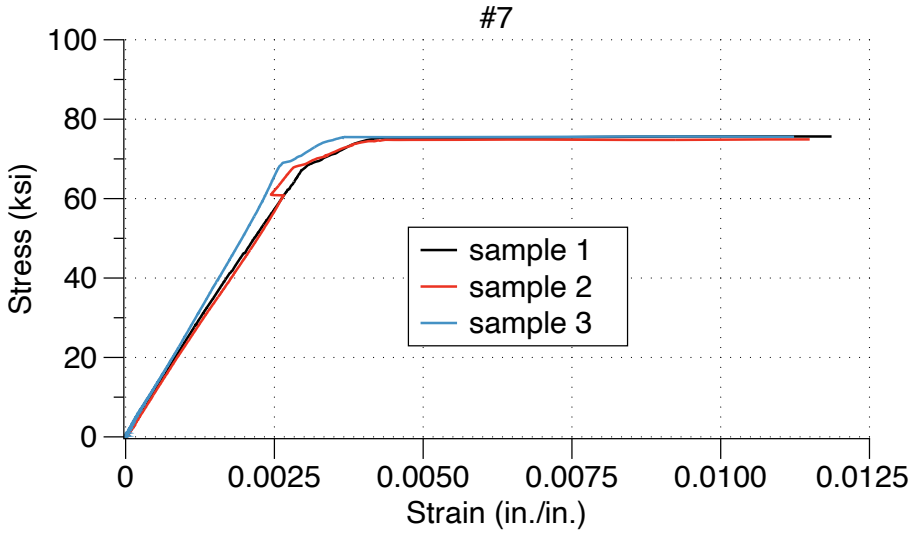

Figure B.2 Stress-strain diagrams – reinforcing bars in phase 2 specimens (cont.).

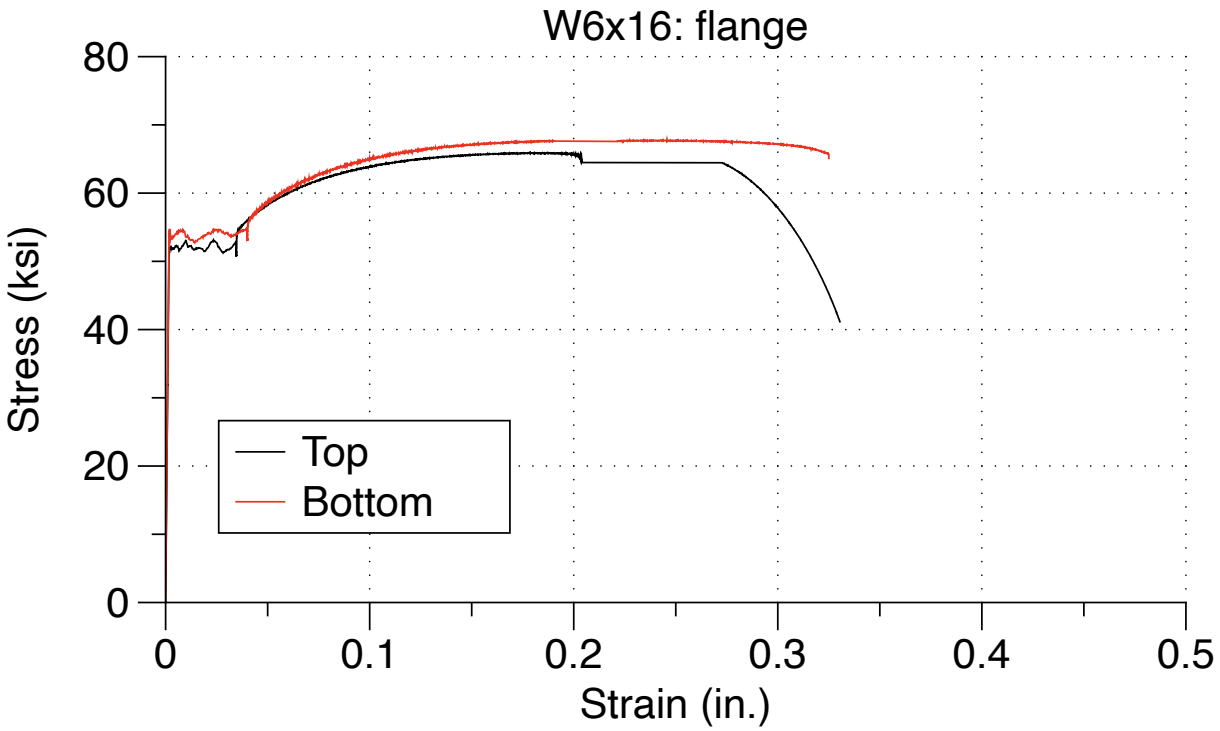

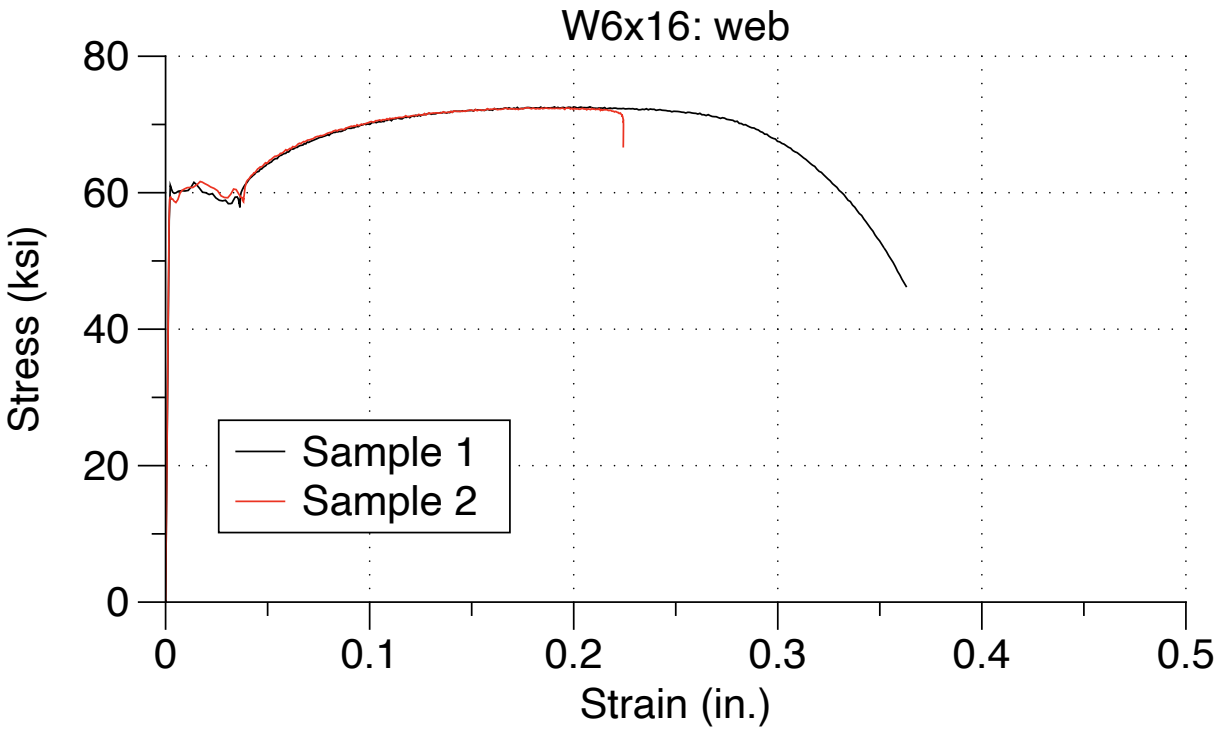

Figure B.3 Stress-strain diagram - steel coupling beam W6x16 (specimens 1a and 1b).

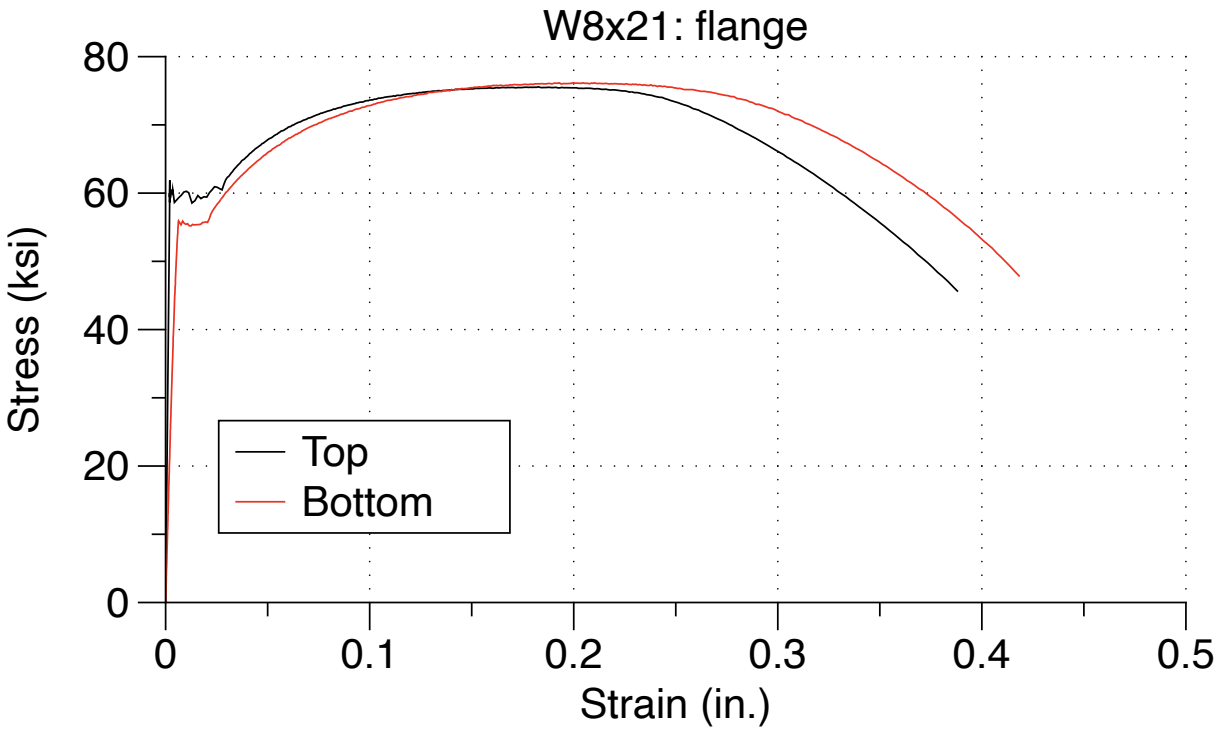

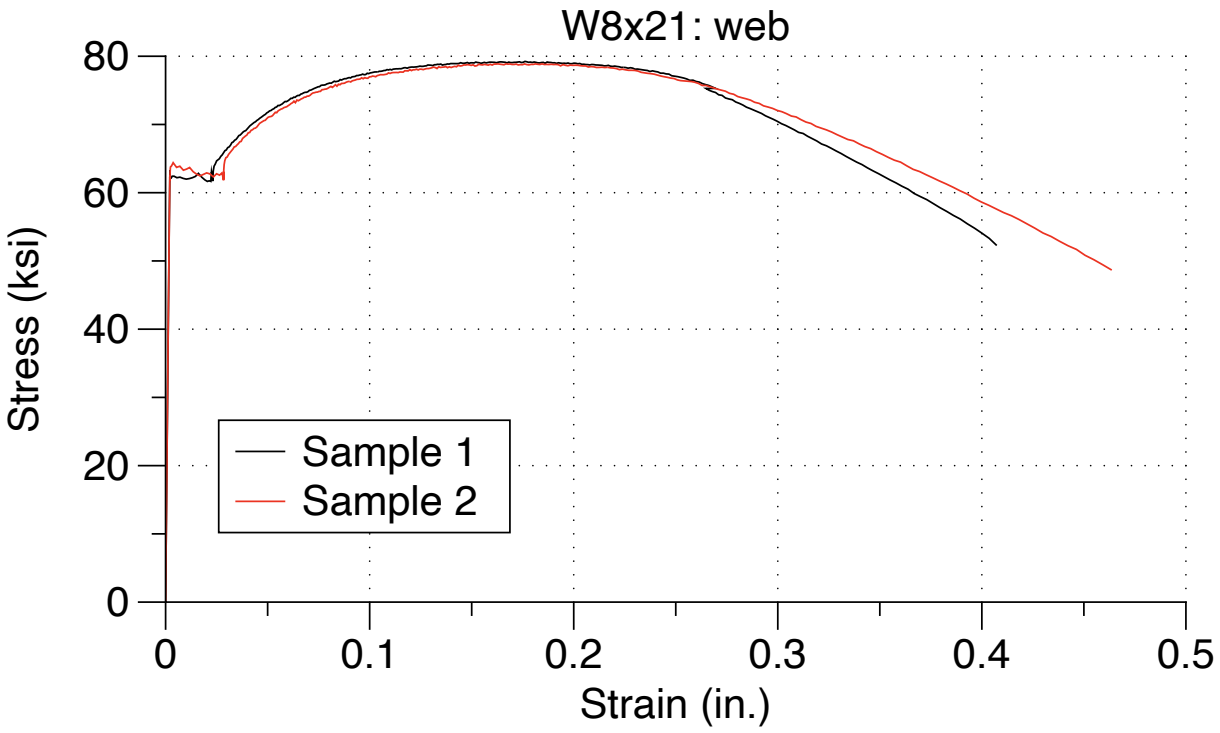

Figure B.4 Stress-strain diagram - steel coupling beam W8x21 (specimens 2a and 2b)

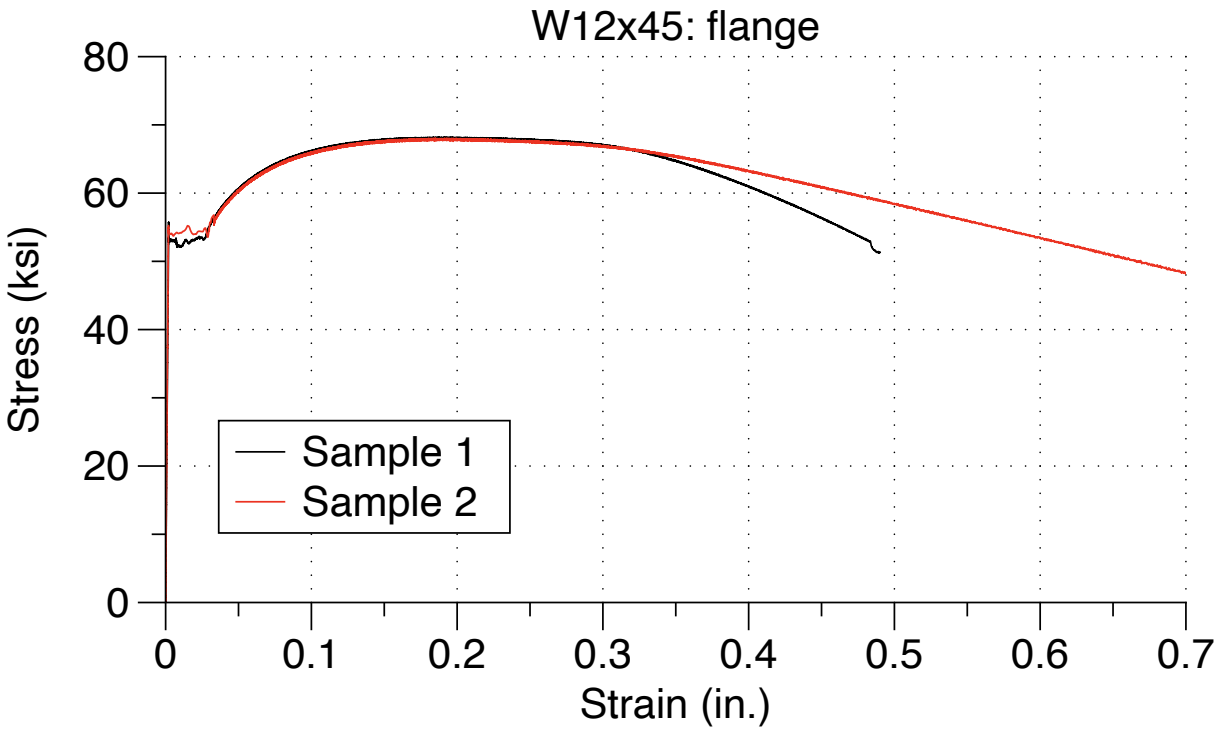

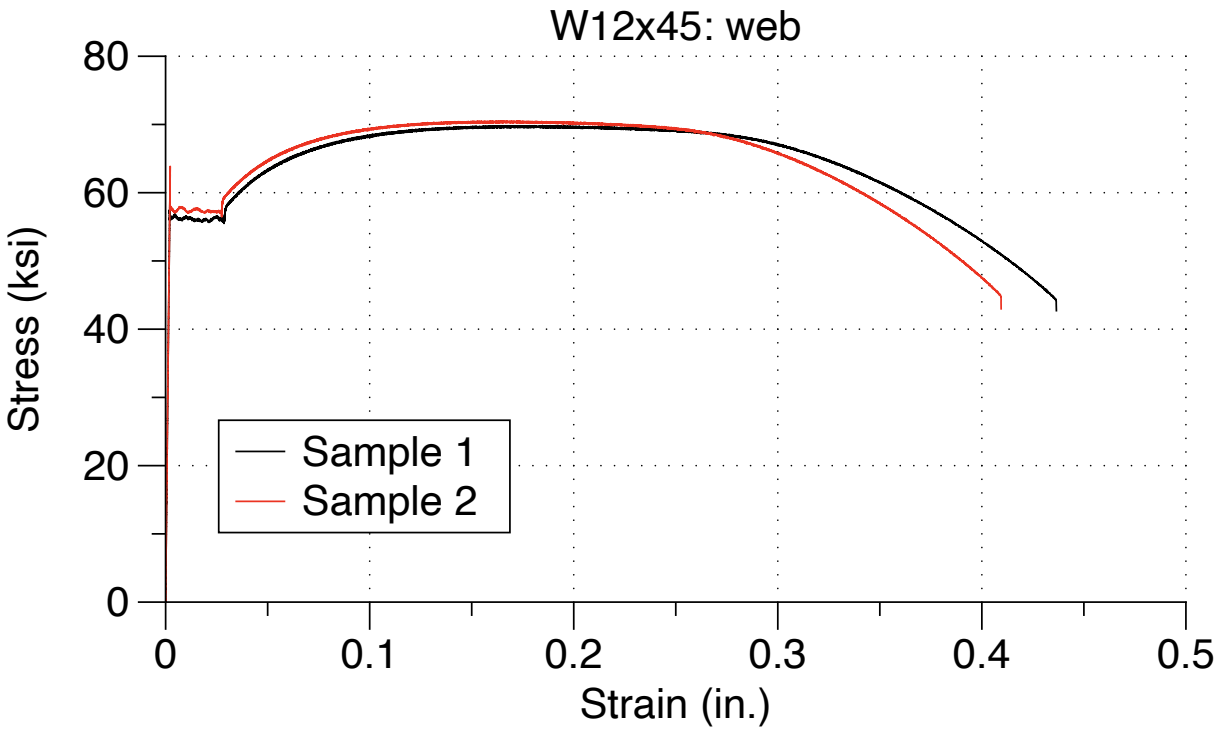

Figure B.5 Stress-strain diagram - steel coupling beam W12x45 (specimens 3-6).

This page left blank intentionally.

Appendix C
Force relationships between secondary and primary actuators

The forces in the secondary actuators need to be related to the coupling beam shear force. These relationships were determined to maintain equal stresses in the prototype C-shaped wall pier and test specimen rectangular wall. The procedure is explained in the following with reference to Figure C.1.

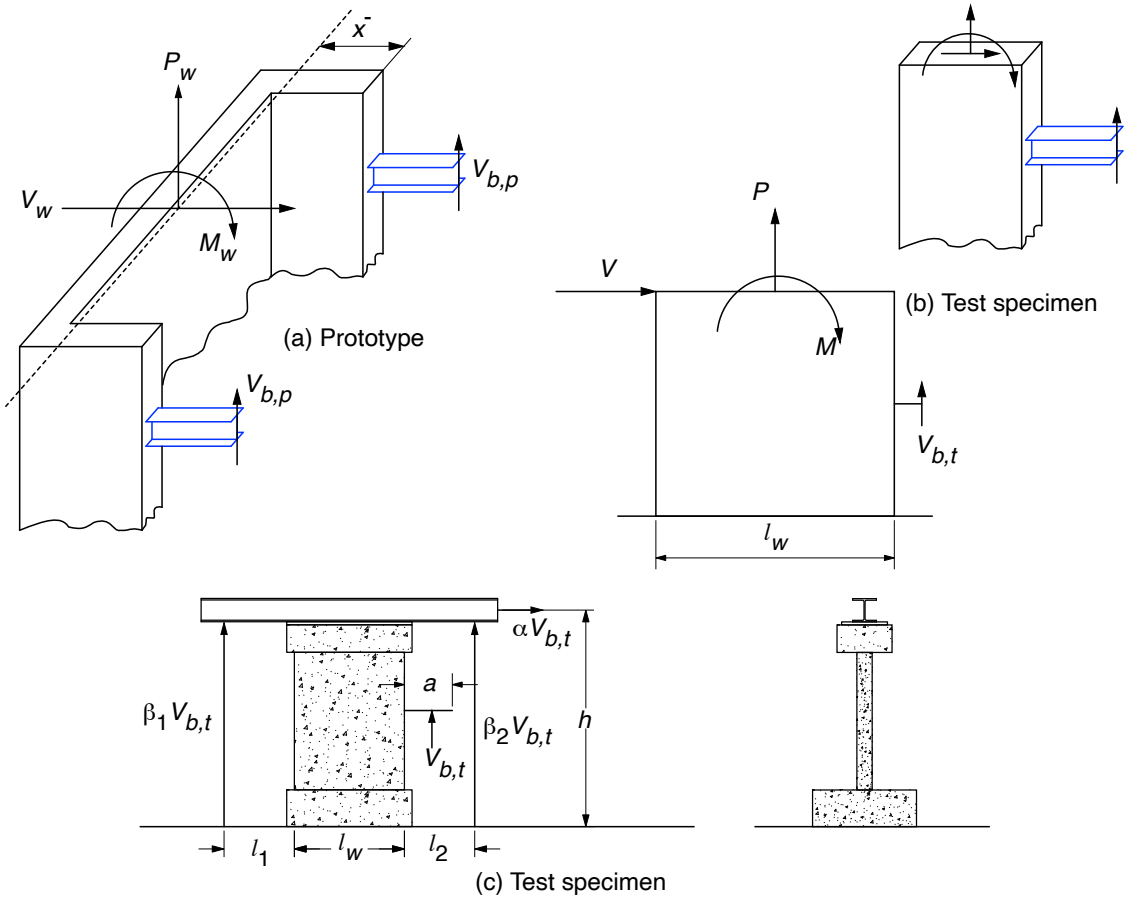

Figure C.1 Illustration of procedure for establishing relationships between actuators.

1. For the prototype structure, the relationships between coupling beam shear ($V_{b,p}$) and wall shear (V_w), wall axial force (P_w), and wall overturning moment (M_w) are established based on the calculated design forces obtained from analysis, i.e., factors R_1, R_2, and R_3 shown in Eq. C.1. These relationships are then used to express the axial stresses (σ) and shear stress (τ) in the prototype C-shaped wall pier in terms of coupling beam shear (Eq. C.1).

$$\frac{V_w}{2V_{b,p}} = R_1 \qquad \frac{P_w}{2V_{b,p}} = R_2 \qquad \frac{M_w}{2V_{b,p}} = R_3$$

$$\tau_{due\ to\ V_w} \approx \frac{V_w}{A_{c\ shaped\ wall}} \qquad \sigma_{due\ to\ P_w} = \frac{P_w}{A_{c\ shaped\ wall}} \qquad \sigma_{due\ to\ M_w} = \frac{M_w x^-}{I_{c\ shaped\ wall}} \qquad \textbf{Eq. C.1}$$

$$\tau_{due\ to\ V_w} \approx \frac{2V_{b,p}R_1}{A_{c\ shaped\ wall}} \qquad \sigma_{due\ to\ P_w} = \frac{2V_{b,p}R_2}{A_{c\ shaped\ wall}} \qquad \sigma_{due\ to\ M_w} = \frac{2V_{b,p}R_3 x^-}{I_{c\ shaped\ wall}}$$

2. The level of stress in wall piers is a key factor influencing the performance of coupling beam. Therefore, the axial stresses due to axial force and overturning moment as well as the shear

stress in the prototype C-shaped wall pier and rectangular are set equal. These stresses (Eq. C.2) can be simplified to find the relationships between the wall shear force (V), axial force (P), and overturning moment (M) and the coupling beam shear ($V_{b,t}$) in the test specimen as shown in Eq. C.3.

$$\sigma_{due\ to\ P} = \frac{P}{A_{rectangular\ wall}} = \sigma_{due\ to\ P_w} = \frac{2V_{b,p}R_2}{A_{c\ shaped\ wall}}$$

$$\sigma_{due\ to\ M} = \frac{M(0.5l_w)}{I_{rectangular\ wall}} = \sigma_{due\ to\ M_w} = \frac{2V_{b,p}R_3x^-}{I_{c\ shaped\ wall}} \qquad \textbf{Eq. C.2}$$

$$\tau_{due\ to\ V} \approx \frac{V}{A_{rectangular\ wall}} = \tau_{due\ to\ V_w} \approx \frac{2V_{b,p}R_1}{A_{c\ shaped\ wall}}$$

$$\frac{P}{V_{b,t}} = \frac{2\left(A_{rectangular\ wall}\right)R_2}{A_{c\ shaped\ wall}} \rightarrow P = V_{b,t}\frac{2\left(A_{rectangular\ wall}\right)R_2}{A_{c\ shaped\ wall}}$$

$$\frac{M}{V_{b,t}} = \frac{2\left(I_{rectangular\ wall}\right)R_3x^-}{0.5l_w\left(I_{c\ shaped\ wall}\right)} \rightarrow M = V_{b,t}\frac{2\left(I_{rectangular\ wall}\right)R_3x^-}{0.5l_w\left(I_{c\ shaped\ wall}\right)} \qquad \textbf{Eq. C.3}$$

$$\frac{V}{V_{b,t}} = \frac{2\left(A_{rectangular\ wall}\right)R_1}{A_{c\ shaped\ wall}}$$

3. The value of α (see Figure C.1) is $V/V_{b,t}$ calculated from Eq. C.3. The value of R_1 is obtained from Eq. C.1. Equilibrium of forces shown in Figure C.1c is used to obtain the values of β_1 and β_2; the equilibrium equations are $P = \beta_1 V_{b,t} + \beta_2 V_{b,t}$ and $M = \beta_1 V_{b,t}(l_1 + 0.5l_w) - \beta_2 V_{b,t}(l_2 + 0.5l_w)$. From these two equations, the expressions for β_1 and β_2 become

$$\beta_1 V_{b,t} = \frac{M + P(l_2 + 0.5l_w)}{l_1 + l_2 + l_w} \qquad \beta_2 V_{b,t} = \frac{P(l_1 + 0.5l_w) - M}{l_1 + l_2 + l_w}$$

Substituting P and M by the expressions obtained in Eq. C.3, the values of β_1 and β_2 can be determined from Eq. C.4 in which R_2 and R_3 are from Eq. C.1.

$$\beta_1 = \frac{\frac{2\left(I_{rectangular\ wall}\right)R_3x^-}{0.5l_w\left(I_{c\ shaped\ wall}\right)} + \frac{2\left(A_{rectangular\ wall}\right)R_2}{A_{c\ shaped\ wall}}(l_2 + 0.5l_w)}{l_1 + l_2 + l_w}$$

$$\beta_2 = \frac{\frac{2\left(A_{rectangular\ wall}\right)R_2}{A_{c\ shaped\ wall}}(l_1 + 0.5l_w) - \frac{2\left(I_{rectangular\ wall}\right)R_3x^-}{0.5l_w\left(I_{c\ shaped\ wall}\right)}}{l_1 + l_2 + l_w} \qquad \textbf{Eq. C.4}$$

This page left blank intentionally.